NASA CONTRACTOR REPORT

ANALYSIS OF HYPERSONIC PRESSURE AND HEAT TRANSFER TESTS ON A FLAT PLATE WITH A FLAP AND A DELTA WING WITH BODY, ELEVONS, FINS, AND RUDDERS

by H. L. Giles and J. W. Thomas

Prepared by
THE BOEING COMPANY
Seattle, Wash.
for Langley Research Center

NATIONAL AERONAUTICS AND SPACE ADMINISTRATION • WASHINGTON, D. C. • AUGUST 1966

NASA CR-536

ANALYSIS OF HYPERSONIC PRESSURE AND HEAT TRANSFER TESTS ON A FLAT PLATE WITH A FLAP AND A DELTA WING WITH BODY, ELEVONS, FINS, AND RUDDERS

By H. L. Giles and J. W. Thomas

Prepared under Contract No. NAS 1-4301 by
THE BOEING COMPANY
Seattle, Wash.

for Langley Research Center

NATIONAL AERONAUTICS AND SPACE ADMINISTRATION

For sale by the Clearinghouse for Federal Scientific and Technical Information
Springfield, Virginia 22151 – Price $4.00

PREFACE

This is one of three final reports on a program to complete the analysis of existing aerothermodynamic test data obtained during the X-20 program. The work has been accomplished by The Boeing Company under Contract NAS 1-4301 with NASA, Langley Research Center, Hampton, Virginia. A. L. Nagel was the program manager, H. L. Giles was the principal investigator, and M. H. Bertram was the NASA contract monitor. Final reports have been prepared for each of three tasks:

Task I - Analysis of Hypersonic Pressure and Heat Transfer Tests on Delta Wings with Laminar and Turbulent Boundary Layers.

Task II - Analysis of Hypersonic Pressure and Heat Transfer Tests on a Flat Plate with a Flap and a Delta Wing with a Body, Elevons, Fins, and Rudders.

Task III - Analysis of Pressure and Heat Transfer Tests on Surface Roughness Elements with Laminar and Turbulent Boundary Layers.

Results of Task II are presented in this report.

CONTENTS

ANALYSIS OF HYPERSONIC PRESSURE AND HEAT TRANSFER TESTS ON A FLAT PLATE WITH A FLAP AND A DELTA WING WITH BODY, ELEVONS, FINS, AND RUDDERS

By H. L. Giles and J. W. Thomas

SUMMARY

Results are presented of an analysis of hypersonic boundary layer separation and flow field interference data taken during the X-20 (Dyna-Soar) program. Pressure and heat transfer data were taken on a sharp flat plate at Mach numbers of 6.38 and 15.15 and Reynolds numbers per foot, based on model length, of 1.404×10^7 and 1.12×10^5, respectively, in the Cornell shock tunnel. Tests on the flat plate model included angles of attack from -15° to +15° and flap deflections from -45° to +45°. Also included were tests of the flat plate model with span extensions to evaluate the three-dimensional effects on separation. Tests of a blunt delta wing were made at Mach number 8.08 at a Reynolds number per foot, based on a model length, of 1.202×10^6 in the AEDC tunnel B. Separation tests were made at angles of attack from 0° to 30° with elevons deflected 0°, 20°, and 45°. A body with a canopy windshield and swept vertical fins was tested on the blunt delta wing model to evaluate interference. The interference tests were made at angles of attack from -10° to +20° and at yaw angles of 0°, +5°, and -5°.

Laminar and transitional separation plateau pressure data are compared with results obtained using existing two-dimensional theoretical and empirical methods. The areas of separation on the blunt delta wing are defined. Boundary layer separation lengths are compared with two-dimensional analytical results and are empirically correlated with a modified theoretical relation. Peak pressures on the elevon are compared with an attached-flow theory. Theoretical heating rate predictions are compared with test data. Pressure and heating on the expansion side of a sharp flat plate are compared with a viscous theory. Interfering flow effects are found to be extremely complex and cannot be predicted by existing techniques.

INTRODUCTION

At the beginning of the X-20 program in November 1959 there was an urgent need for aerothermodynamic information on complex configurations, particularly on flow separation and interference. Although much work had been done for flat plates and simple shapes under ideal conditions, there were few data or techniques available for application to the design and analysis of actual vehicle configurations.

In order to provide an experimental basis for configuration development and aid in development of theoretical methods, an extensive parameteric series of delta wing tests was conducted early in the X-20 program. In conjunction with the delta wing program, tests were performed on configuration build-ups, including blunt delta wings with tip fins and deflected rudders, bodies tailored for housing necessary equipment for flight and crew compartments, and deflected elevons. Additional tests of basic flat plates were performed with deflected flaps and also with span extensions. One purpose of the tests was to extend the Mach number range of the current data.

Although some of these data have been reported in X-20 program documentation, no complete analysis of the data had been made, nor any analysis reports written. This report presents the separation and interference data, an appraisal of the data, and comparisons of the data with existing theories. Included are the pressure and heating on a sharp flat plate with deflected flaps at Mach 6.38 and 15.15 and on a blunt delta wing with deflected elevons at Mach 8.08. Interference pressure and heating data are presented for combinations of tip fins and bodies with the blunt delta wing. The majority of the data are for laminar flow; however, some turbulent flow data are presented.

Although considerable time has elapsed since these tests were made, there still remains a need for hypersonic separation and interference data, particularly on composite configurations. Accordingly, the NASA has financed the continued analysis and publication of the data. Two other reports in this series, references 1 and 2, present the results of delta wing heating tests and surface roughness tests conducted during the X-20 program.

SYMBOLS

b_F	span of flap
c	specific heat of model skin
c_F	chord of flap
c_p	specific heat at constant pressure
C_f	skin friction coefficient, $\tau / \left[1/2 \ (\rho u^2) \right]$
C_P	pressure coefficient
$C'_{P_{PL}}$	plateau pressure coefficient referenced to inviscid pressure rather than boundary layer edge pressure
$C_w = \rho_w \mu_w / \rho_e \mu_e$	
D	diameter
h	heat transfer coefficient, (Btu/ft^2-sec-°R)
H	total enthalpy, (ft-lb/slug)
k	thermal conductivity, constant
K	constant
ℓ	length of constant plateau pressure
ℓ_{sep}	length of dividing streamline
L	length
M	Mach number
N_{CL}	distance measured along the surface from the centerline and normal to the leading edge
N_{Re,L_r}	free stream Reynolds number based upon a model reference length, L_r, (L_r = 1.22 ft for delta wing and 1.0 ft for flat plate)
N_{Re,x_e}	Reynolds number based on boundary layer edge conditions at x_e

N_{St}	Stanton number, $h/(\rho_\infty u_\infty c_{p_\infty})$
$N_{St,o}$	Stanton number on the stagnation point of a hemisphere of 1 inch diameter according to the $\rho_r\mu_r$ theory
p	normalized pressure, P/P_{HL}
P	pressure
Pr	Prandtl number
q	dynamic pressure, $\gamma PM^2/2$
$\dot{q}$	heating rate, $(Btu/ft^2\text{-sec})$
$\dot{q}_o$	heat transfer rate on the stagnation point of a hemisphere of 1-inch diameter according to the $\rho_r\mu_r$ theory
r	recovery factor
R	radius of curvature
S	distance along surface
t	time
T	temperature
u	velocity
$\bar{u}$	mean velocity
x	distance measured along surface
x_{CL}	distance measured from delta wing apex along centerline
x_e	distance from leading edge of the boundary layer growth to the beginning of pressure rise
X	normalized distance, $(x - x_{HL})/\delta^*_{HL}$
y	distance measured normal to surface
α	angle of attack
$\beta = \sqrt{M^2 - 1}$	
γ	specific heat ratio
δ	boundary layer thickness
δ^*	boundary layer displacement thickness

Δ^*	equivalent displacement thickness of separated region
ΔE	elevon deflection angle
ΔF	flap deflection angle
$\Delta \ell$	length of streamwise extent of free interaction
ΔR	rudder deflection angle
$\Delta \nu$	flow expansion angle
ε	turning angle of dividing streamline
Λ	sweep angle
μ	dynamic viscosity
ρ	density
$\tilde{\rho}$	mean density
τ	shear stress; model skin thickness
ψ	angle of yaw

Subscripts:

aw	adiabatic wall
A	aerodynamic
c	conduction; corner
corr	correction
CL	centerline
e	boundary layer edge conditions at x_e
eff	effective
F	maximum value on flap or elevon
HL	hinge line
ℓ	end of constant plateau pressure
L	laminar
m	measured

max	maximum
N	normal
PL	plateau
r	reference
ref	reference
R	conditions at point of reattachment
s	separation
T	turbulent
TE	trailing edge
w	wall
o	stagnation; tunnel total conditions
1	conditions ahead of boundary layer discontinuity
2	conditions after boundary layer discontinuity
∞	free stream condition
+	downstream
-	upstream

Superscripts:

'	model stagnation conditions
*	evaluated at the reference temperature, T*

APPARATUS AND METHODS

The X-20 experimental data presented in this report were obtained from tests of a blunt delta wing model and a sharp flat plate model in the Arnold Engineering Development Center (AEDC) tunnel B and in the Cornell Aeronautical Laboratory (CAL) 48-inch shock tunnel.[a,b,c] Reference 3 is the Cornell data report for the shock tunnel tests. A summary of test conditions for each model is presented in Table I. The pressure and heat transfer data for both of the tests discussed in this report were reduced by the wind tunnel organizations that took the data. Further reduction of the thin-skin heat transfer data from tunnel B was accomplished by The Boeing Company.

Blunt Delta Wing Model in AEDC Tunnel B

The blunt delta wing model, AD462M-1, was tested in the AEDC tunnel B. The delta wing was 14 inches long with a 73° swept cylindrical leading edge and a spherical nose cap of the same diameter as the leading edge. Two detachable bodies were provided; together with two sets of detachable tip-mounted fins with deflected rudders, and two sets of detachable deflected elevons. The AD462M-1 model configurations are shown in figure 1.

The delta wing model was electroformed of nickel with a nominal skin thickness of 0.05 inches. It was instrumented with 5 mil (#36 gage) chromel-alumel thermocouples welded to the inside of the skin and pressure taps which were connected to nine pressure transducers through a scanner valve. The thermocouples were attached on the right side of the model and the pressure taps on the left side. The bodies, fins and elevons were instrumented with pressure taps and thermocouples.

---

[a] Mauren, R.J.: Data Report - Arnold Engineering Development Center Tunnel B, Boeing Airplane Company Test No. 12 Mach 8 Heat Transfer and Pressure Test on AD462M-1, a Glider Configuration. Boeing Document D2-8045, 1961. Available on loan from The Boeing Company.

[b] Cornelius, J.R.: Data Report - Re-evaluated Heat Transfer Data from the AEDC-B-BAC-012 Test of the AD462M-1 Model. Boeing Document D2-8045-1, 1962. Available on loan from The Boeing Company.

[c] Ellison, R.K.: Turbulent Reference, Roughness, Leakage, and Deflected Surface Heat Transfer and Pressure Tests for The Boeing Company Conducted in the CAL 48" Hypersonic Shock Tunnel. Boeing Document D2-80910, 1963. Available on loan from The Boeing Company.

The AEDC tunnel B is a continuous-flow, closed-circuit, variable-density wind tunnel. The stagnation chamber air was heated by use of a propane-fired heater and was expanded to test section conditions through an axisymmetric convergent-divergent nozzle contoured for a nominal Mach number of 8. The model was supported from the rear by a sting which was fitted into a hydraulically actuated sector. The sting could be pre-bent at 3.55 inches aft of model, eliminating large sting deflections at high angles of attack.

For the heat transfer runs, the model was enclosed in cooling shoes while the tunnel was started and while angle of attack was being changed. The model was cooled by low temperature air. The cooling shoes were sufficiently large that the model could be pitched while being cooled. The retraction of the shoes required approximately 0.5 seconds from the time the shoes were fully closed until they were fully open.

Wind tunnel total pressure and total temperature were measured in the stagnation chamber upstream of the nozzle. The test-section Mach number at each stagnation pressure is defined as the average Mach number in the test-section core as determined from pitot surveys. The following empirical equation has been written to predict the tunnel Mach number as a function of total pressure (psia):

$$M_\infty = 8.125 - \frac{30}{P_o + 120} \tag{1}$$

Tunnel static conditions, P_∞, q_∞, and N_{Re}/ft, were then calculated using the perfect-gas isentropic-flow equations. The model stagnation pressure, P'_o, was calculated using the free stream Mach number and the perfect-gas normal-shock equations of reference 4.

The blunt delta wing was instrumented for heat transfer measurement with thermocouples spotwelded to the inside of the skin. The temperature was recorded every 0.05 seconds for 10 seconds. The temperature time derivative, dT/dt, was then calculated at the midpoint of a second-order "least-squares curve fit" through 21 temperature points. The local aerodynamic heat transfer rate was then calculated using the relation:

$$\dot{q}_m = \rho c \tau \left(\frac{\partial T_w}{\partial t}\right) = h_m (T_{aw} - T_w) \tag{2}$$

where ρ is the skin density, c is the skin specific heat, τ is the skin thickness, T_{aw} is the adiabatic wall (local recovery) temperature and T_w is the wall temperature. The adiabatic wall temperature was calculated from the following equation:

$$\frac{T_{aw}}{T_o} = r + (1 - r) \frac{1 + \frac{\gamma - 1}{2} M_\infty^2 \sin^2 \alpha_{local}}{1 + \frac{\gamma - 1}{2} M_\infty^2} \tag{3}$$

where α_{local} is the angle between the free stream velocity vector and the local tangent plane. The recovery factor, r, was taken as 0.85 for laminar flow and 0.90 for turbulent flow. Although equation (3) is not exact except at the wing leading edge and the stagnation point, the error will be small because of the small value of (1 - r).

All calorimeter-model heat transfer data were corrected for lateral conduction by the Thomas-Fitzsimmons method (ref. 1) which basically consists of extrapolating the curve of heat transfer coefficient versus time (or temperature) back to the start of the test run. For the blunt delta wing (AD462M-1) the test was assumed to start at the time the cooling shoes were fully open, which corresponds to t = 0.5 seconds on the temperature versus time trace. The method is illustrated by the data of figure 2. As shown, the measured heat transfer coefficient decreases steadily with time, indicating an increasing amount of heat conduction away from the thermocouple location. The parabola fitted by the method of least squares is also shown. As indicated on the plot, the time of test initiation, t_o, is 0.50 sec, leading to the corrected value denoted by the filled square. As shown, the conduction effect on the last measured heat transfer coefficient was more than 30 percent. The corrected heat transfer coefficient, h_A, is seen to be some 12 percent above the highest measured value. It is also seen to be several percent above the corrected value obtained by the more common $\nabla^2 T$ method* where the measured skin temperatures are used to calculate the conduction rates.

The symbol τ in equation (2) is the local ratio of the skin volume to the volume of the heated surface - actually, [d(skin volume)/d(skin external surface area)] - which for a flat surface is just the measured skin thickness. On models with curved skins the [d(skin volume)/d(skin external surface area)] is no longer the measured skin thickness τ but an effective thickness τ_{eff} which is a function of τ. The following correction was applied to the measured heat transfer coefficient to account for the change of skin volume per unit surface area on curved surfaces:

$$h_{corr} = \left(\frac{\tau_{eff}}{\tau}\right) h_m = \left(\frac{\rho c \tau_{eff}}{T_{aw} - T_w}\right)\left(\frac{dT_w}{dt}\right) \qquad (4)$$

For cylindrical surfaces, the measured heat transfer coefficient may be corrected approximately by:

$$\left(\frac{\tau_{eff}}{\tau}\right) = \left(1 - \frac{\tau}{2R}\right) \qquad (5)$$

---

*The Laplacian operator, ∇^2, is defined by

$$\nabla^2 = \frac{\partial^2}{\partial x^2} + \frac{\partial^2}{\partial y^2}$$

where x and y are measured in the plane of the skin, and are orthogonal.

where R is the radius of curvature. The maximum volume correction used in this report occurs on the fin leading edge. For this position,

$$\tau_{eff} = .9\tau \tag{6}$$

Sharp Flat Plate Model in Cornell Shock Tunnel

The sharp flat plate model (AD642M-1) shown in figure 3 was tested in the Cornell shock tunnel. The plate was 12 inches long and 7 inches wide with the aft 4 inches hinged to permit flap deflection either up or down. The span of the plate could be extended to 18 inches with side plates.

The plate and flap were instrumented with fourteen pressure and fourteen heat transfer gages. Eleven pairs of gages were placed near the plate centerline, the pressure on the left and heat transfer on the right. The remaining three pairs were oriented spanwise on the flap, 1.6 inches from the trailing edge, as shown in figure 3. The pressure transducers employed lead zirconium titanate piezoelectric crystals which are extremely sensitive, and incorporated a dual-element feature to eliminate the acceleration effects. The transducer output was recorded on an oscilloscope. The transducers were calibrated after installation in the model. The voltage variation was linear over the range of pressure encountered in this test. The pressure instrumentation has been described in detail in reference 5.

Heat transfer rates were measured using thin-film resistance thermometers. A thin film of platinum approximately 0.1 micron thick was painted on a pyrex substrate which had been shaped to the model contour. A thin dielectric coating was deposited on the gage surface to insulate the metallic film from ionized air flow. The gages were calibrated by measuring the change of resistance of the metal film as a function of temperature. Since its heat capacity is negligible, the film instantaneously measures the transient surface temperature of the gage. The heat transfer instrumentation has been described in detail in reference 6.

The Cornell hypersonic shock tunnel has been described in references 7 and 8. The tunnel employs a constant-area reflecting shock tube to supply air to a contoured convergent-divergent hypersonic nozzle. The "tailored interface" technique, wherein the states of the gases on either side of the shock tube driver-driven interface are matched, supplies test air for a sufficient length of time to allow accurate measurements of pressure and heat transfer rates on the model. The temperature and pressure of the stagnation chamber is determined by the initial temperature and pressure of the driven tube air and the shock Mach number. The stagnation pressure and the speed of the incident shock were measured on every run to determine nozzle supply conditions. The test section Mach number was determined for the nozzle used

by pitot pressure calibrations with the assumption that the flow was isentropic. Real gas effects were included. The test section static conditions were then calculated in a manner similar to that employed in AEDC tunnel B, as previously discussed.

DATA APPRAISAL

In some cases involving separation, pressure and heat transfer data from repeated runs disagree. After an examination of the data, the authors have concluded that separation phenomena are not always repeatable within the degree of control possible in a practical test. For example, boundary layer transition can cause large changes in the extent of separation, and cannot always be duplicated even with attached flow. In regions unaffected by separation the measurements repeat consistently. Typical examples of the data obtained are shown in figures 4 through 7.

No appreciable tunnel flow irregularities have been reported for the Cornell shock tunnel. However, the flat plate pressure data at 0° angle of attack and Mach number 6.38, shown in figure 8, are 20 percent below the inviscid calculated values for that Mach number. This could be the result of upflow in the tunnel or an angle of attack measurement error of 0.8°. Axial Mach number gradients for the Cornell shock tunnel are less than .1/ft for the Mach number 6.38 data and less than .2/ft for the Mach number 15.15 data. The AEDC tunnel B has a centerline flow which is uniform to $\pm$ 0.3%. Axial Mach number gradient is 0.01/ft according to reference 9.

REVIEW OF BASIC THEORY

Physical Considerations

Flow separation is caused by the action of an adverse pressure gradient on boundary layer flow. Because the momentum within the boundary layer is less than that of the external flow, the flow near the surface may be brought to rest or even reversed by relatively small adverse pressure gradients. The resulting changes in the boundary layer can have a large effect on the external flow. A typical example of these effects is sketched below.

(a) Inviscid flow (b) Viscous flow

With separation, the simple corner flow is replaced by an effective body shape indicated by the heavy line in sketch (b). Since the external flow is strongly affected, the analysis cannot be conducted within the framework of boundary layer theory which is based on a prior knowledge of the longitudinal pressure distribution. The actual behavior of the pressure and shear force at the surface can be determined qualitatively with the aid of sketch (b), and is shown schematically in sketch (c) below.

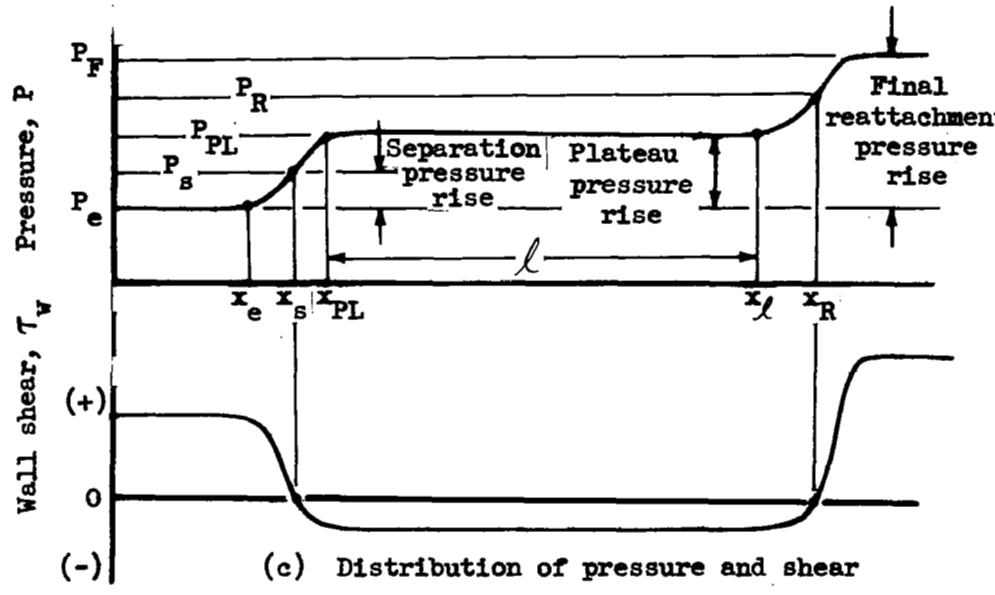

(c) Distribution of pressure and shear

As shown, the pressure for this idealized case is always rising or constant through the separation region, while the shear force becomes negative. The point of separation, defined as the first point at which $\tau_w = 0$, is seen to be well ahead of the corner, indicating that the initial pressure rise is determined by the interaction of the boundary layer with the external flow rather than the corner. The point of reattachment, x_R, is the second point of sketch (c) at which $\tau_w = 0$. In this report P_F will be used to designate the maximum pressure on the flap or elevon, whereas, in sketch (c) above, the maximum pressure after reattachment is identical to the final reattached pressure.

The fact that the separation point lies upstream of the corner simplifies the analysis somewhat, since one expects the behavior at separation to be relatively independent of the downstream flow. With the assumption that the flow at separation is independent of the details of the downstream flow, Chapman (ref. 10) demonstrated that

$$C_P \sim \sqrt{\frac{C_{f_e}}{\beta_e}} = \sqrt{\frac{C_{f_e}}{\sqrt{M_e^2 - 1}}} \qquad (7)$$

Additional assumptions used in obtaining this result are that the flow is two-dimensional and that the pressure may be predicted by linearized theory. This result has been confirmed by other investigators, both by analysis and testing. Since this result is basic to the interpretation of the tests reported herein, an outline of its derivation will be given.

Two-Dimensional Separation in Supersonic Flow

It is assumed in the analysis that there exists a dividing streamline that forms the effective boundary of the inviscid flow. The essential features of the flow field are sketched below:

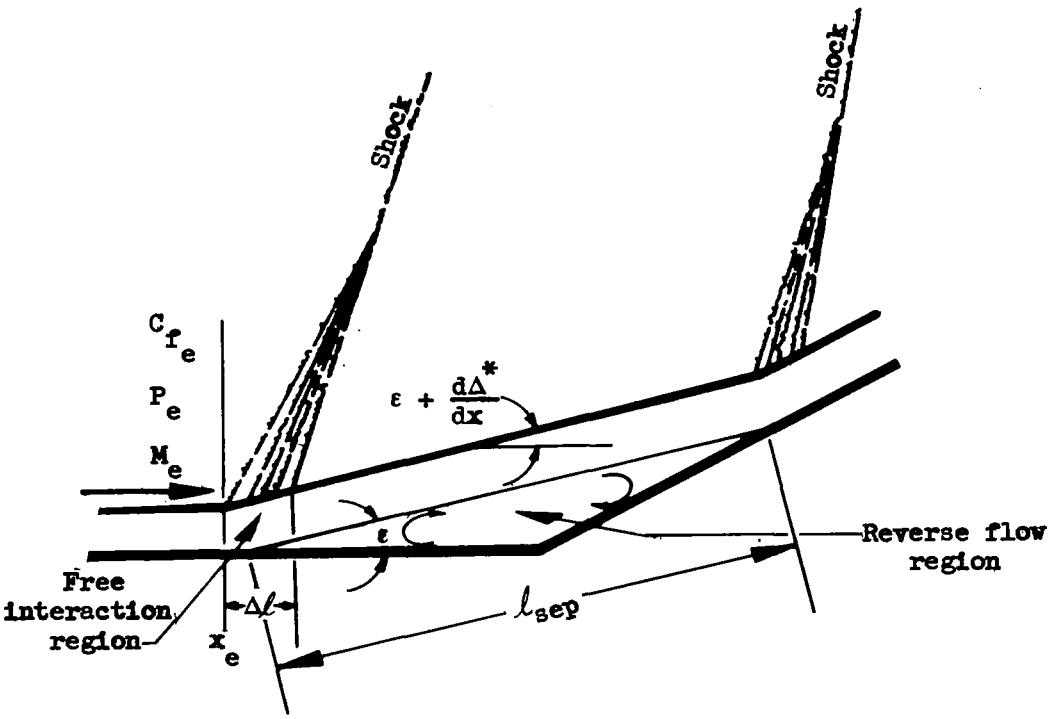

It is assumed that the interaction of the boundary layer and external flow that occurs ahead of the separated region is independent of downstream conditions. The term "free interaction" is used to describe this independence. Within the limitations of linearized theory for supersonic flow the pressure in the interaction region may be related to the growth of the boundary layer displacement thickness δ^* by:

$$C_P = \frac{P - P_e}{q_e} = \frac{2}{\sqrt{M_e^2 - 1}} \frac{d\delta^*}{dx} \tag{8}$$

where the subscript, e, refers to conditions at the boundary layer edge at the beginning of the interaction. In the separated region the pressure is nearly constant and given by

$$C_{P_{PL}} = \frac{P_{PL} - P_e}{q_e} = \frac{2}{\sqrt{M_e^2 - 1}} \frac{d\Delta^*}{dx} \tag{9}$$

where Δ^* is the equivalent displacement thickness of the separated region. If $\Delta\ell$ is the length of the streamwise extent of free interaction and if the increase in δ^* is much larger than the original value, then the order of magnitude of $C_{P_{PL}}$ is given by

$$C_{P_{PL}} = \frac{P_{PL} - P_e}{q_e} \approx \frac{1}{\sqrt{M_e^2 - 1}} \left(\frac{\delta^*}{\Delta\ell}\right) \tag{10}$$

A boundary layer momentum balance at the wall gives

$$\frac{\partial P}{\partial x} = \left(\frac{\partial \tau}{\partial y}\right)_w$$

Again by order of magnitude considerations for constant M_e

$$\frac{\partial P}{\partial x} \doteq \frac{P - P_e}{\Delta\ell} \sim \frac{\tau_w}{\delta} \sim \frac{\tau_{w,e}}{\delta^*}$$

Equation (10) now becomes

$$C_{P_{PL}} \sim \left(\frac{\tau_{w,e}}{\delta^*}\right)\left(\frac{\Delta\ell}{q_e}\right) \tag{11}$$

Multiplying equations (10) and (11) yields

$$\left(C_{P_{PL}}\right)^2 \sim \left(\frac{\tau_w}{q_e}\right) \frac{1}{\sqrt{M_e^2 - 1}} \tag{12}$$

or

$$C_{P_{PL}} \sim \sqrt{\frac{C_f}{\beta}} \tag{13}$$

To this point the derivation has required no knowledge of the boundary layer state, and so may be applied to either laminar or turbulent boundary layers. Using well known relations for the friction coefficient and introducing proportionality constants gives:

$$\left(C_{P_{PL}}\right)_L = \frac{(K_{PL})_L}{(\beta_e)^{1/2} (N_{Re,x_e})^{1/4}} \tag{14}$$

$$\left(C_{P_{PL}}\right)_T = \frac{(K_{PL})_T}{(\beta_e)^{1/2} (N_{Re,x_e})^{1/10}} \tag{15}$$

Several authors have given somewhat more detailed derivations that lead to estimates of K_{PL}. All are within the general framework just given, however, and subject to the same general restrictions.

Wall Temperature Effects

The wall temperature and the rate of heat transfer to or from the separated region may affect the separation characteristics because of the strong dependence of the transport properties on temperatures within the separated region. Curle (ref. 11) and Gadd (refs. 12 and 13) have predicted that the pressure coefficient at separation is independent of wall temperature. However, Curle predicted that the pressure gradient at separation is inversely proportional to the wall temperature and Gadd predicted that the extent of the region of interaction should be proportional to the three-halves power of the wall temperature. Later experiments of Gadd (ref. 14) showed little effect of wall temperature except under conditions of large heat transfer.

The analysis of Erdos and Pallone (ref. 15) does include wall temperature effects, provided no pressure gradient exists in the flow ahead of separation. Their results indicate a strong effect of wall temperature only for turbulent boundary layers. For turbulent flow the predicted plateau pressures were calculated from the relations given by Erdos and Pallone and include the effects of wall temperature. The laminar plateau pressures were calculated using equation (13) with the constant determined from reference 10 by Chapman, Kuehn, and Larson.

Hence,
$$\left(C_{P_{PL}}\right)_L = 2.23\sqrt{\frac{C_{f_e}}{\beta_e}} \tag{16}$$

Aerodynamic Heating With Separation

The aerodynamic heating effects of flow separation and reattachment can be large and extremely complex. In most cases predictions must be based on approximate methods. The difficulty of providing useful heat transfer information for actual design is made somewhat easier by the fact that maximum values are usually of most interest. As shown in this report, upper bound methods can often be devised.

The heat transfer through a laminar separated region was analyzed by Chapman (ref. 16) with the aid of boundary layer theory. His calculation indicated that average laminar heat transfer is reduced by about 50 percent as compared to an attached flow for the same local flow properties at the boundary layer outer edge. This result has been verified in tests of reference 17 by Larson for cavity-type flow and tests of reference 18 by Holloway,

Sterrett, and Creekmore for forward-facing steps. Although the results of reference 17 indicate that the same reduction might apply to turbulent flow, the test data of reference 18 indicate an increase in heating for transitional and turbulent separation over forward-facing steps.

Reattachment heating presents a more complex problem because of the large pressure gradient that exists throughout the reattachment region. Chung and Viegas (ref. 19) have made a calculation of the laminar boundary-layer flow at reattachment; however, a prior knowledge of the reattachment pressure gradient is required.

Two original approximate methods are used in this report. The method of the appendix is an approximate method for calculating boundary-layer interaction with an expanding or compressing flow. The second method is an upper bound estimate of reattachment heating. The very simple result obtained is

$$\frac{\dot{q}_{max}}{\dot{q}_{undisturbed}} \pm \frac{N_{St,max}}{N_{St,undisturbed}} = \frac{P_{max}}{P_{undisturbed}} \tag{17}$$

This approximate result is based on the relation:

$$N_{St} = \frac{\text{constant}}{\rho_\infty u_\infty C_{P_\infty} (Pr)^{2/3}} \frac{\rho^* \mu^{*\,1/n} u_e}{\left[\int_0^x \rho^* \mu^* u_e \, dx\right]^{1/(n+1)}} \tag{18}$$

which is a slight generalization of an equation by Lees (ref. 20). In equation (18) n is 1 for laminar flow and 4 for turbulent flow. The superscript, *, denotes evaluation at the reference temperature, T*, defined as:

$$T^* = 0.5\, T_w + 0.28\, T_e + 0.22\, T_{aw}$$

To evaluate the effect of a sudden compression on N_{St} as predicted by equation (18), we write

$$\frac{(N_{St})_+}{(N_{St})_-} = \frac{\left(\rho^* \mu^{*\,1/n} u_e\right)_+}{\left(\rho^* \mu^{*\,1/n} u_e\right)_-} \frac{\left[\int_0^{x_-} \rho^* \mu^* u_e \, dx\right]^{1/(n+1)}}{\left[\int_0^{x_+} \rho^* \mu^* u_e \, dx\right]^{1/(n+1)}} \tag{19}$$

where the subscripts + and - indicate evaluation just downstream and just upstream, respectively, of a sudden compression. If the compression occurs over a very short distance the two integrals must be nearly equal, since

$$\int_0^{x_+} \rho^* \mu^* u_e \, dx = \int_0^{x_-} \rho^* \mu^* u_e \, dx + (x_+ - x_-)\, \rho^* \mu^* u_e + \ldots$$

and for small values of $(x_+ - x_-)$

$$\int_0^{x_+} \rho^* \mu^* u_e \, dx \doteq \int_0^{x_-} \rho^* \mu^* u_e \, dx$$

so that

$$\frac{(N_{St})_+}{(N_{St})_-} \doteq \frac{\left(\rho^* \mu^{*\,1/n} u_e\right)_+}{\left(\rho^* \mu^{*\,1/n} u_e\right)_-} = \frac{\left[P\left(\mu^{*\,1/n}/T^*\right) u_e\right]_+}{\left[P\left(\mu^{*\,1/n}/T^*\right) u_e\right]_-} \qquad (20)$$

In this expression the changes in pressure are dominant. Not only do the changes in T^* and μ^* tend to compensate, but the changes in reference temperature are small, since T_w and T_{aw} will not change appreciably. Referring to wedge theory, it is found that the ratio of the local to free stream velocity varies approximately as the cosine of the deflection angle, and so is near 1.0 for angles of 30 degrees or less. Neglecting these "small" differences:

$$\frac{\left(\rho^* \mu^{*\,1/n} u_e\right)_+}{\left(\rho^* \mu^{*\,1/n} u_e\right)_-} = \frac{P_+}{P_-} \qquad (21)$$

Immediately downstream of the compression the heating rate begins to decrease as the integral in equation (18) increases. Hence, equation (17) now becomes

$$\frac{(N_{St})_+}{(N_{St})_-} = \frac{(N_{St})_{max}}{(N_{St})_{flat\ plate}} = \frac{P_{max}}{(P)_{flat\ plate}} = \frac{P_+}{P_-} \qquad (17)$$

Since no assumption has been made regarding boundary layer state, equation (17) applies in either laminar or turbulent flow. Equation (17) would also be applicable in the presence of flow separation provided no appreciable increase in the integral of equation (18) occurred over the separated region. Since the integral represents the effect of wall shear on the boundary layer growth, it seems reasonable that the small shear forces in the separated region are also negligible. In the case of separation the subscripts + and - would refer to conditions just ahead of separation and just downstream of reattachment.

Equation (21) cannot be expected to be quantitatively correct. Many important features of separation and reattachment have been neglected, particularly the effect of the reattachment pressure gradient. However, in the absence of any rigorous method, equation (21) does provide a qualitative explanation of many of the observed results.

APPLICATION OF BASIC THEORY TO THE PRESENT PROGRAM

Almost none of the idealizations used in deriving equation (16) apply in the present tests. Since the flow was hypersonic, linear theory does not correctly predict the pressure changes that occur. Induced pressure gradients existed over the model surface in the shock tunnel tests, a condition not considered in the simple analysis. Also, all models tested were of finite span so that three-dimensional flow effects are present. Although the effects of span extension on a flat plate were investigated, no end plates were used. In either case three-dimensional flow effects would exist.

Although the measured flat plate pressures without separation are compared with the viscous theory of Dewey (ref. 21), the predicted pressure rises were calculated from the faired test data levels ahead of the separated flow. No theoretical predictions for the location of the points of separation were made. However, calculated plateau pressure levels, based on equation (16) for laminar flow and reference 15 for turbulent flow, were compared with the test data. Using the measured pressures, the boundary layer edge conditions and matching theoretical separation and plateau pressure rises were determined for several axial stations aft of the leading edge, including the region where the observed pressure rises to the plateau level. Because of the low density of instrumentation, the actual point of separation was not measured nor was the character of the pressure rise to the plateau defined by the test data. Therefore, the separation point was determined as the axial station aft of the leading edge where the faired data best matched the calculated separation and plateau pressure levels.

For the flat plate test, the total pressures used for predicting the boundary layer edge conditions were determined from the tunnel conditions and oblique shock relations of reference 4. The turning angle presumed for each oblique shock was the angle associated with the pressure rise from free stream to the most forward measured pressure on the flat plate. For the delta wing, the total pressure used was that pressure calculated for a stagnation streamline on the swept blunt leading edge of the wing. The predicted plateau pressure rise for laminar separation was determined by equation (16). For turbulent flow, the plateau pressure rise was calculated using the theoretical results of Erdos and Pallone (ref. 15). The separation point was assumed to occur at a pressure rise coefficient equal to one-half of the calculated plateau pressure rise coefficient.

The measured maximum pressures after reattachment are compared with two predicted pressure levels, the attached-flow elevon pressure and the separated-flow elevon pressure. The attached-flow elevon pressure was calculated by oblique-shock theory using the flap or elevon deflection as the turning angle through the shock and based on initial conditions ahead of the shock

equal to those of the undisturbed flow at the hinge line. The pressure on the elevon for separated flow was calculated from a two-shock system by oblique-shock theory. The turning angle for the first shock was determined from the pressure rise to the separation plateau and the boundary layer edge conditions at the beginning of the rise. The turning angle for the second shock was $(\Delta E - \varepsilon)$ as shown in the sketch below. The final pressure was calculated (ref. 4) by turning the flow through the second shock from the separation plateau conditions.

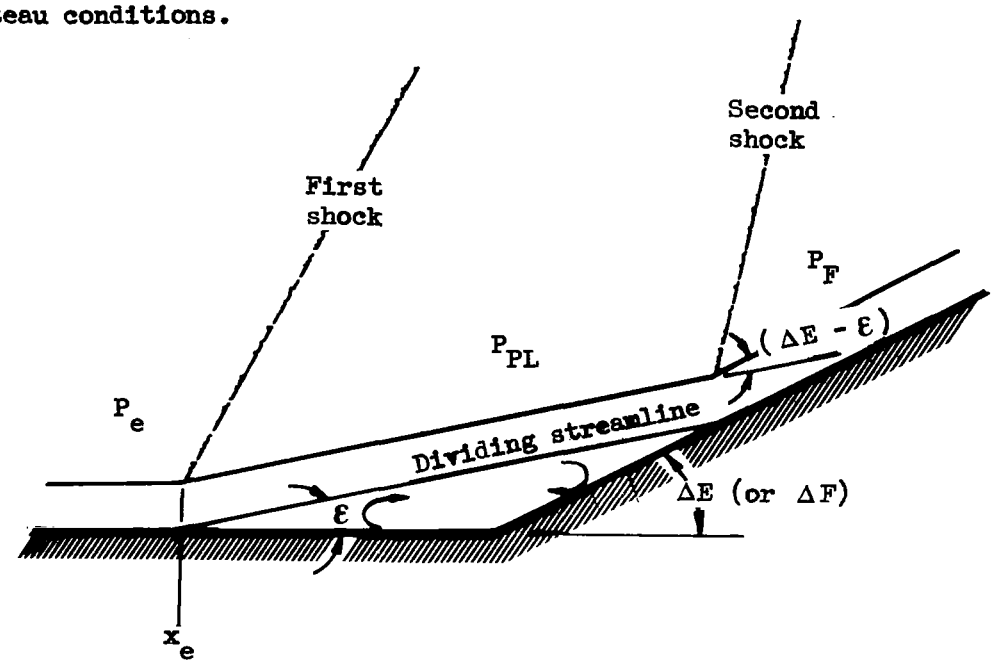

Laminar and turbulent heating rates for undisturbed flow were determined by the $\rho_r \mu_r$ method which has been described in Appendix A of reference 1. The reattachment heating rates were determined from the attached-flow pressures and equation (17). The predicted heating rates for the delta wing were calculated using the blunt delta wing leading edge shoulder value as the hinge line value and increasing it by the ratio of maximum elevon pressure divided by the delta wing lower surface value.

RESULTS AND DISCUSSION

Flat Plate Model with Deflected Flap

Pressure data - effect of flap deflection.- Pressure data from the flat plate model are presented in figures 8 through 11. Schlieren photographs are presented in figure 12. The data obtained at a Mach number of 6.38, presented in figure 8, were found to agree well with wedge theory, both on the plate ahead of the flap and on the flap for deflections of 0°, 15°, and 30°. The data show little or no indication of flow separation. With higher flap deflections, the data indicate that separation occurred. The 0° angle of attack data with 45° flap deflection show an increase in pressure well ahead of the flap and an increasing pressure trend over the entire length of the model. With 30° flap deflection, the final pressure is in good agreement with the attached-flow prediction. With 45° flap deflection the measured pressure is seen to be far below the theoretical prediction. The data of figure 8 also indicate a local minimum at $x/L_r = 0.5$ to 0.7, that is not in accordance with the simple theoretical concepts previously discussed. A similar behavior has been observed by Graham and Vas (ref. 22) and is explained by them as being associated with the generation of a small secondary vortex in a corner. As demonstrated by the test data of reference 22, the minimum is most pronounced for the flat plate model with the sharpest leading edge. The minimum does not appear in the data for the bluntest leading edge model of reference 22. Hence, the appearance of a local minimum in the present sharp flat plate data is not surprising.

At the two highest flap deflections, the data taken at Mach 6.38 with the plate at 15° angle of attack (figure 8) show a strong negative pressure gradient at the trailing edge. In neither case is the measured maximum pressure after reattachment as high as the theory predicts. However, it is seen that the instrumentation density is such that the peak value could have occurred without being measured. In the test involving 30° flap deflection, it seems probable that the peak pressure occurred at $x/L_r = .8$ and that it was near the wedge theory prediction. The theoretical predictions for figure 8(b) assume turbulent boundary layer flow since the heating data presented later show good agreement with turbulent theory.

Additional data taken at a Mach number of 15 are presented in figure 9. The negative angle of attack data with 0° flap deflection, figure 9(a), show a pressure disturbance which begins well forward of the hinge line and extends to the trailing edge of the flap. This indicates possible separation which could be induced by the shock at the trailing edge. A similar phenomena exhibited by the $\Delta F = 15°$ data produces no definable plateau pressure. The data for 30° and 45° flap deflection show reasonable agreement with the plateau pressure predictions by the method of reference 10 (eq. (16)), although in no case is there agreement with the predicted final pressure.

The viscous flat plate pressure curve, calculated by the method of Dewey, (ref. 21) gives fairly good agreement with the 0° and +15° angle of attack data. However, the -15° angle of attack data are as much as 35% below the values predicted by the method of Dewey.

Pressure data for the flat plate at 0° and +15° angles of attack are presented in figures 9(b) and 9(c), respectively. As the flap angle is increased, the separation point moves foward, the plateau pressure level rises and the length of separation increases. As shown in figure 9(b) for 15° of flap deflection at 0° angle of attack, the flow appears to remain attached. The data do not show a sudden increase at the flap hinge line as predicted by inviscid attached-flow theories. Starting at the flap hinge line, the pressure rises gradually and approaches asymptotically the inviscid pressure level at the flap trailing edge. A relation is presented in the appendix to this report, equation (A8), expressing the pressure rise in a corner for hypersonic viscous flow. This equation has coupled the inviscid and viscous flow through the use of the Newtonian pressure and the boundary layer relations presented in the appendix.

The basic assumptions involved are:

1. Boundary layer displacement thickness downstream of the corner is proportional to a power (close to unity) of the pressure.

2. The displacement thickness distribution represents the effective edge streamline along which the inviscid flow turns.

3. The inviscid pressure distribution is given by Newtonian theory.

As shown in figure 9(b), the test data are bracketed by the theoretical viscous and inviscid pressures. Although the viscous corner flow theory predicts the character trend of the data, it has underestimated the flap pressures.

The 30° and 45° flap deflection cases show measured maximum pressures after reattachment significantly below the predicted separated flow values. This could be a result of the complicated interaction between the bow shock and the separation and reattachment shocks shown in the Schlieren photograph in figure 12(g). However, it must be remembered that in any real test, the maximum observed value will generally be less than the actual maximum, which may occur at only one uninstrumented point. The steepness of the observed pressure gradients in the present test is such that the peak value could easily have occurred between the pressure gages. (e.g., the alternate data fairing shown in figures 9(b) and 9(c)).

The measured plateau pressures shown in figure 9 are seen to agree reasonably well with the predictions based on the method of Chapman:

$$C_{P_{PL}} = 2.23\sqrt{\frac{C_{f_e}}{\beta_e}} \qquad (22)$$

The procedure for using this equation to predict $C_{p_{PL}}$ has been described in the previous section.

Pressure data for negative flap deflections, presented in figure 10, are well above inviscid theory. The discrepancy is not attributed to flow separations since the pressure gradient is favorable. A simplified interaction theory described in the appendix is seen to predict the trends of the data as shown by the solid lines in figure 10. For both Mach 6.38 and Mach 15.15 the viscous effects on elevon pressures predicted by the theory are too large.

Pressure data - effect of span extension.- In order to evaluate the three-dimensional influence of a finite-span flat plate on the separation caused by a deflected control surface, the flat plate model was provided with span extensions as shown in figure 3. The chord of the flap was 4 inches and the basic span was 7 inches, giving a flap aspect ratio of $b_F/c_F = 1.75$. With a 6-inch span extension, the flap aspect ratio was increased to 3.25. None of the flat plate model configurations included end plates.

The effect of the span extensions on the pressure distribution is shown in figure 11. The corresponding heating data are presented in figure 16. The extensions caused the plateau pressure to increase and the locations of maximum pressures on the flap to move aft, except when the peak already occurred at the trailing edge. Although some of the pressure and heating data at Mach 6.38 and 0° angle of attack were not usable and not shown in figures 11(a) and 16(a), the separation is transitional with or without span extensions. However, the point of boundary layer transition has moved upstream for the extended span data. The Mach 15.15 data shown in figures 11(c) and 11(d) at angles of attack of 0° and 15°, respectively, are all laminar, regardless of span. Span extension does not appreciably affect the characteristic dip in pressure at the end of the plateau for either Mach number.

Heating data - effect of flap deflection.- The effect of flap deflection on the flat plate model heating is presented in figures 13 through 16. The heat transfer data for the zero flap deflection are compared with analytical values based on the $\rho_r \mu_r$ theory (ref. 1). These data agree well with the theory predictions for both laminar and turbulent flow.

Heating rates for the deflected flap are seen to be qualitatively similar to the pressure data. As pointed out in a previous section, this similarity is to be expected in regions of large pressure gradients, such as those existing in the present tests. The trends observed ahead of the flap are not predicted by the above considerations, however. Although at Mach 6.38, heating data ahead of the flap do show an increase in heating rate when flaps are deflected, there is usually no corresponding increase in pressure. In contrast, the Mach 15 data of figures 9 and 14 show an increase in pressure, but no increase in heating for a 30° flap deflection angle. The Mach 6.38 results, shown in figure 13, are attributed to transition, while the Mach 15 results are qualitatively consistent with the expected behavior of laminar separated flows.

Heating data for negative flap deflections are presented in figure 15. The theory curve for expansion over the flap is based on a method presented in the appendix and predicts,

$$\frac{\dot{q}}{\dot{q}_{HL}} = \frac{N_{St}}{N_{St,HL}} = \frac{P}{P_{HL}} \qquad (23)$$

The theory is seen to correlate both the laminar and turbulent pressure and heating data.

Heating data - effect of span extensions.- The effect of span extensions on the flat plate heating rates is presented in figure 16. The largest effect was observed on the flap at Mach 6.38 at 0° angle of attack, where it is seen that the heating rates were significantly reduced on the flap. When the extensions were used a less severe reattachment peak occured. The observation could not be confirmed with pressure data, due to insufficient instrumentation. The remaining plots of figure 16 show little effect of span, but are consistent with pressure data in indicating that the reattachment peak moves back as the span is increased.

The heating data at Mach 6.38 and 0° angle of attack are presented in figure 16(a). For the undeflected flap case, comparison of the data with the theory indicates boundary layer transition occurring over the last half of the plate. The pressure data agree with the laminar theory over the forward portion of the plate and rise to the turbulent theory level near the trailing edge. As was mentioned earlier, in the discussion of the corresponding pressure data of figure 11(a), with a deflected flap, boundary layer transition occurs farther upstream for the extended span case. At Mach 15.15, agreement of the heating rate data with theory indicates pure laminar boundary layer flow.

Separation on a Blunt Delta Wing

Pressures.- Pressure distributions on the lower surface of the blunt delta wing of figure 1 at Mach 8.08 along a 6° ray line (35% span) are shown in figure 17. The data are shown over a range of angles of attack from 0° to 30°. The pressure data are for elevon deflections of 20° and 45° and for the elevons removed. Data for the wing without elevons has been labeled $\Delta E = 0°$. The pressure parameter used is P/P'_o where P'_o is the model stagnation pressure (the total pressure behind a normal shock). The distance parameter, S/D, is the distance, S, along the surface on a 6° ray line, divided by the diameter, D, of the blunt leading edge. Since D is nominally equal to one inch, S/D is equal to the distance in inches. Repeat runs are indicated by flagged symbols.

The extent of separation is indicated in figure 17 by the length of the dividing streamline, ℓ_{sep}, which was estimated from observed separation points, and is shown for each case. The point of separation was determined from the data by the technique described previously for the flat plate. At the separation point on the 6° ray line of the wing, that turning angle was determined (using the oblique-shock relations of reference 4) which would correspond to the rise from the boundary layer edge conditions, across an oblique shock, to the measured plateau pressure. Assuming that on the 6° ray line the dividing streamline is straight and at the calculated turning angle to the wing, the intersection of the dividing streamline with the deflected elevon determines the point of reattachment and ℓ_{sep}. The values obtained agree well with the elevon data of figures 17 and 20.

It is shown in figure 17 that increasing the elevon deflection from 20° to 45° caused both the separation and reattachment points to move forward. The movement of the reattachment point is much less than that of the separation point, so that the length of the separated region is increased. The separation length is seen to reach a maximum at about 10° angle of attack. For elevon angles of 20° at $\alpha \geq 20°$, the area of separation apparently does not extend forward to the most aft pressure gage on the wing and is not shown.

Spanwise pressure distributions are presented in figure 18. Separation effects are shown over the entire instrumented portion of the wing span at the rearmost gage location, $x_{CL}/D = 13.44$. At $\alpha = 0°$, separation has occurred for $x_{CL}/D = 12.26$ with $\Delta E = 20°$, and for $x_{CL}/D = 9.32$ with $\Delta E = 45°$. When $\alpha = 10°$, separation has occurred for $x_{CL}/D = 7.85$ with $\Delta E = 45°$. There is also evidence of separation near the centerline at $x_{CL}/D = 9.32$ with $\Delta E = 20°$. The width of this separation increases farther downstream.

A more graphic indication of the extent of separation is provided by figure 19, in which the separated region has been indicated by shading. The separated regions were determined from the pressure distributions together with the calculated dividing streamlines of figure 17. Separated regions corresponding to two elevon settings are shown on each plot. However, both elevons had the same setting for any particular test.

At angles of attack of 0° and 5°, deflection of the elevons causes boundary layer separation over a large portion of the wing. At 5° angle of attack, 45° of elevon deflection separates all of the boundary layer flow except on the leading edge or very near the nose. It is not clear whether or not the flow remains separated in the region of the trailing edge centerline.

Heat transfer.- Heat transfer distributions at Mach 8.08 along a 6° ray line on the lower surface of the blunt delta wing are shown in figure 20. Each heat transfer distribution of figure 20 corresponds to a pressure distribution of figure 17. The data are shown over a range of angles of attack of 0° to 25°. Heat transfer data at $\alpha = 30°$ and an elevon deflection of 45° are not reported due to tunnel blockage. The heat transfer data are for elevon deflections of 20° and 45° and for the delta wing with the elevons removed. Data without elevons have been labeled $\Delta E = 0°$. The heat transfer parameter here is $N_{St}/N_{St,o}$ where N_{St} is local Stanton number and $N_{St,o}$ (calculated by the $\rho_r \mu_r$ method) is the Stanton number corresponding to the model stagnation conditions and model thickness. The distance parameter, S/D, is the same as used in figure 17. Repeat runs are noted by flagged symbols.

All of the distributions shown in figure 20 exhibit a characteristic trend. The separated heating rates are below the no-elevon values in the forward part of the separated region but rise rapidly just ahead of the elevon hinge line. This trend is similar to that shown by the transition data of Sterrett and Holloway in reference 23, and may indicate transitional flow in the present tests. The measured heating rates in the separated region are not always repeatable, as is shown by the data for 45° of flap deflection in figures 20(b) and 20(h). The corresponding pressure data in figures 17(b) and 17(h), respectively, demonstrate much better repeatability. The poorest repeatability seems to occur near the start and end of separation. Again, this could be caused by the randomness of transition, particularly in evidence for the 0° angle of attack case of figure 20(a).

The dividing streamlines which were determined from the pressure data are shown again for comparison with the heat transfer data. The overall agreement of the pressure and heat transfer data with respect to the observed locations of separation and reattachment is good. In a few cases, such as figures 20(c) and 20(d), the heat transfer data show the effects of a disturbance somewhat upstream of the location indicated by the pressure data of figures 17(c) and 17(d). The pressure and heat transfer data were taken on the same model, but at different times in the test run. When the heat transfer data were taken, the model was enclosed in cooling shoes while the angle of attack was varied. However, for the pressure data, the cooling shoes were not used when test parameters were changed. Therefore, the pressure data represent a higher wall temperature to total temperature ratio. Since wall cooling tends to reduce the extent of separation, the expected effect of wall temperature would lead to larger separated areas for the pressure test data.

Elevon pressures and heating.- Elevon pressure and heating data are presented in figures 21 and 22. The pressure data, figure 21, are compared to oblique-shock theory for the local flow conditions. For reference, the calculated hinge line pressure for no flap deflection is also shown.

The data are seen to fall between the two theory curves, and indicate a large variation in pressure over the elevon. The variation is largest at low angles of attack and the largest elevon deflection. However, the upper bound of the data is seen to be predicted well by the attached flow (oblique-shock) theory. It will be noted that for an elevon deflection of 45° both the theory and the data indicate local pressures approximately three times the stagnation point value. This result reflects the high dynamic pressure that exists behind the main wing shock wave. It is noted that the pressure at the outboard tip of the elevon is consistently high and in good agreement with the attached flow theory, while the inboard gages indicate pressures that are usually an order of magnitude lower. This behavior is consistent with the previous information regarding the extent of separation. At the highest angle of attack with 20° of elevon deflection, it is seen that the pressures are nearly constant and in agreement with the attached flow prediction, confirming the earlier statement regarding the absence of separation for this condition. Based on the data of figure 21, it appears that attached flow theory provides a good prediction of maximum pressures after reattachment, even in the presence of extensive separation.

The corresponding heat transfer data are presented in a similar manner in figure 22. The data show trends that are very similar to those shown by the pressure data. However, the details of the heating distribution are somewhat different with the point of maximum heating at or near the elevon midspan in many cases. As with the pressures, the maximum heating rates on the elevon exceed stagnation point values for 45° of elevon deflection. The lowest heating rates occur at the inboard trailing edge in nearly all cases.

The application of equation (17) to delta wing elevon heating is complicated by the three-dimensionality of the flow. Heating rates vary considerably along the hinge line, so that the choice of an undisturbed value is dependent on the location at which the method is to be applied. If an upper bound is desired, the maximum hinge line value should be used. For the subject blunt delta wing, the maximum hinge line value is predicted to occur at the leading edge shoulder. This value, multiplied by the theoretical pressure ratio shown in figure 20, is shown in figure 21 as "Attached flow theory". The agreement of this method with the data is seen to be poor at low angles of attack. The agreement improves with angle of attack with the upper bound well predicted for $\Delta E = 20°$ and angles of attack from 20° to 30°. The agreement with the data for $\Delta E = 45°$ also improves with angle of attack, but the theory still exceeds the highest measured value by about 50% at the highest angle of attack.

The comparison indicates that the theory used here greatly overpredicts the data for most conditions. It is, of course, possible that much higher heating rates occurred than were measured. Considering the tremendous range of the measured values and the limited number of instruments, it is

virtually certain that higher values did occur and were not measured. According to the theory used here, the maximum heating rate should occur at the outboard tip of the elevon, a conclusion that is in agreement with the data. With only two thermocouples in that region the existence of local values approaching the theory is not precluded.

At high angles of attack, the undisturbed hinge line values are much more uniform, so that the uncertainty in the application of equation (17) is much less.

Comparison of Plateau Pressures and Separation Lengths

Plateau pressure.- Plateau pressure data from the present program are summarized in figure 23, together with theoretical predictions of references 10, 15, 23, and 24. The flat plate data are seen to agree well with the predictions (also shown in figure 9). The blunt delta wing data are seen to generally fall below the flat plate theory. As noted previously, the finite-span flat plate data indicate that three-dimensional effects reduce plateau pressures. A larger effect is to be expected for the delta wing data.

As shown in figure 17, the blunt delta wing data exhibit a favorable pressure gradient ahead of the separation. Following the practice of reference 22, the pressure coefficients were recomputed as referenced to an initial pressure that ignored the induced pressure gradient. The correlation with the flat plate results are improved but are still lower than the predictions, indicating that the reduction is due to three-dimensional flow effects. This conclusion is confirmed by the good agreement of the flat plate data with the theory in spite of the strong induced pressure gradients, (e.g., fig. 9).

Figure 24 presents the plateau pressure data plotted versus edge Mach number from the beginning of the pressure rise to the separation point. Again, most of the delta wing data fall far below the flat plate data or the appropriate two-dimensional theory line.

Length of separated flow region.- Comparisons have been made of the length of separated flow observed in the present tests with the theoretical predictions. These comparisons are presented in figure 25. Figure 25(a) shows a correlation of present data with the following expression of Erdos and Pallone (ref. 15).

$$\left(\frac{\ell_{sep}}{\delta_e}\right) = \left(\frac{\ell_{sep}}{\delta_e}\right)_{ref}\left(\frac{\varepsilon_{ref}}{\varepsilon}\right) = K\left(\frac{P_F - P_{PL}}{P_e}\right)\left(\frac{\varepsilon_{ref}}{\varepsilon}\right) \qquad (24)$$

In addition to the data of this report, some data by Hakkinen et. al. (ref. 24), Putnam (ref. 25) and Pate (ref. 26) are also shown. There is seen to be very little agreement with anything except the original correlation of reference 24 data shown by Erdos and Pallone. However, since there appears to be a Mach number effect, equation (24) was re-examined. Combining equation (24) with equation (8) leads to

$$\left(\frac{\ell_{sep}}{\delta_e}\right)_L \left(\beta_e\right)^{1/2} = K_L\left(\frac{P_F - P_{PL}}{P_e}\right)\left(N_{Re,x_e}\right)^{1/4} \frac{\left(\beta_e\right)_{ref}^{1/2}}{\left(N_{Re,x_e}\right)_{ref}^{1/4}} \quad (25)$$

and

$$\left(\frac{\ell_{sep}}{\delta_e}\right)_T \left(\beta_e\right)^{1/2} = K_T\left(\frac{P_F - P_{PL}}{P_e}\right)\left(N_{Re,x_e}\right)^{1/10} \frac{\left(\beta_e\right)_{ref}^{1/2}}{\left(N_{Re,x_e}\right)_{ref}^{1/10}} \quad (26)$$

The reference conditions and constants used by Erdos and Pallone are

$$\left.\begin{aligned} K_L &= 105 \\ M_e &= 2 \\ N_{Re,x_e} &= 0.2 \times 10^6 \end{aligned}\right\} \quad \text{for laminar flow} \quad (27)$$

and

$$\left.\begin{aligned} K_T &= 4.15 \\ M_e &= 2.8 \\ N_{Re,x_e} &= 2.0 \times 10^6 \end{aligned}\right\} \quad \text{for turbulent flow} \quad (28)$$

These values are used in equations (25) and (26) to obtain:

$$\left(\frac{\ell_{sep}}{\delta_e}\right)\left(\beta_e\right)^{1/2} = 6.52\left(\frac{P_F - P_{PL}}{P_e}\right)\left(N_{Re,x_e}\right)^{1/4} \quad \text{for laminar flow} \quad (29)$$

and

$$\left(\frac{\ell_{sep}}{\delta_e}\right)\left(\beta_e\right)^{1/2} = 0.178\left(\frac{P_F - P_{PL}}{P_e}\right)\left(N_{Re,x_e}\right)^{1/10} \quad \text{for turbulent flow.} \quad (30)$$

The data of figure 25(a) are presented in figure 25(b) plotted according to the relation indicated by equation (29). There appears to be little improvement in correlation over figure 25(a).

Hakkinen, Greber, Trilling, and Abarbanel (reference 24) have derived a semi-empirical relation for the length of the constant-pressure separated region. Their relation is

$$\left(\frac{\ell}{x_\ell}\right)\left(1 - \frac{\ell}{x_\ell}\right)^{-(1/8)} = 2.53 \left(1 + \frac{\gamma - 1}{2} r M_e^2\right)^{3/2} \left(\beta_e\right)^{-(1/4)} \left(C_{f_{x_\ell}}\right)^{1/4} \left(C_{P_F} - 1.21 C_{P_{PL}}\right) + 0.097 \qquad (31)$$

which can be written in a more convenient form:

$$\frac{\left(\frac{\ell}{x_\ell}\right) - 0.097\left(1 - \frac{\ell}{x_\ell}\right)^{1/8}}{\left(1 - \frac{\ell}{x_\ell}\right)^{1/4}} = 2.53 \left(\frac{T_{aw}}{T_e}\right)^{3/2} \left(\frac{C_{f_e}}{\beta_e}\right)^{1/4} \left(C_{P_F} - 1.21 C_{P_{PL}}\right) \qquad (32)$$

This relation has been plotted in figure 25(c) together with the Mach 10 data of Putnam, and the sharp flat plate and blunt-delta wing X-20 data. The correlation of the data is poor. However, modifying the constant from 2.53 to 0.08 greatly improves the agreement, particularly with Putnam's data. However, the X-20 data are still badly scattered.

The final plot of figure 25 presents an empirical correlation that was suggested by the Erdos and Pallone parameter. The correlation is seen to be more successful than the previous attempts, although considerable scatter still exists.

Interference

Tests were performed at Mach 8.08 in AEDC tunnel B on representative X-20 configurations; including a composite wing-body model and a wing with fins and rudders. The composite wing-body simulated the X-20 forward center body containing the pilot's windshield. Pressure and heating data were taken at the center of the windshield, on the upper surface of the wing in the region of the body-wing junction, and along the fin leading edges.

Windshield pressures and heating.- Pressures measured at the center of the windshield are presented in figure 26 for angles of attack from -10° to +20°. The data for +5°, 0°, and -5° angle of yaw are shown. Figure 1(c) shows the location of the pressure tap.

In order to interpret the flow mechanics associated with the experimental data, it was necessary to compare the test data with theory for various flow models depending upon the angle of attack range. The shaded band in figure 26 represents the locus of theoretical calculations which correspond to the experimental data. As could be expected, at negative angles of attack where the windshield approaches a 90° inclination to the free stream, the pressure approaches the normal shock value. At 0° angle of attack the pressures agree with either of two flow models: first, a two-shock compression consisting of a 16° cone followed by a 16° wedge; and secondly, a normal shock and expansion to the shoulder followed by a two-shock compression consisting of two 16° wedges. At +10° to +20° angle of attack the flow appears to be separated at the shoulder. The theory line which agrees with the data in this region was based upon a normal shock and expansion followed by separation at the shoulder with plateau pressure levels corresponding to equation (14). Within the small scatter of the data shown in figure 26 it is difficult to isolate any effects of the small yaw angles.

Stanton numbers measured on the windshield are presented in figure 27(a) for 0° of yaw, and in figure 27(b) for $\pm$ 5° of yaw. Although these heating data are associated with the pressure data of figure 26, the thermocouple locations on the model windshield were on either side of the pressure tap which was on the centerline. Figure 1(c) shows the dimensional location of the instrumentation. For the 0° yaw case, the heating follows the trends of the pressures. The predicted heating presented in figure 27(a) was determined from the calculated pressures of figure 27(b) by the following relation:

$$\left(\frac{N_{St}}{N_{St,o}}\right) = \left(\frac{3}{8}\right)\left(\frac{P}{P'_o}\right) \tag{33}$$

where the constant, $\frac{3}{8}$, was determined empirically.

This technique was suggested by the analysis presented earlier in this report of the effects of flap deflection on model heating. The correlation of the predicted heating by this technique to the measured Stanton numbers is excellent. The predicted heating matches the measured heating as well as the original calculated pressures match the measured pressures.

The windshield heating for the yawed conditions is presented in figure 27(b). The predicted heating for the unyawed condition lies between the heating measured on either side of the windshield centerline. The windward gage indicates the highest heating rate in all cases.

Shielding of the windshield at positive angles of attack is demonstrated by figures 26 and 27. At angles of attack greater than 10°, shielding has reduced the heating and pressures on the windshield by at least one-order of magnitude.

Upper surface wing heating.- Heating rates on the leeward surface of the blunt delta wing-body model, as shown in figure 1(c), are presented in figure 28. Data are shown in terms of faired contours to clarify the presentation.

As the angle of attack increases from 5° to 20°, the maximum heating rates are seen to decrease by more than 50%. With the wing at 5° angle of attack, the heating rates are greatest near the leading edges and decrease in the aft and inboard directions.

With the wing at higher angles of attack, the heating rates over the forward portion of the wing behave in a similar fashion, with the largest heating rates at the leading edge and forward along the body. However, as shown in figures 28(b) and 28(c), two distinct peaks in heating rate occur at approximately 35% and 70% span at the trailing edge of the wing. At the highest angle of attack the inboard peak has disappeared.

The flow exhibiting the two peaks appears to be somewhat similar to the flow field produced by a shock from a two-dimensional wedge impinging on a flat plate. This case has been investigated by Gulbran, Redeker, Miller and Strack in reference 27. A flow field sketch from reference 27 is reproduced here because of its apparent similarity to the delta wing upper surface flow in the presence of the body.

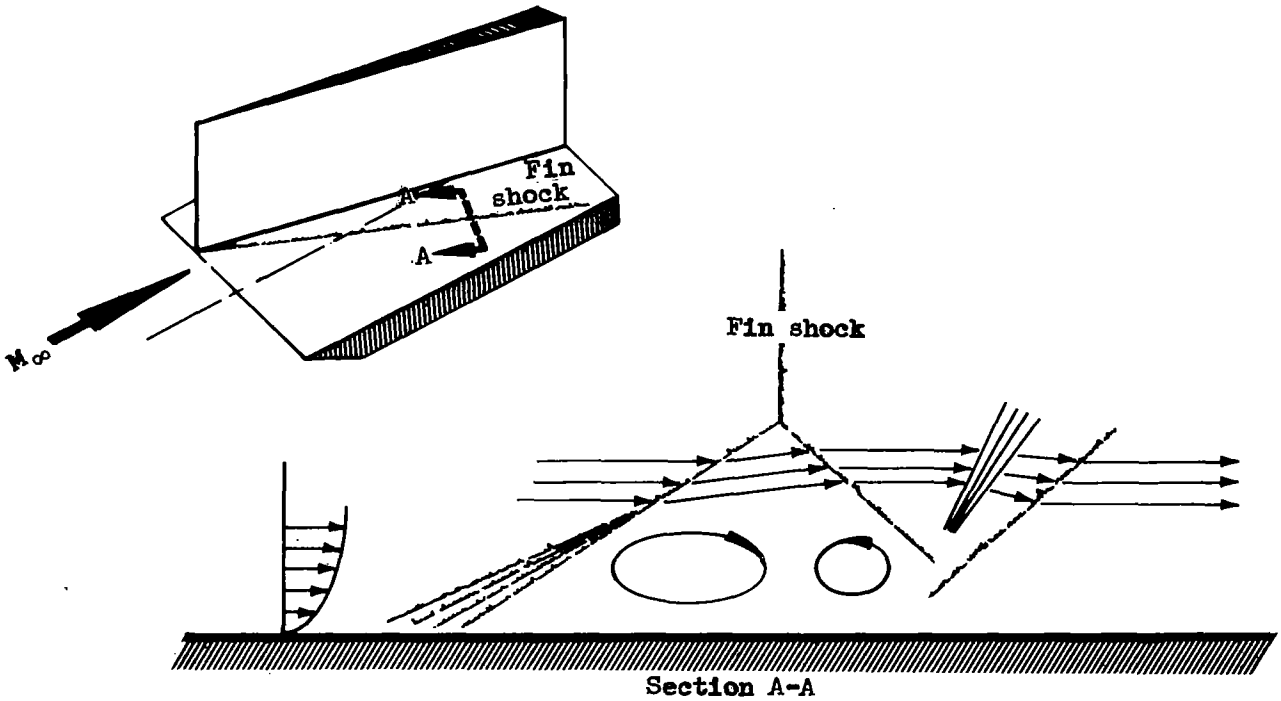

Section A-A

In the delta wing-body flow field the body shock wave corresponds to the fin shock in the sketch on page 31. The impingement of this shock on the wing boundary layer would lead to an interaction of the type observed in reference 27 with secondary vortices as shown. The impingement of the streamlines separating the two vortices could produce the high heating rates observed near the body.

Fin leading edge pressures and heating.- Pressures and heating rates were measured along the leading edge of a swept fin attached to the blunt delta wing model. Details of the configuration are presented in figure 1(b).

Fin leading edge pressures are presented in figure 29 for angles of attack from 0° through 20°. The data are in general agreement with theoretical pressure trends on an isolated swept cylinder. The effect of rudder deflection on fin leading edge pressure is negligible. The difference between the faired curves in figure 29 indicates that a disturbance caused by the wing bow shock has interfered with the fin flow field. At 0° angle of attack the aft (outboard) fin pressure data agree with the calculated isolated swept cylinder stagnation line value. At angles of attack less than 10° the bow shock disturbance has increased the fin leading edge pressures on the forward (inboard) pressure tap. At 10° angle of attack, the disturbance has moved outboard and both fin leading edge pressures are the same.

Heating rate data along the fin leading edge, which correspond to the pressure data of figure 29, are shown in figure 30. All of these data are considerably lower than the isolated swept cylinder theoretical values. However, later tests of complete configurations with denser instrumentation produced much higher heating rates on the fin leading edge. Although no effect of rudder deflection on pressure data was observed, the heating rate data show a general increase with increased rudder deflection from 20° to 45°. In most cases, a heating maximum occurs at opposite ends of the fin leading edge for the two rudder deflections. Maximum heating occurs inboard for a rudder deflection of 20°. The dashed line in figure 30 was faired through the data taken at the inboard gage with 20° of rudder deflection. Using the ratio of the measured pressures at the inboard and outboard locations on the fin leading edge, the effect of bow shock disturbance on heating rates was predicted as shown in figure 30. The ratio of heating rates was determined after equation (21), and may be stated as

$$\frac{(N_{St})_{inboard}}{(N_{St})_{outboard}} = \frac{(P)_{inboard}}{(P)_{outboard}} \tag{34}$$

CONCLUDING REMARKS

An analysis has been made of the hypersonic flow separation and interference data at Mach 6, 8, and 15 taken from tests conducted in the X-20 program. The models tested included a sharp flat plate with deflected flaps, and a blunt delta wing with body, elevons, fins and rudders. The flat plate was tested at Mach numbers of 6.38 and 15.15 and at nominal Reynolds numbers of 1.4×10^7 and

1.12×10^5, respectively. Test angles of attack were -15°, 0° and +15° with flap deflections of -45°, -20°, 0°, +15°, +30°, and +45°. The blunt wing was tested at a Mach number of 8.08 at a nominal Reynolds number of 1.2×10^6. The delta wing was tested with windward elevon deflections of 20° and 45° at angles of attack up to 30°. Tests were made on the body-wing combination at angles of attack from -10° to +20°.

Separation did not occur on the sharp flat plate at Mach 6.38 with a flap deflection of 15°; with 30° flap deflection, a slight separation may have occurred at 0° angle of attack. At 45° flap deflection, separation occurred well ahead of the flap. Heating rate comparisons indicate that the flow ahead of the flap was laminar or transitional. At Mach 15.15, laminar separation occurred with all flap deflections. The extent of separation was very small for 15° of flap deflection at 0° angle of attack.

The sharp flat plate plateau pressure data are generally in good agreement with the predictions of theories developed for much lower Mach numbers. The relation

$$C_{P_{PL}} = 2.23\sqrt{\frac{C_{f_e}}{\beta_e}}$$

was found to agree with measured plateau pressures to within about 25% at local Mach numbers up to ~12. This agreement was observed even in tests with large favorable pressure gradients ahead of the separation. However, no reliable means of predicting the location of the separation point or the length of separation was found.

The plateau pressures were nearly constant over the length of the separation. However, many cases exhibited a slight minimum near the hinge line that is not predicted by the basic theories. It appears that the observed minimum is attributed to the generation of a secondary vortex within the separation.

Maximum pressures after reattachment on the flat plate were generally at or below wedge theory predictions. In those cases where maximum pressures after reattachment were well below wedge theory, very large pressure gradients were often present, indicating that the peak values may have occurred at uninstrumented locations.

Maximum heating distributions after reattachment were qualitatively similar to maximum pressure ratios after reattachment. Maximum heating rates were generally equal to or less than maximum values calculated for attached flow. These calculated maximum values are based on heuristic arguments suggesting that

$$\frac{(N_{St})_{max}}{(N_{St})_{undisturbed}} = \frac{(P)_{max}}{(P)_{undisturbed}}$$

Maximum calculated values were exceeded by the flat plate data only when transition occurred between the separation and reattachment points.

The delta wing data show extensive separation due to elevon deflection at low angles of attack in spite of the small size of the elevons. The chord of the elevons was only 10% of the wing root chord and they were separated by a gap that was approximately 20% of the wing span. At 10° angle of attack virtually the entire wing was in separated flow with elevon deflections of either 20° or 45°. At a 20° angle of attack, the extent of separation was greatly reduced but still extended to 20% of the model length or more. The plateau pressures on the delta wing were found to be generally well below the theoretical predictions. This is attributed to three-dimensional flow effects since the flat plate model exhibited a slight but similar result, that was reduced by increasing the model span.

As on the flat plate model, maximum pressures after reattachment were well predicted by local oblique-shock theory assuming attached flow. The corresponding heating predictions based on the above relation were much above the data in most cases. Good agreement was obtained for angles of attack from 20° to 30° with an elevon deflection of 20°. In the other cases the measurements take on a very wide range of values. The heating distribution is characterized by extreme gradients, indicating that much higher values could have occurred at uninstrumented locations.

Data from the wing-body and wing-fin combinations indicate extremely complicated flow fields that defy analysis. However, the windshield heating rate data were found to be directly proportional to the measured pressure over the entire range of angles of attack.

APPENDIX

PRESSURE AND HEATING ON EXPANSION AND COMPRESSION SURFACES

The expansion of a hypersonic flow about a sharp corner can be strongly affected by the presence of a boundary layer. The effective turning angle of the flow external to the boundary layer is reduced because of the boundary layer growth, as shown in the sketch below:

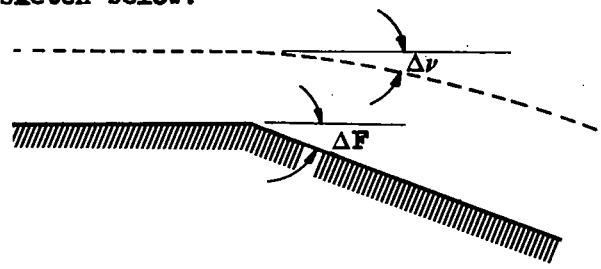

The assumption is made that the effective expansion angle may be approximated by

$$\Delta\nu = \Delta F - \frac{d\delta^*}{dx} \tag{A1}$$

where $\Delta\nu$ is the inviscid flow expansion angle, ΔF is the surface angle, and δ^* is the boundary layer displacement thickness. The calculation of the flow in the expansion region is seen to require the simultaneous solution of the boundary layer equations and a Prandtl-Meyer expansion. Because of the complexity of such a calculation, simpler methods were sought.

Behavior of the Boundary Layer in Hypersonic Expanding Flow

The boundary layer in the expansion region will respond to changes in external pressure, temperature, and velocity. However, for a hypersonic flow the effect of pressure will be dominant. For example, the velocity increase in expanding an ideal diatomic gas from a Mach number of 5.0 to any higher Mach number is less than 10%. The changes in boundary layer edge temperature will be large, but the change in the mean boundary layer temperature will also be relatively small. The temperature change may be estimated with the aid of the reference temperature formula of Eckert (ref. 28)

$$T^* = 0.5\ T_w + 0.22\ T_{aw} + 0.28\ T_e \tag{A2}$$

The recovery temperature, T_{aw}, which is much larger than the edge temperature, T_e, changes very little in an expanding hypersonic flow, greatly reducing

the effect of changes in T_e. The actual effect, based on a recovery factor of 0.85 for an expansion from Mach 5.0 to Mach infinity, is as follows:

	T_w/T_o		
	0	.5	T_{aw}/T_o
T^*/T_o at M = 5	.2758	.5258	.7133
T^*/T_o at $M \to \infty$	.1872	.4372	.612

It is seen that the largest possible change is about 30%, under conditions for which the pressure would decrease to zero.

In contrast, the boundary layer thickness must depend strongly on the pressure. The requirement that the boundary layer mass flow (which increases with distance in ordinary flows) does not decrease in the expansion, leads to

$$\int_0^{\delta} \rho\, u\, dy \geq \left[\int_0^{\delta} \rho\, u\, dy\right]_{HL} \tag{A3}$$

Approximating the integral by mean values

$$\bar{\rho}\,\bar{u}\,\delta \geq \bar{\rho}_{HL}\,\bar{u}_{HL}\,\delta_{HL} \tag{A4}$$

From the previous discussion, changes in velocity and in the mean boundary layer temperature, T*, are relatively small, so that approximately

$$\delta\, P \geq \delta_{HL}\, P_{HL} \tag{A5}$$

Use of the equal sign in equation (A5) is equivalent to neglecting boundary layer growth as a function of distance. Since the normal growth of the boundary layer reflects the integrated effect of the shear force at the wall, the effect will be small if the region of calculation is small compared to the leading edge distance. Further, the thickening of the boundary layer implied by equation (A5) must be accompanied by a decrease in wall shear force. If it is assumed that the boundary layer profiles remain similar through the expansion and that the effects of velocity changes and external temperature changes can be neglected, there results

$$\frac{\tau}{\tau_{HL}} \doteq \frac{P}{P_{HL}} \tag{A6}$$

The percentage boundary layer growth in the expansion region can then be estimated by the expression on the following page.

$$\frac{\int_{HL}^{TE} \tau \, dx}{\int_{0}^{HL} \tau \, dx} \doteq \frac{-P(x_{HL} - x_{TE})}{P_{HL} \, x_{HL}}$$

For the present tests, the estimated increase in the distance integral of the wall shear force is less than 10%, and is neglected. The arguments for equation (A6) also imply that

$$\frac{\dot{q}}{\dot{q}_{HL}} = \frac{P}{P_{HL}} \tag{A7}$$

a result that was used in figure 15.

Expanding Flow Calculation

Based on the above reasoning, it is assumed that

$$\frac{\delta^*}{\delta^*_{HL}} = \left(\frac{P}{P_{HL}}\right)^{-n} \tag{A8}$$

where P is the local pressure and the subscript, HL, denotes values at the hinge line. The exponent n is taken to be constant for any particular calculation. Differentiating equation (A8) and combining the result with equation (A1) leads to

$$\Delta\nu = \Delta F + \frac{n(P_{HL}^{\,n} \, \delta^*_{HL})}{P^{(n+1)}} \frac{dP}{dx} \tag{A9}$$

Nondimensionalizing equation (A9) with respect to hinge line values,

$$\Delta\nu \doteq \Delta F + \frac{n}{p^{(n+1)}} \frac{dp}{dX} \tag{A10}$$

in which

$$p = P/P_{HL} \quad \text{and} \quad X = (x - x_{HL})/\delta^*_{HL}$$

Equation (A10) establishes a relation between the pressure gradient and the inviscid flow expansion angle as determined from the boundary layer equation (A8).

A second equation is now required to express the inviscid relation between the flow expansion angle, $\Delta\nu$, and the pressure. For expanding flow, the Prandtl-Meyer function tabulated in reference 4 was used.

Method of Integration

It was necessary to integrate equation (A10) numerically. It was found most convenient to treat X as the dependent variable. The derivation of a formula suitable for numerical treatment, with n = 1, is as follows

$$dX = \frac{1}{(\Delta\nu - \Delta F)p^2}\, dp \tag{A11}$$

writing equation (A11) numerically and using barred quantities for averages over the interval X

$$X_{j+1} - X_j = \frac{(p_{j_{HL}} - p_j)}{(\overline{\Delta\nu} - \Delta F)\bar{p}^2} \tag{A12}$$

The averaged values are approximated by using the geometric mean pressure

$$\bar{p} = \sqrt{(p_j)\,(p_{j+1})} \tag{A13}$$

and evaluating $\Delta\nu$ at the mean pressure

$$\overline{\Delta\nu} = \Delta\nu(\bar{p}) \tag{A14}$$

Combining equations (A12), (A13), and (A14) gives

$$X_{j+1} = X_j + \frac{\left[(p_j/p_{j+1}) - 1\right]}{\left[\Delta F - (\overline{\Delta\nu}_j)\right]p_j} \tag{A15}$$

Equation (A15) is conveniently integrated by selecting a constant value of p_{j+1}/p_j. With this ratio specified, all values of p_j and $\overline{\Delta\nu}_j$ are determined and it only remains to calculate the values of X_j. The initial value of $\Delta\nu = 0$ is established by the requirement that dp/dX be finite at the hinge line.

Application to Compression Flow

Although the discussion leading to (A10) is not entirely applicable in compression flows, it is interesting to compare the method with data from the present report.

For compression flows (ΔF negative), isentropic compression is not to be expected and for this case Newtonian theory was used to calculate the local pressure.

$$C_p = 2 \sin^2 \Delta\nu \tag{A16}$$

where, as before, $\Delta\nu = \Delta F - (d\delta^*/dx)$. In this case both ΔF and $d\delta^*/dx$ are negative. With the approximation $(\sin \Delta\nu) \approx (\Delta\nu)$, there results

$$\frac{d\delta^*}{dx} = - \delta^*_{HL} \left[\Delta F - \sqrt{\frac{p - 1}{\gamma (M_{HL}^2)}} \right] \tag{A17}$$

again differentiating equation (A8) and combining the result with equation (A17)

$$\frac{dp}{dX} = \left(\frac{p^{n+1}}{n} \right) \left\{ \Delta F - \left[\frac{p - 1}{\gamma (M_{HL}^2)} \right]^{1/2} \right\}$$

and therefore,

$$X = \int_{p=1}^{p=P/P_{HL}} \frac{n}{p^{(n+1)} \left\{ \Delta F - \left[\frac{p - 1}{\gamma (M_{HL}^2)} \right]^{1/2} \right\}} dp \tag{A18}$$

Equation (A18) may be integrated numerically. In closed form (for $n = 1$) it becomes

$$X = \left(\frac{3}{2\Delta F} \right) + \left[\frac{\gamma}{3} (M_{HL}^2) \Delta F \ln \Delta F \right] - \left(\frac{3}{2\Delta F\, p} \right) - \left(\frac{3}{4\Delta F} \ln p \right)$$

$$- \frac{1}{2} \left[\gamma (M_{HL}^2) \right]^{1/2} (p - 1)^{1/2} - \frac{\gamma}{2} (M_{HL}^2) \Delta F \ln \left\{ \Delta F - \left[\frac{p - 1}{\gamma (M_{HL}^2)} \right]^{1/2} \right\}$$

Model type	Test facility	Free-stream Mach number, M_∞	Free-stream Reynolds number, N_{Re,L_r}	Reference length, L_r, ft	Incident shock Mach number	Nozzle supply stagnation pressure, P_o, psia	Total enthalpy, H_o, ft-lb/slug	Model temp., T_w, °R	Laminar reference heating rate, $\dot{q}_o$, Btu/ft^2-sec	Laminar reference Stanton number, $N_{St,o}$	Angle of attack, α, degrees	Angle of yaw, ψ, degrees
AD462M-1 Blunt delta wing	AEDC tunnel B	8.08	1.202×10^6	1.22	——	200	7.5×10^6	500	11.56	.0277	-10 to +30	-5,0,+5
AD642M-1 Sharp flat plate	Cornell shock tunnel	6.38	14.040×10^6	1	2.81	3900	13.5×10^6	520	197	——	0 to +15	0
		15.15	$.112 \times 10^6$	1	4.20	1380	27.1×10^6	520	32.8	——	-15 to +15	0

TABLE I.- NOMINAL WIND TUNNEL FLOW CONDITIONS

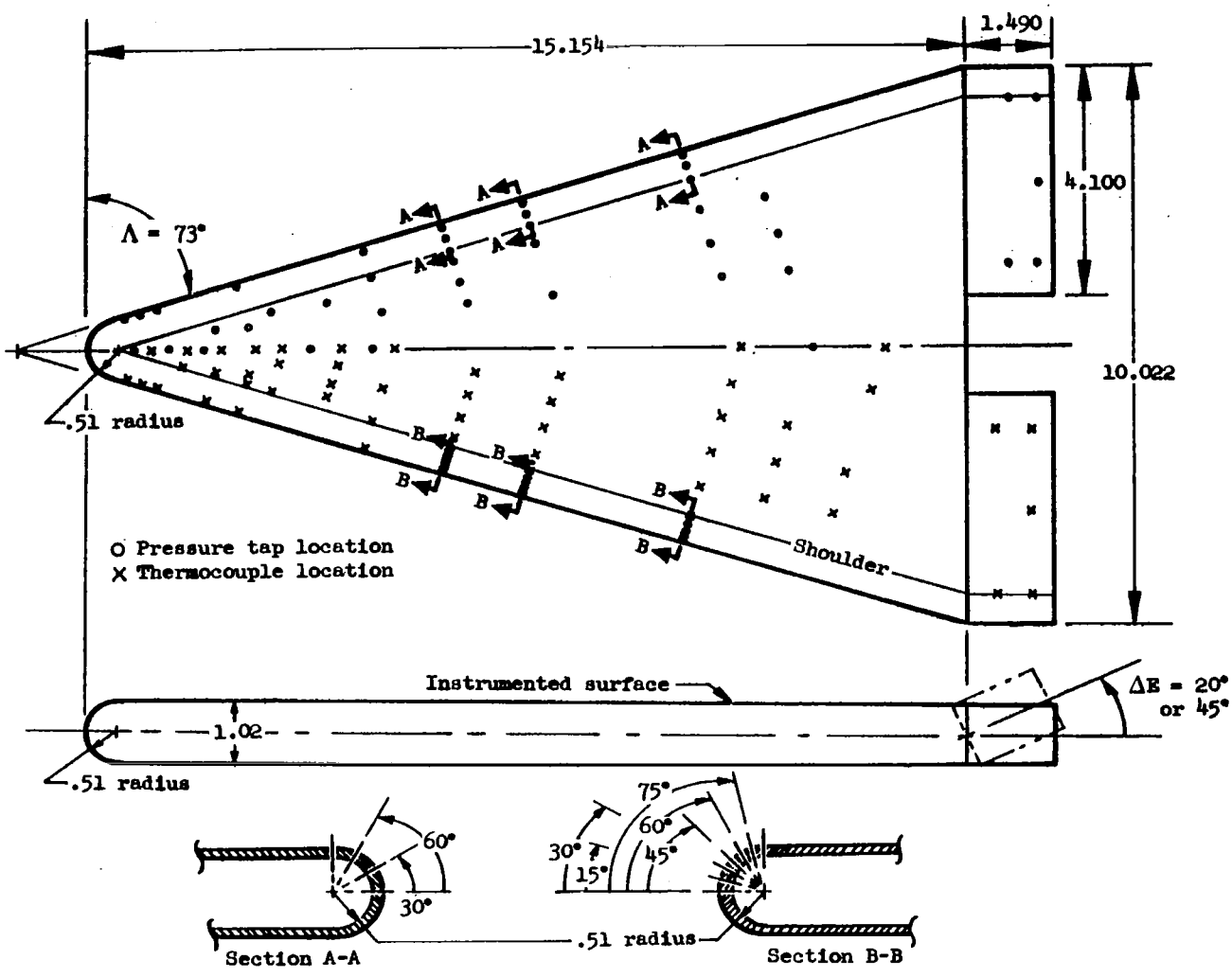

(a) Wing with deflected elevons.
All linear dimensions
are in inches

Figure 1.- Blunt delta wing model, AD462M-1.

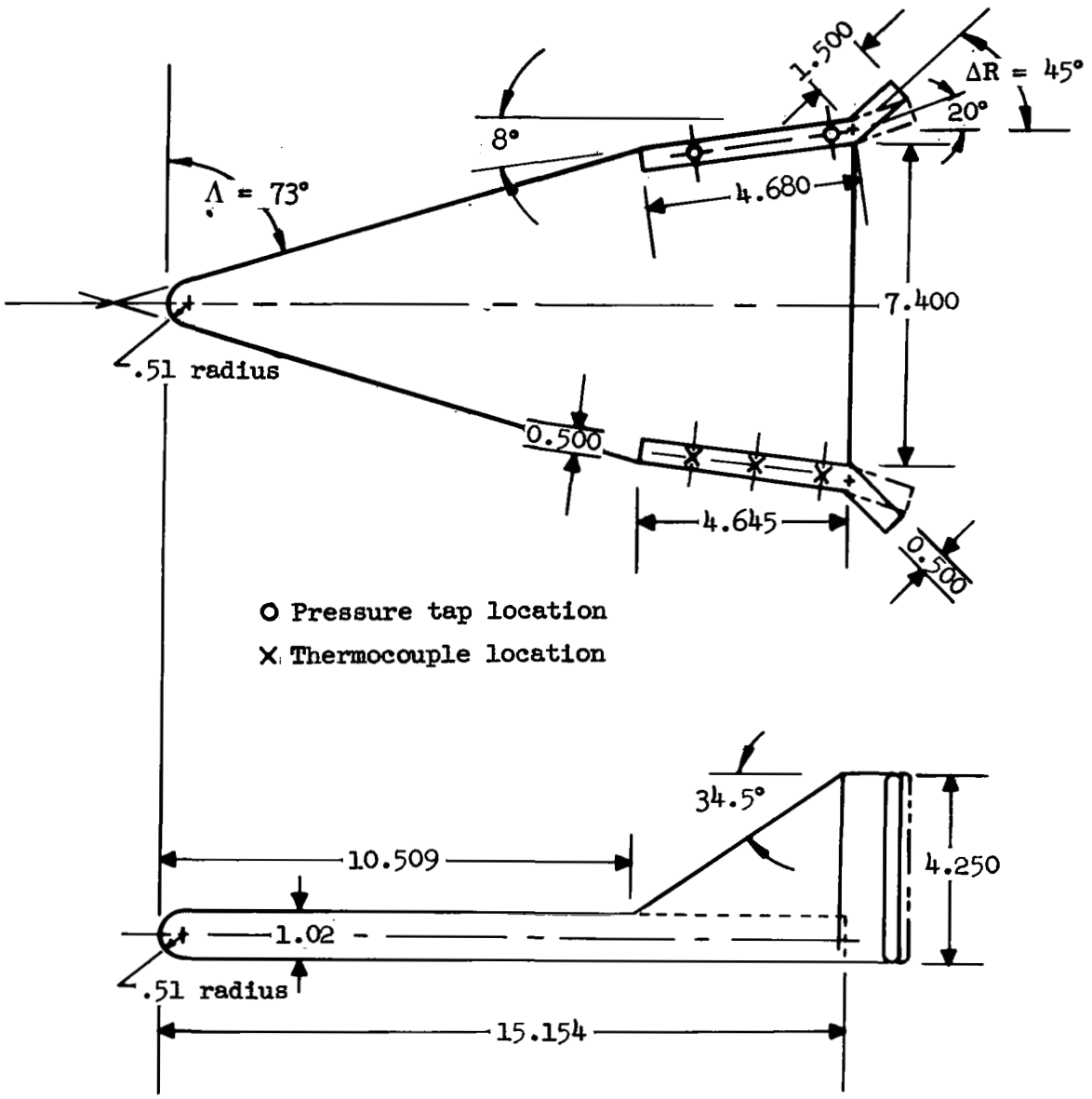

(b) Wing with fins and rudders.
All linear dimensions
are in inches

Figure 1.- Continued.

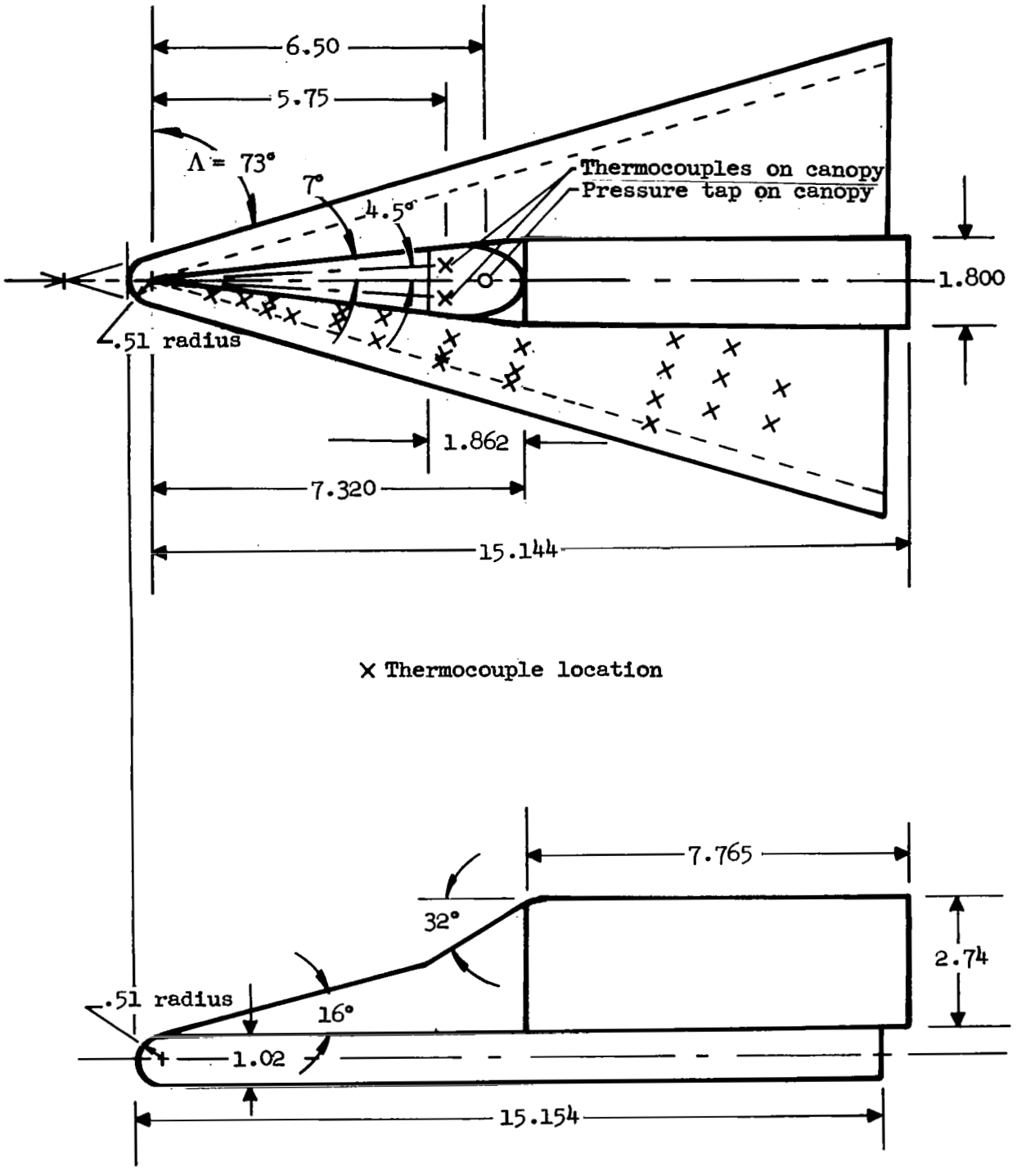

(c) Wing with body and canopy with windshield.
All linear dimensions are in inches

Figure 1.- Concluded.

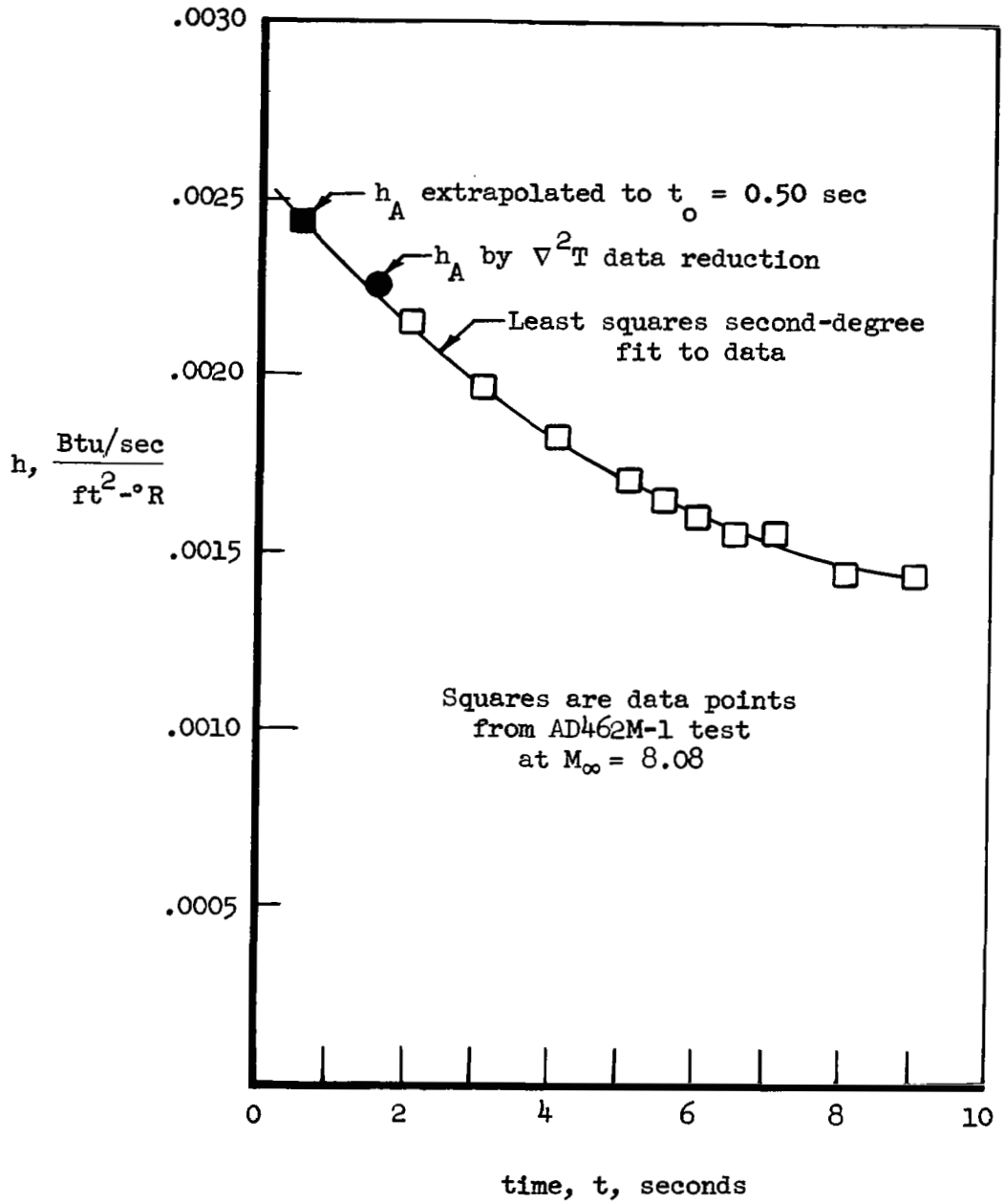

Figure 2.- Heat transfer conduction corrections for thin-skinned calorimeter models.

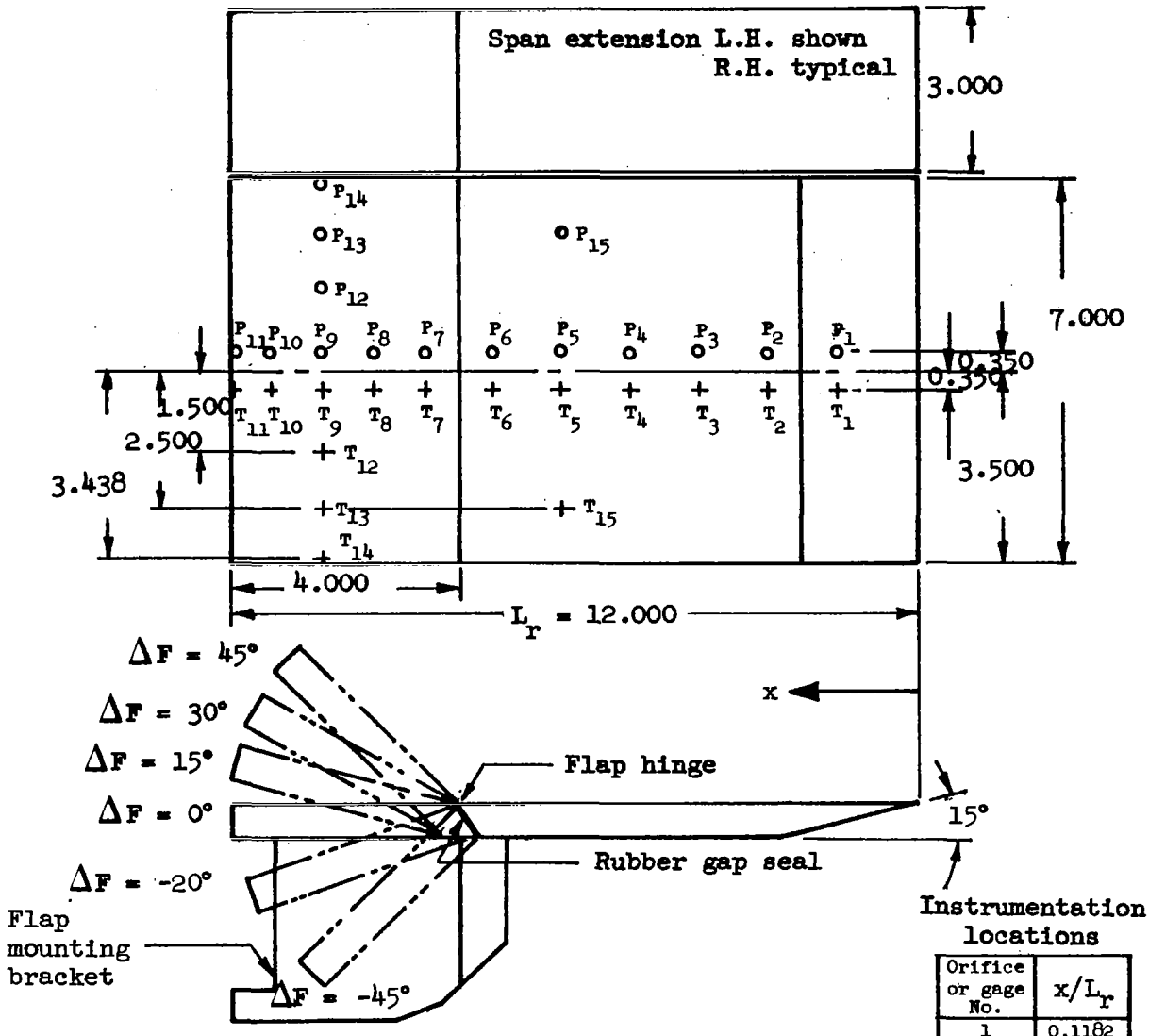

All linear dimensions are in inches

Orifice or gage No.	x/L_r
1	0.1182
2	0.2183
3	0.3180
4	0.4180
5	0.5185
6	0.6185
7	0.7160
8	0.7910
9	0.8660
10	0.9410
11	0.9950
12	0.8660
13	0.8660
14	0.8660
15	0.5185

Figure 3.- Sharp flat plate separation model, AD642M-1

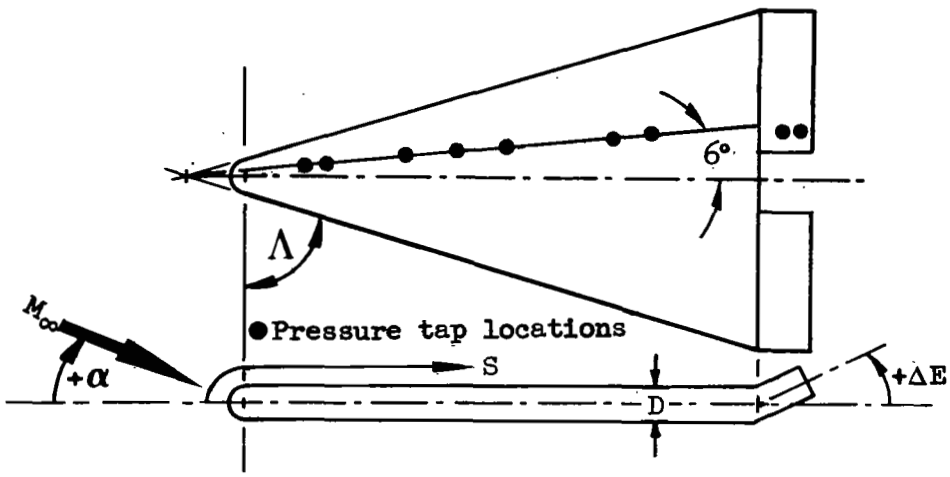

Flagged symbols indicate repeat test data

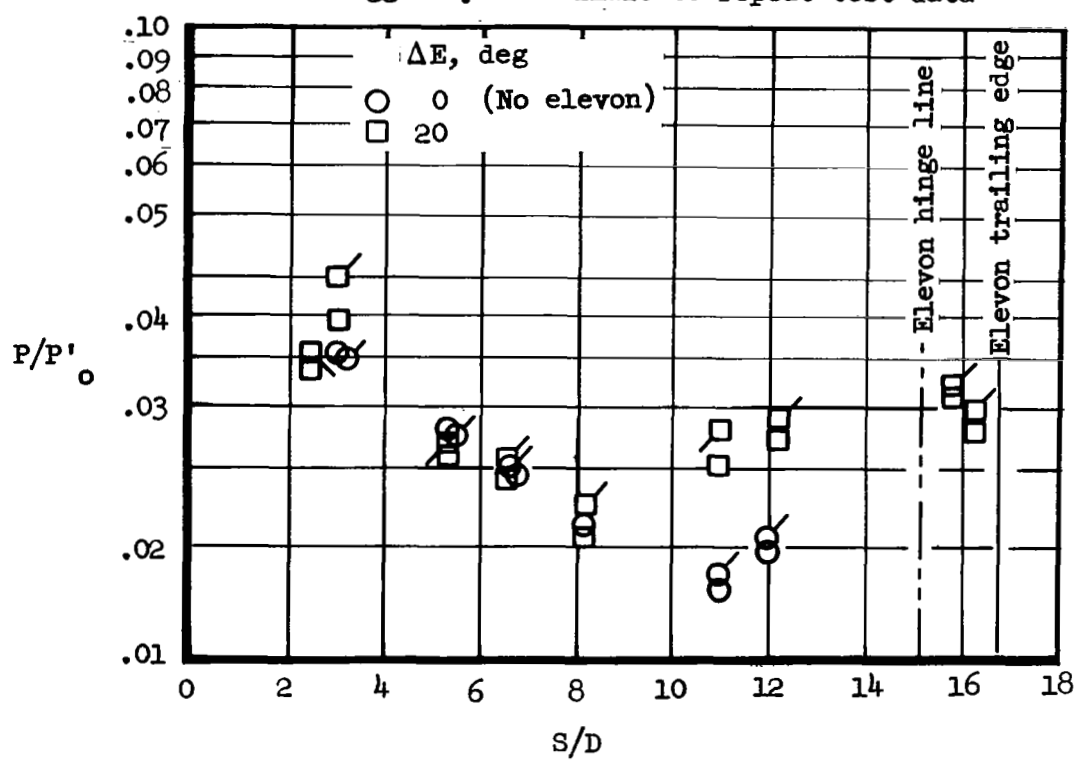

Figure 4.- Pressure data repeatability along a 6° ray line on a blunt delta wing model. AD462M-1; $M_\infty = 8.08$; $\alpha = 0°$; $\Lambda = 73°$; $N_{Re,L_r} = 1.202 \times 10^6$; $P'_o = 1.63$ psia; $H_o = 7.5 \times 10^6$ ft-lb/slug.

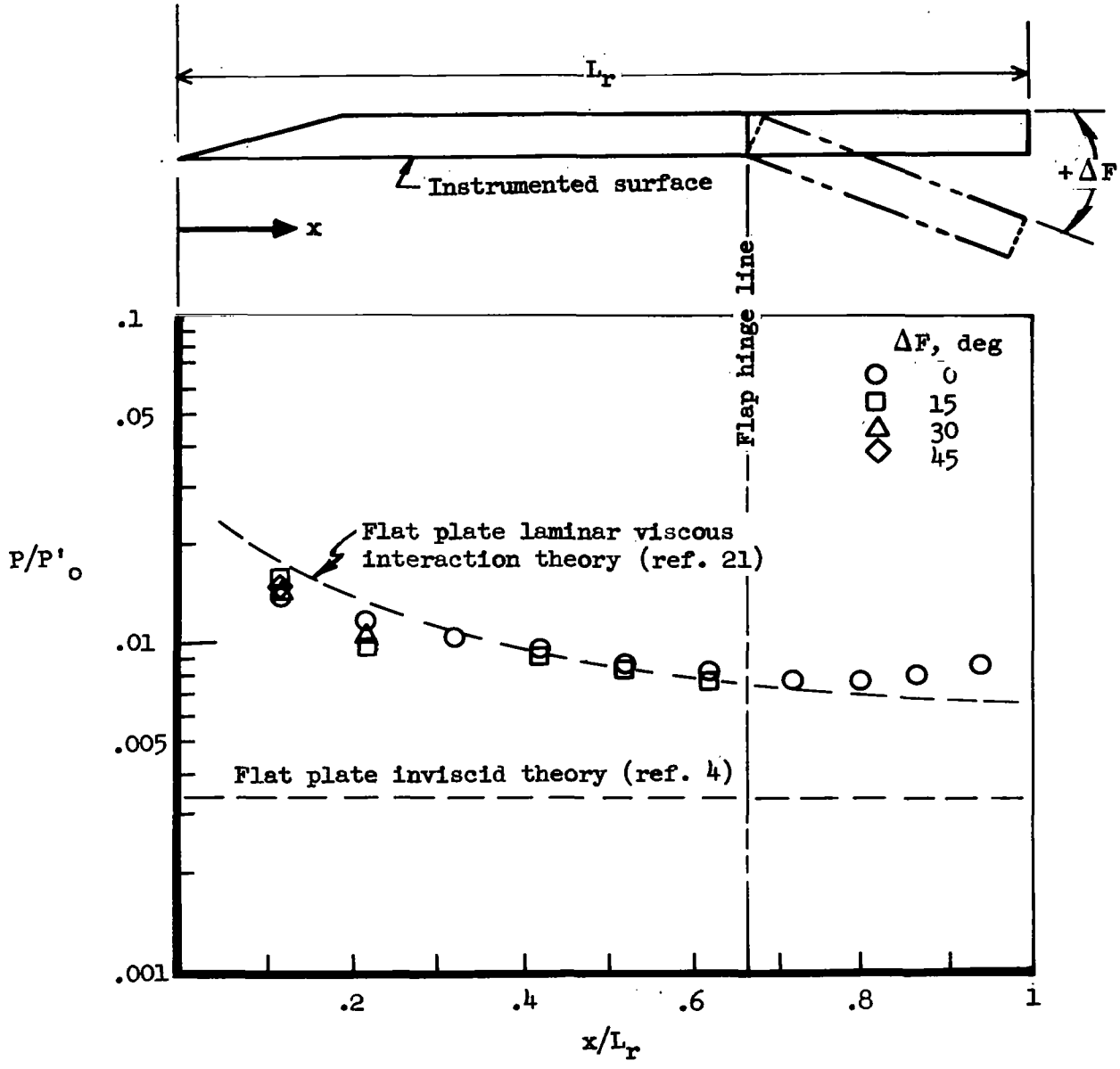

Figure 5.- Pressure data repeatability ahead of separation on a sharp flat plate model. AD642M-1; M_∞ = 15.15; α = 0°; N_{Re,L_r} = .116 x 10^6; P'_o = .442 psia; H_o = 27.1 x 10^6 ft-lb/slug.

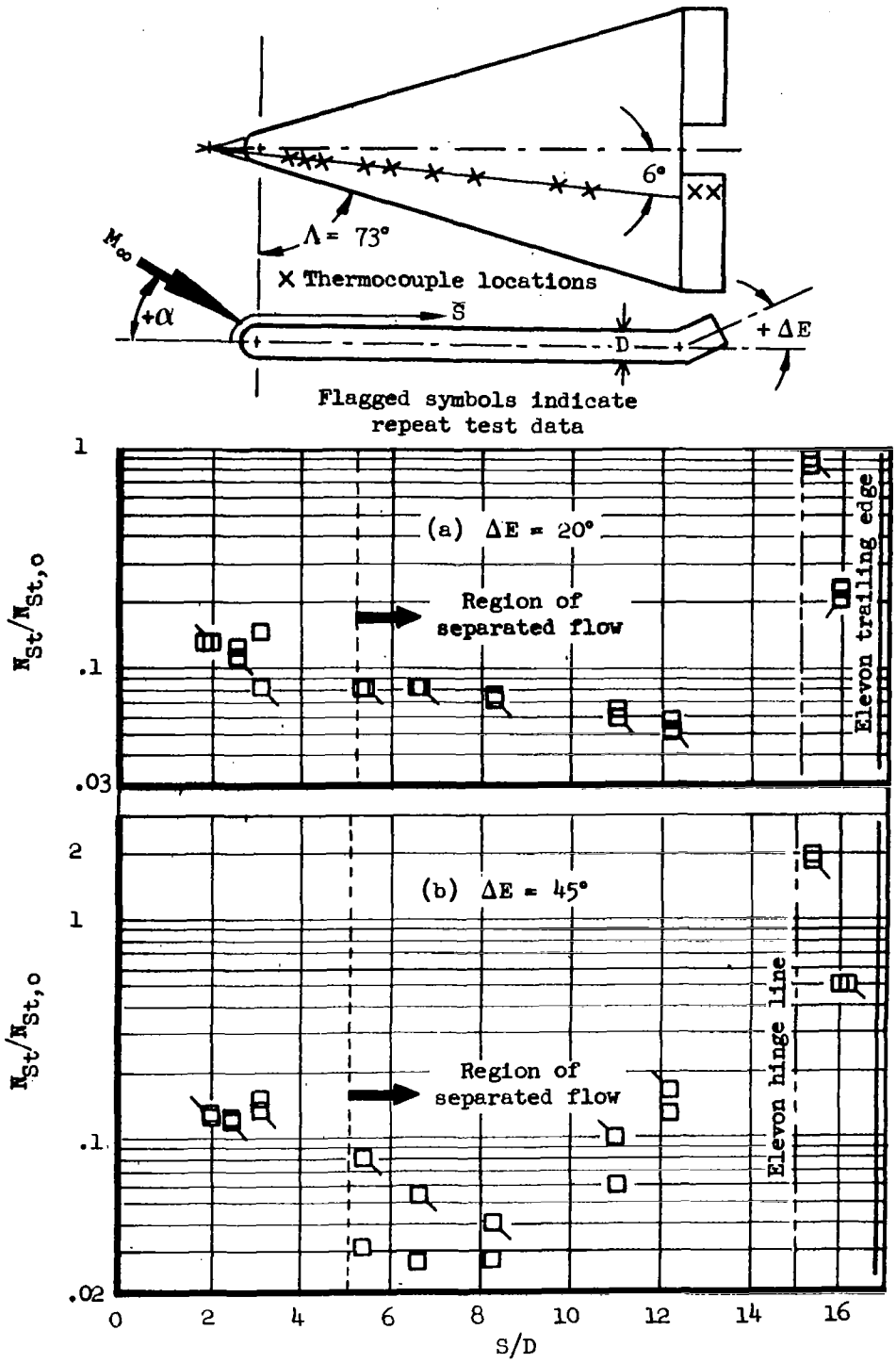

Figure 6.- Repeatability of heat transfer data along a 6° ray line on a blunt delta wing model. AD462M-1; $M_\infty = 8.08$; $\alpha = 15°$; $N_{Re,L_r} = 1.202 \times 10^6$; $P'_o = 1.63$ psia; $H_o = 7.5 \times 10^6$ ft-lb/slug; $N_{St,o} = .0277$.

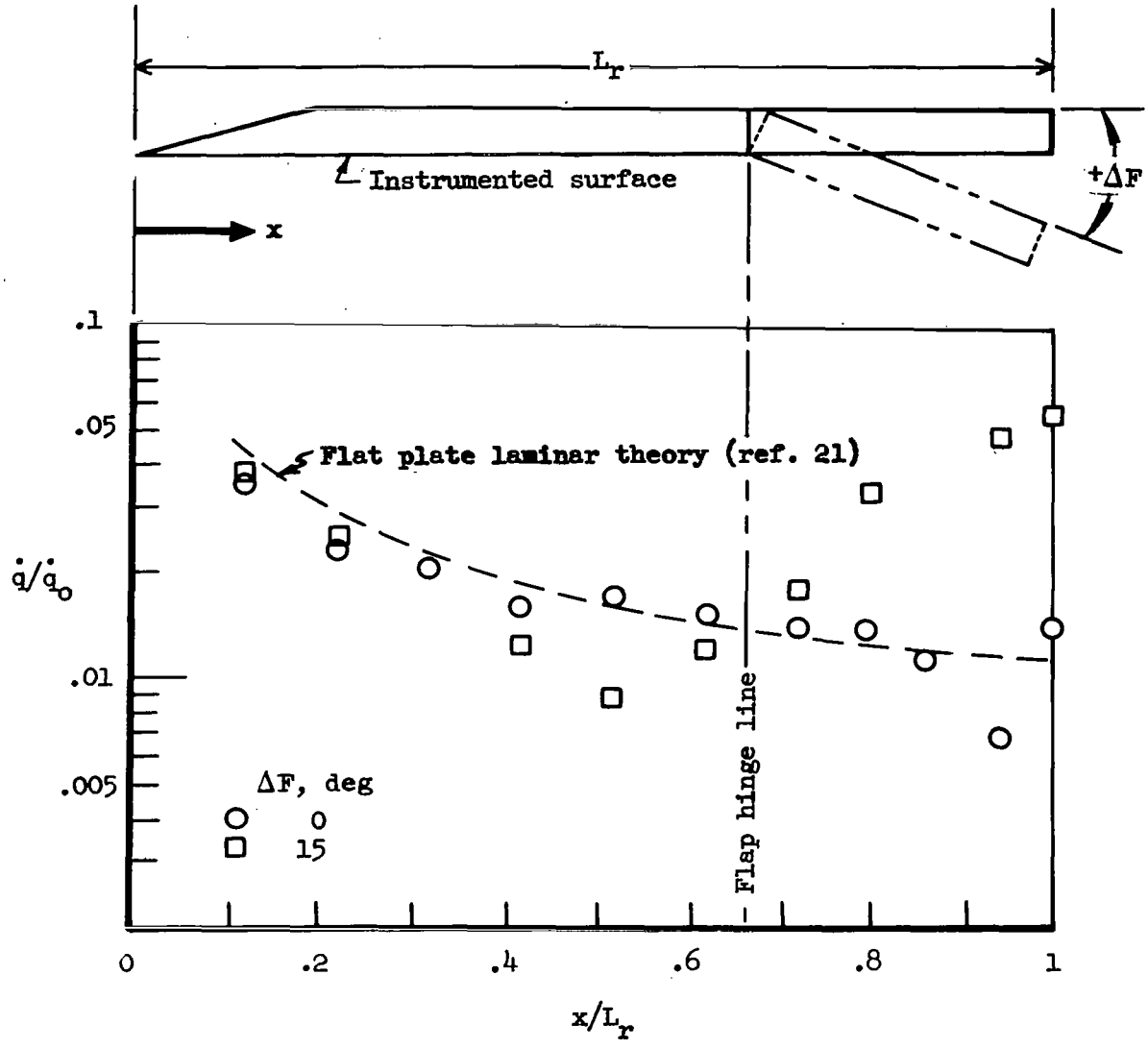

Figure 7.- Repeatability of heat transfer data without separation on a sharp flat plate model. AD642M-1; M_∞ = 15.15; α = 0°; N_{Re,L_r} = .116 x 10^6; P'_o = .442 psia; H_o = 27.1 x 10^6 ft-lb/slug; $\dot{q}_o$ = 33 Btu/ft^2-sec.

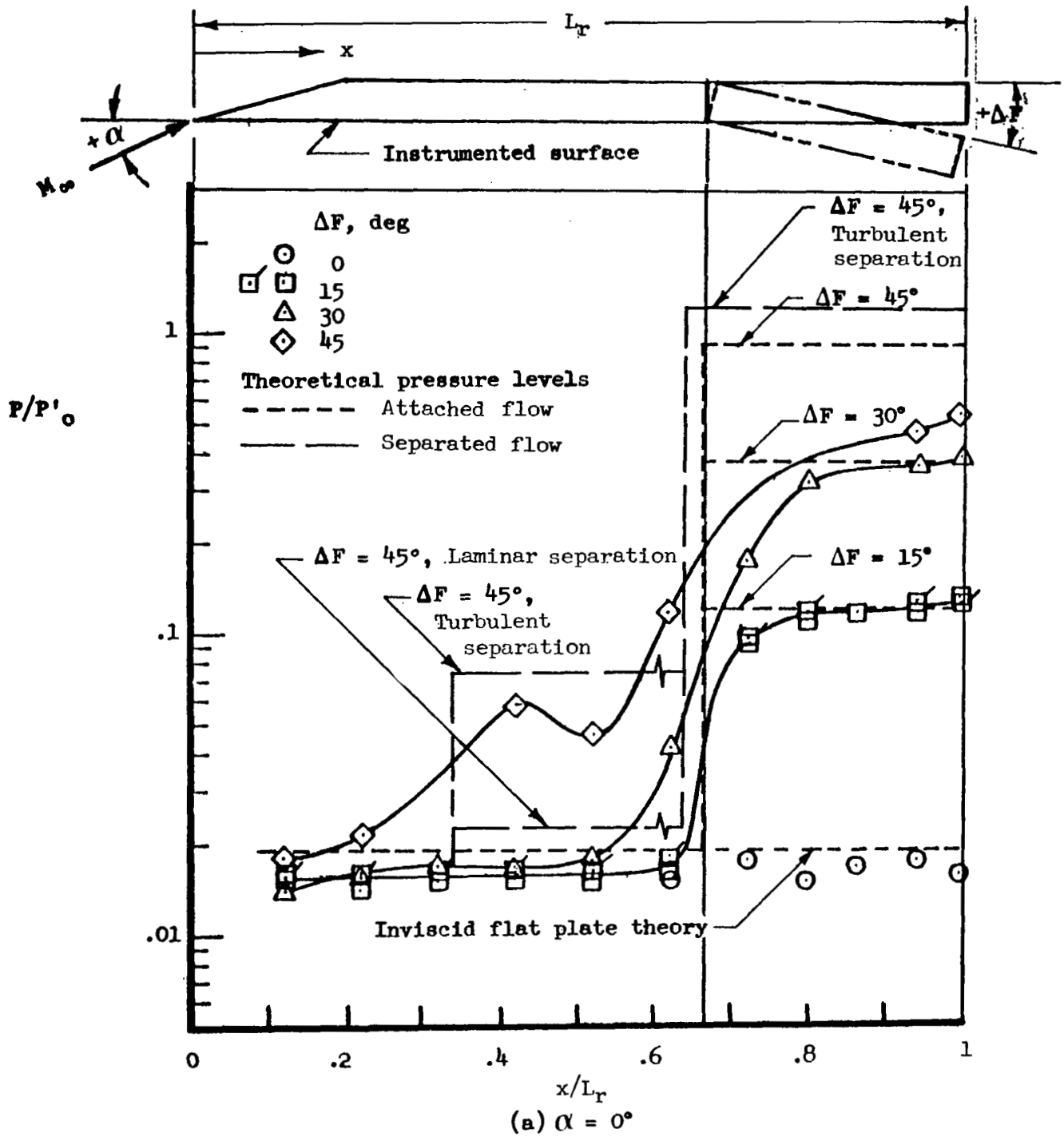

(a) $\alpha = 0°$

Figure 8.- Pressure distribution on sharp flat plate with deflected flap. $M_\infty = 6.38$; $P'_o = 89.3$ psia; $H_o = 13.5 \times 10^6$ ft-lb/slug; $N_{Re,L_r} = 14.08 \times 10^6$.

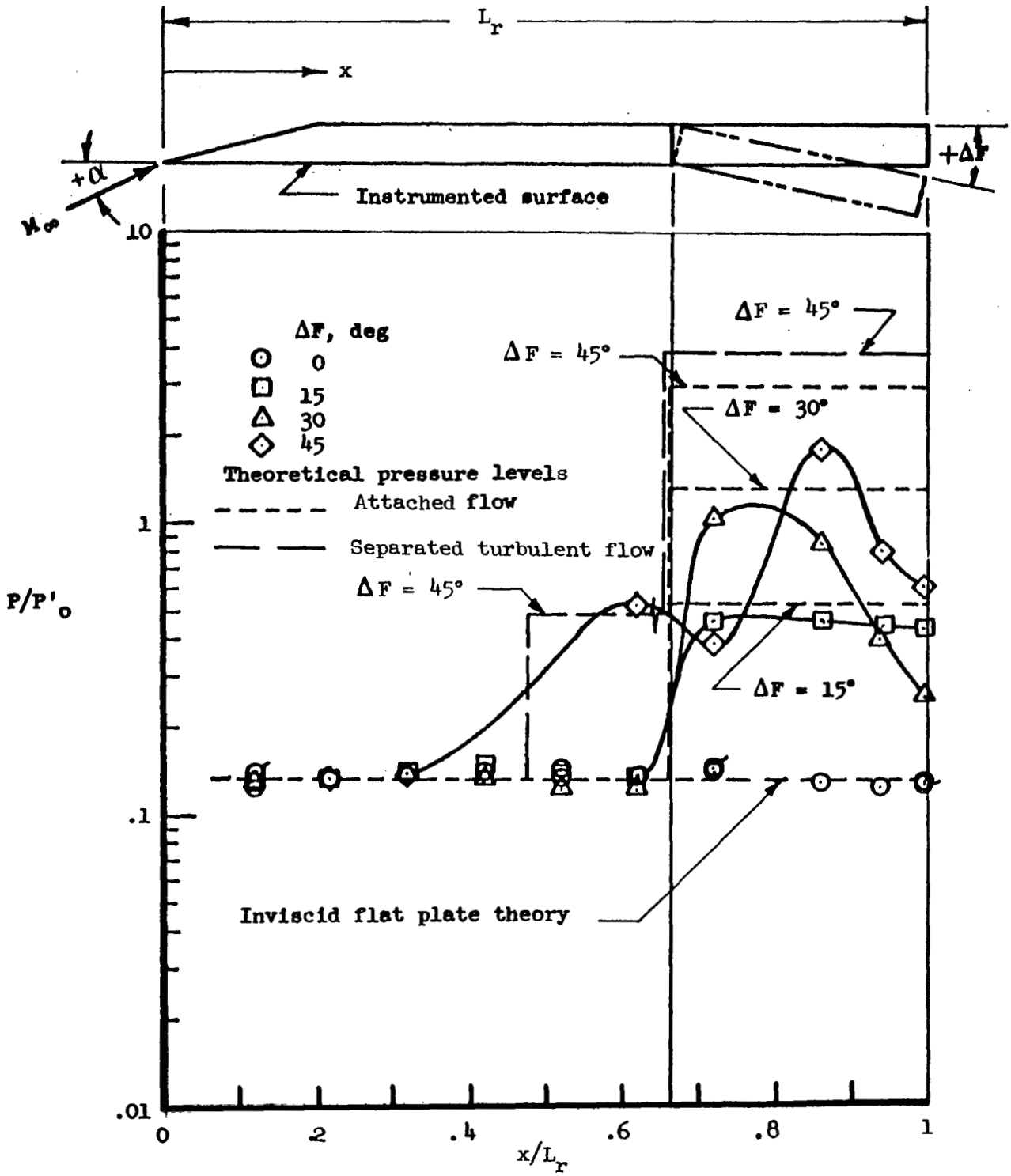

(b) $\alpha = 15°$

Figure 8.- Concluded.

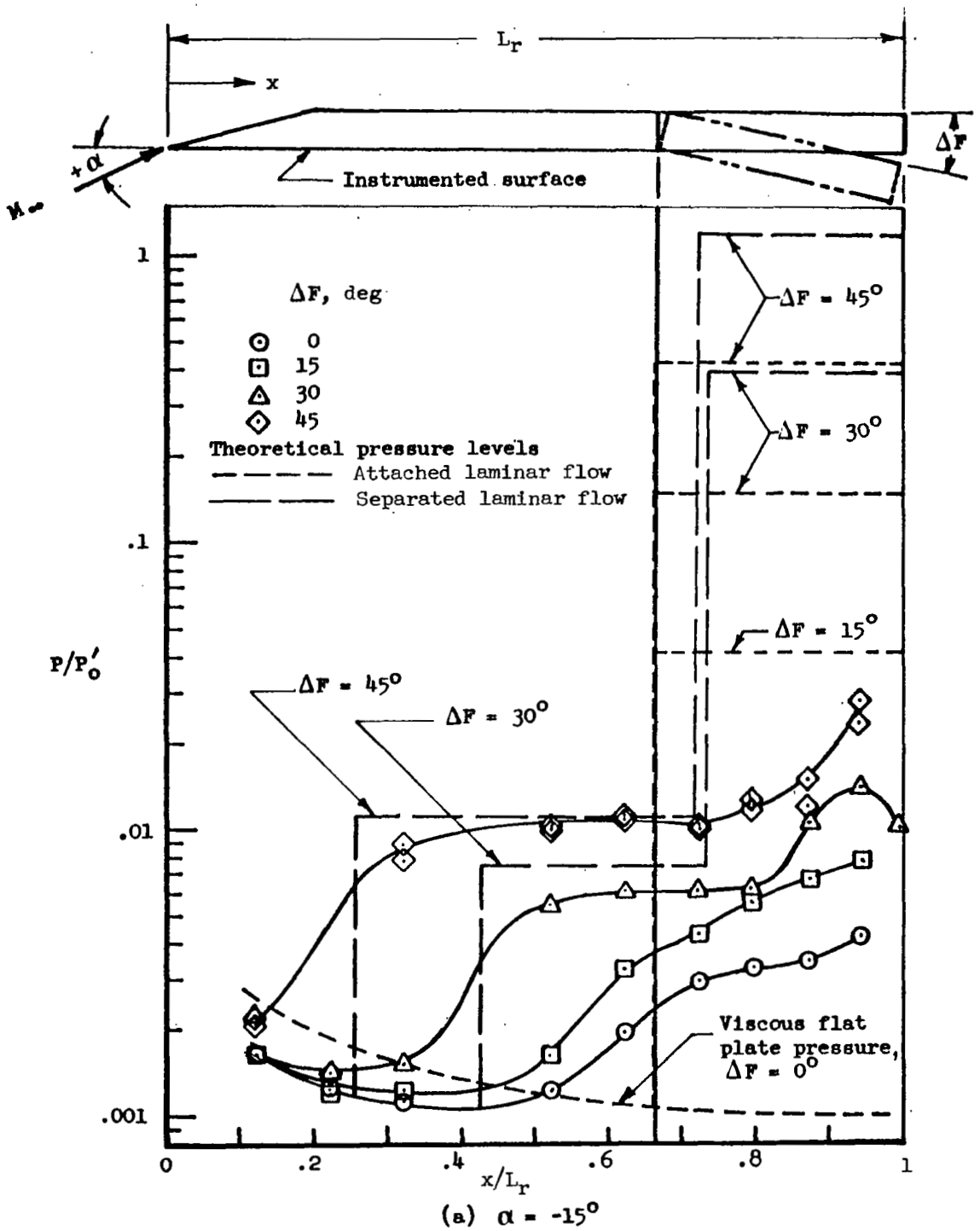

(a) $\alpha = -15°$

Figure 9. - Pressure distribution on sharp flat plate with deflected flap. $M_\infty = 15.15$; $P'_o = .424$ psia; $H_o = 27.2 \times 10^6$ ft-lb/slug; $N_{Re,L_r} = .112 \times 10^6$.

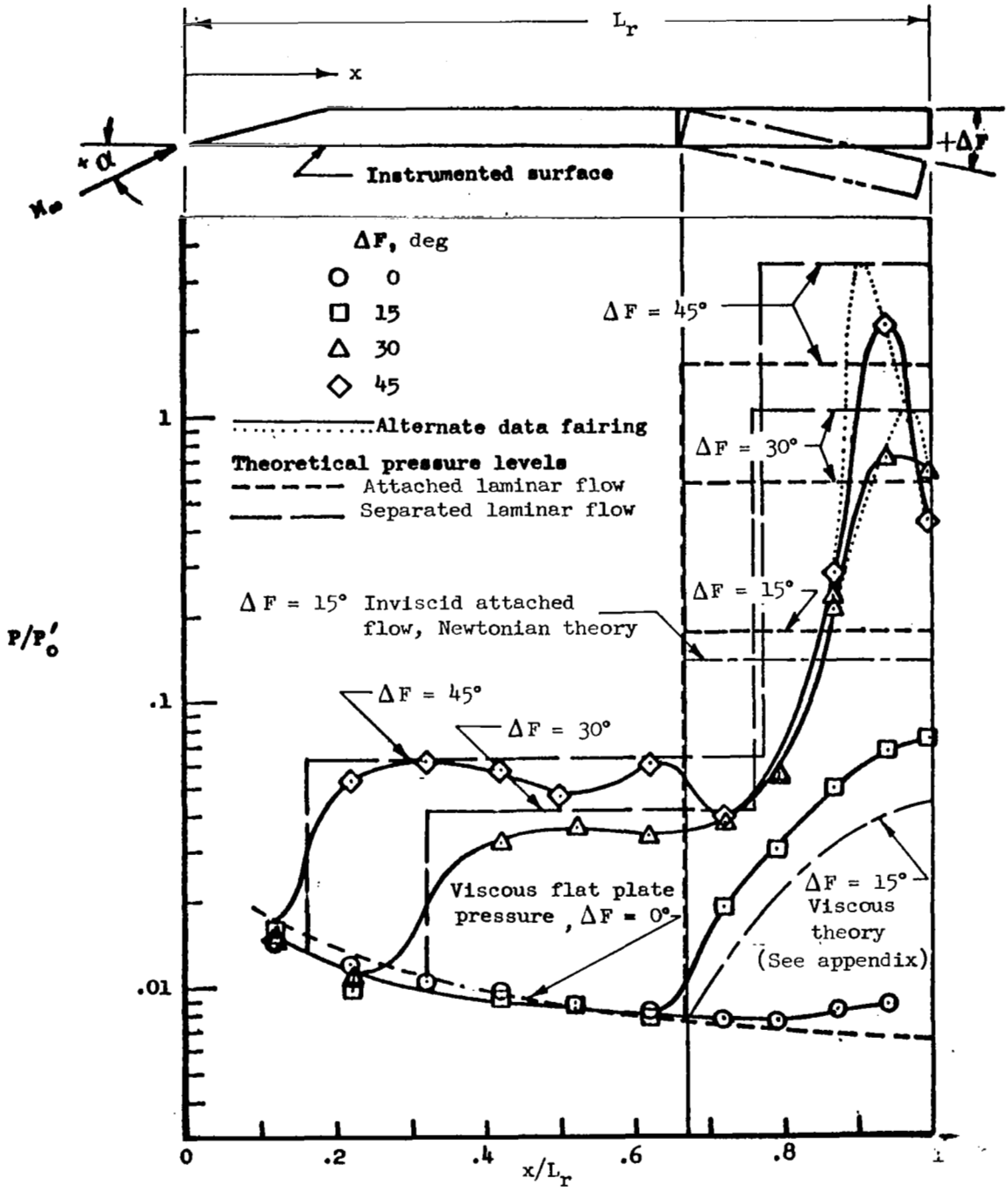

(b) $\alpha = 0°$

Figure 9. - Continued.

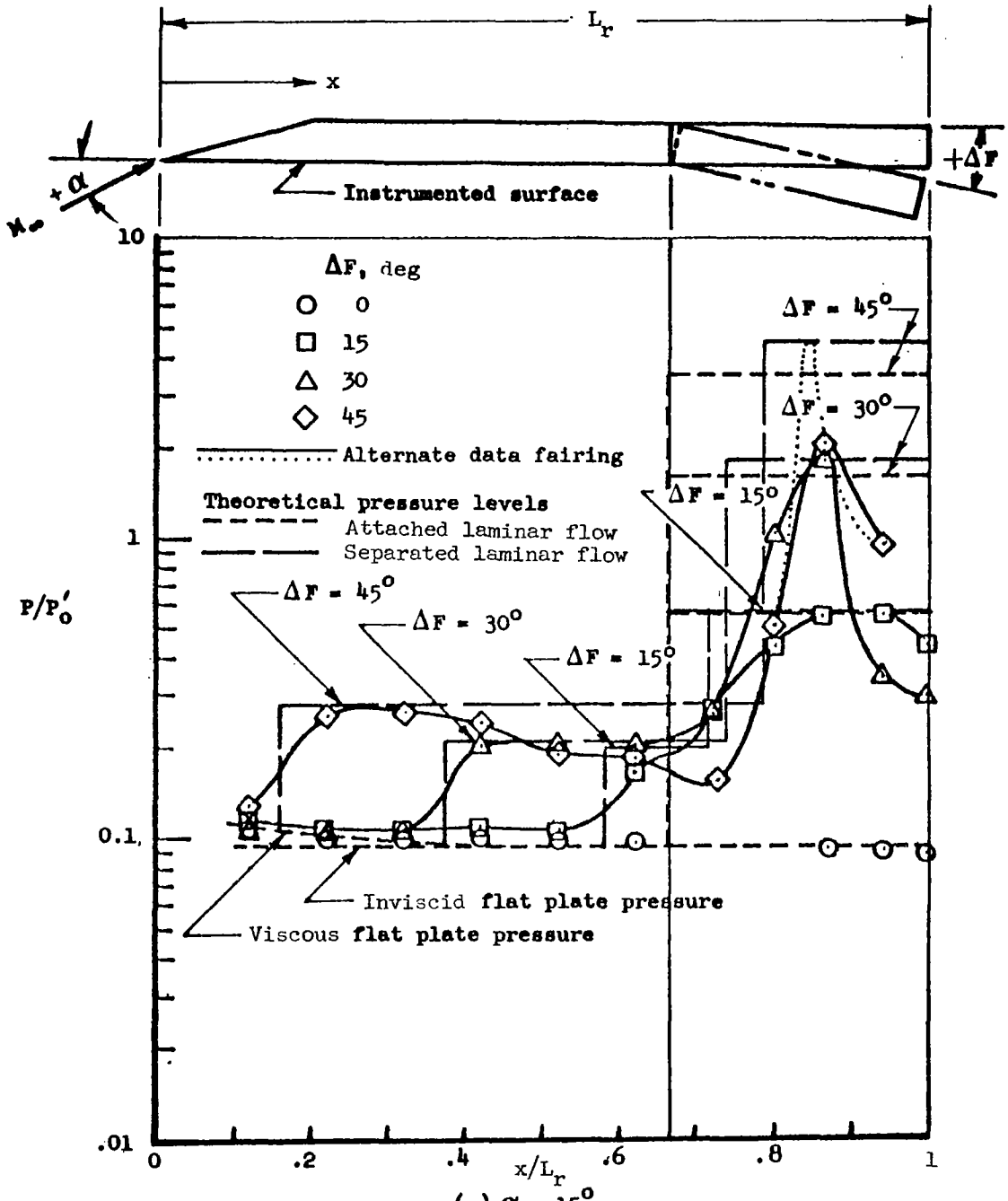

(c) $\alpha = 15^\circ$

Figure 9. - Concluded.

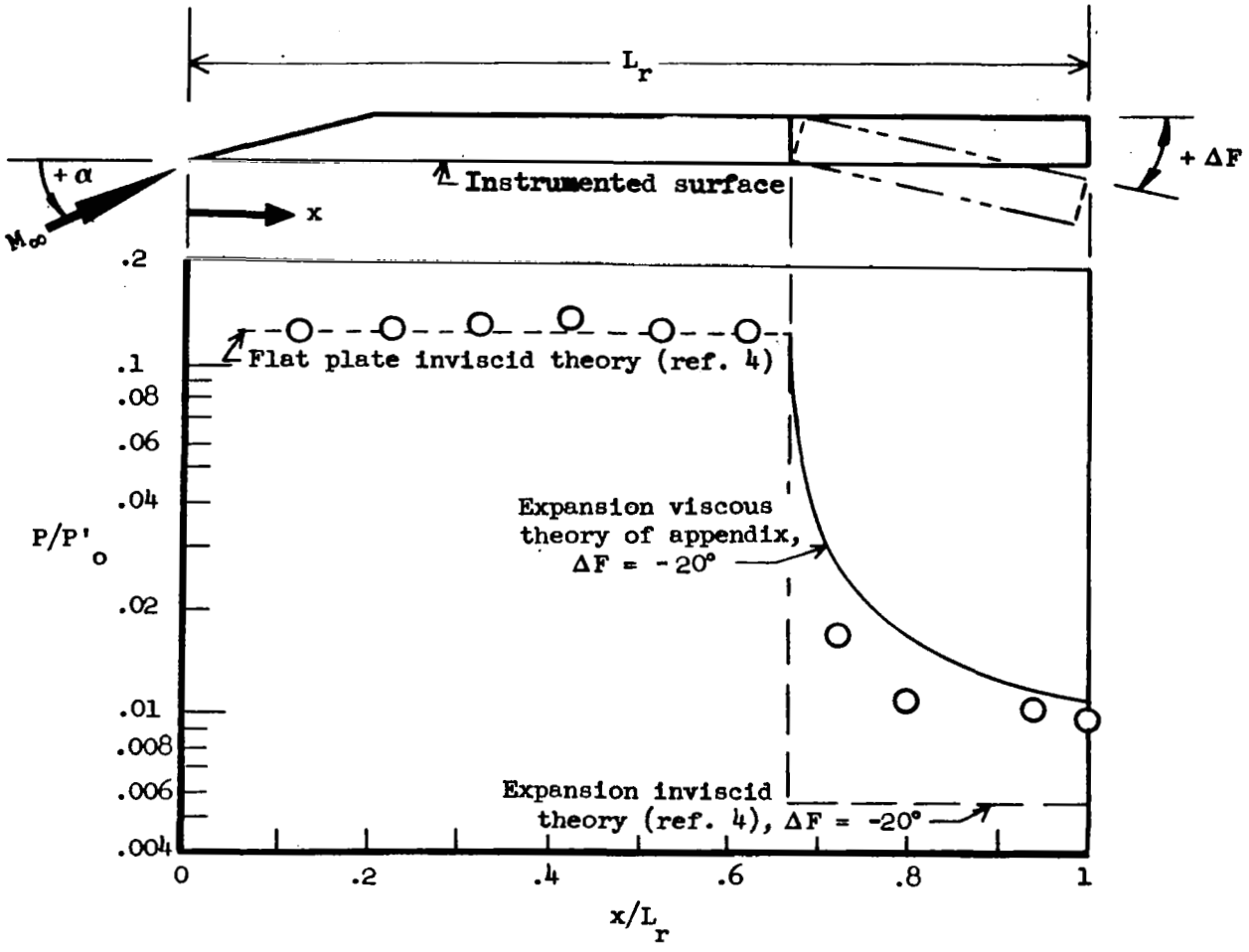

(a) $M_\infty = 6.38$; $N_{Re,L_r} = 14.09 \times 10^6$; turbulent boundary layer; $P'_o = 89.28$ psia; $H_o = 13.3 \times 10^6$ ft-lb/slug

Figure 10.- Pressure distribution on a sharp flat plate with expanding flow over a deflected flap. $\alpha = 15°$.

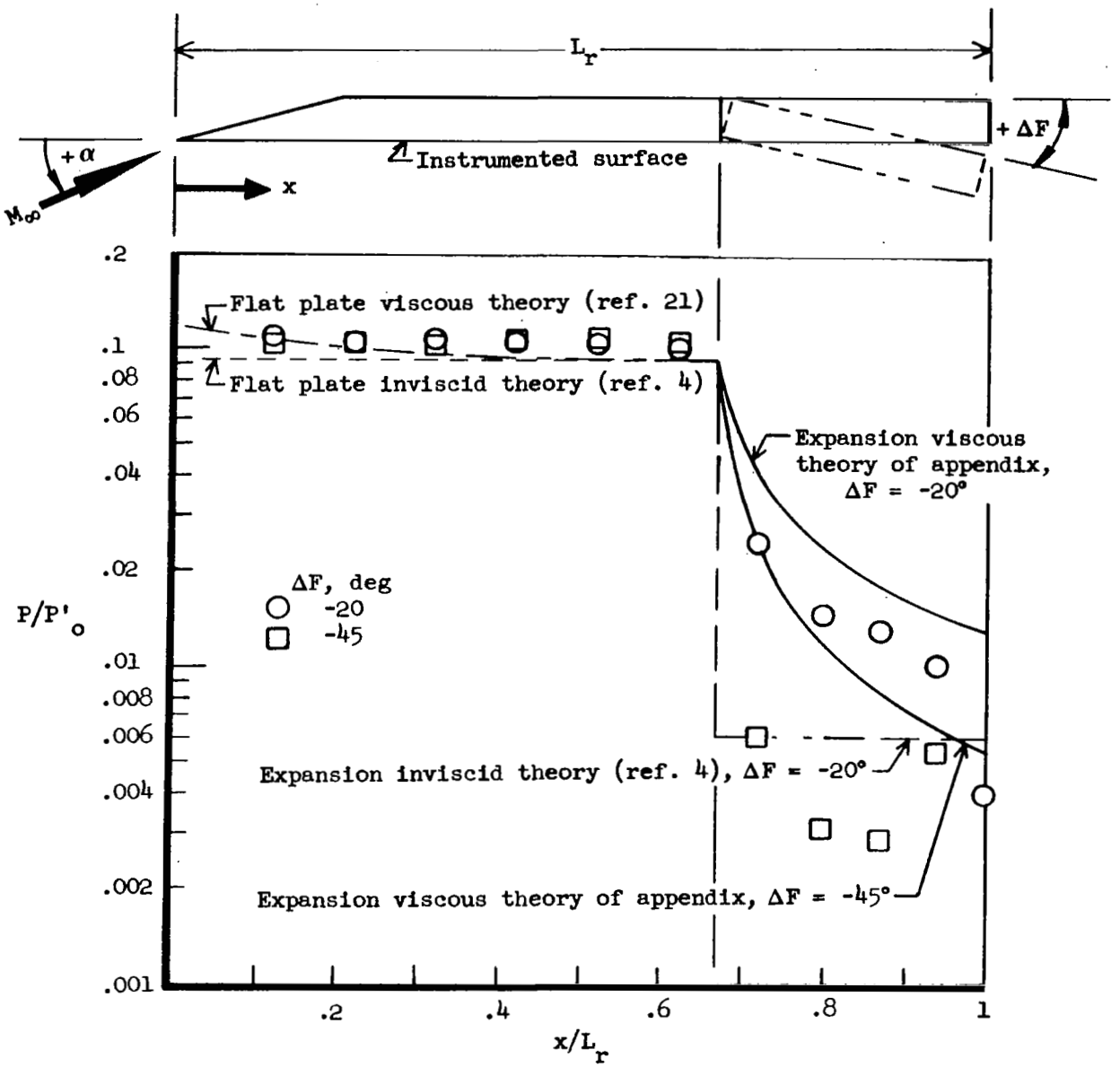

(b) $M_\infty = 15.15$; $N_{Re,L_r} = .109 \times 10^6$; laminar boundary layer; $P'_o = .423$ psia; $H_o = 27.4 \times 10^6$ ft-lb/slug

Figure 10.- Concluded.

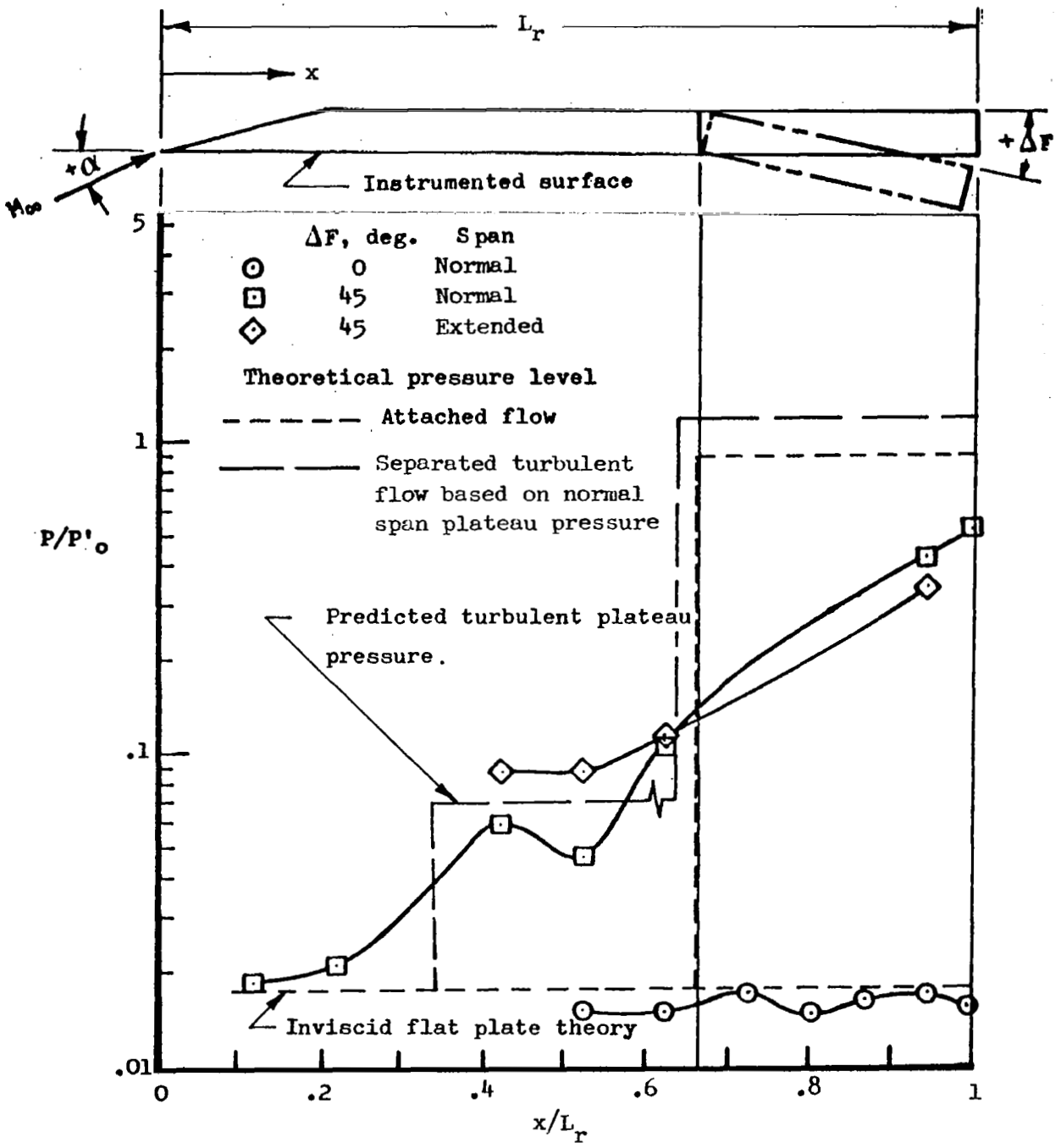

(a) $M_\infty = 6.38$; $\alpha = 0°$; $P'_o = 88.84$ psia; $H_o = 13.67 \times 10^6$ ft-lb/slug; $N_{Re,L_r} = 13.69 \times 10^6$

Figure 11.- Effect of span on the pressure distribution on a sharp flat plate with deflected flap.

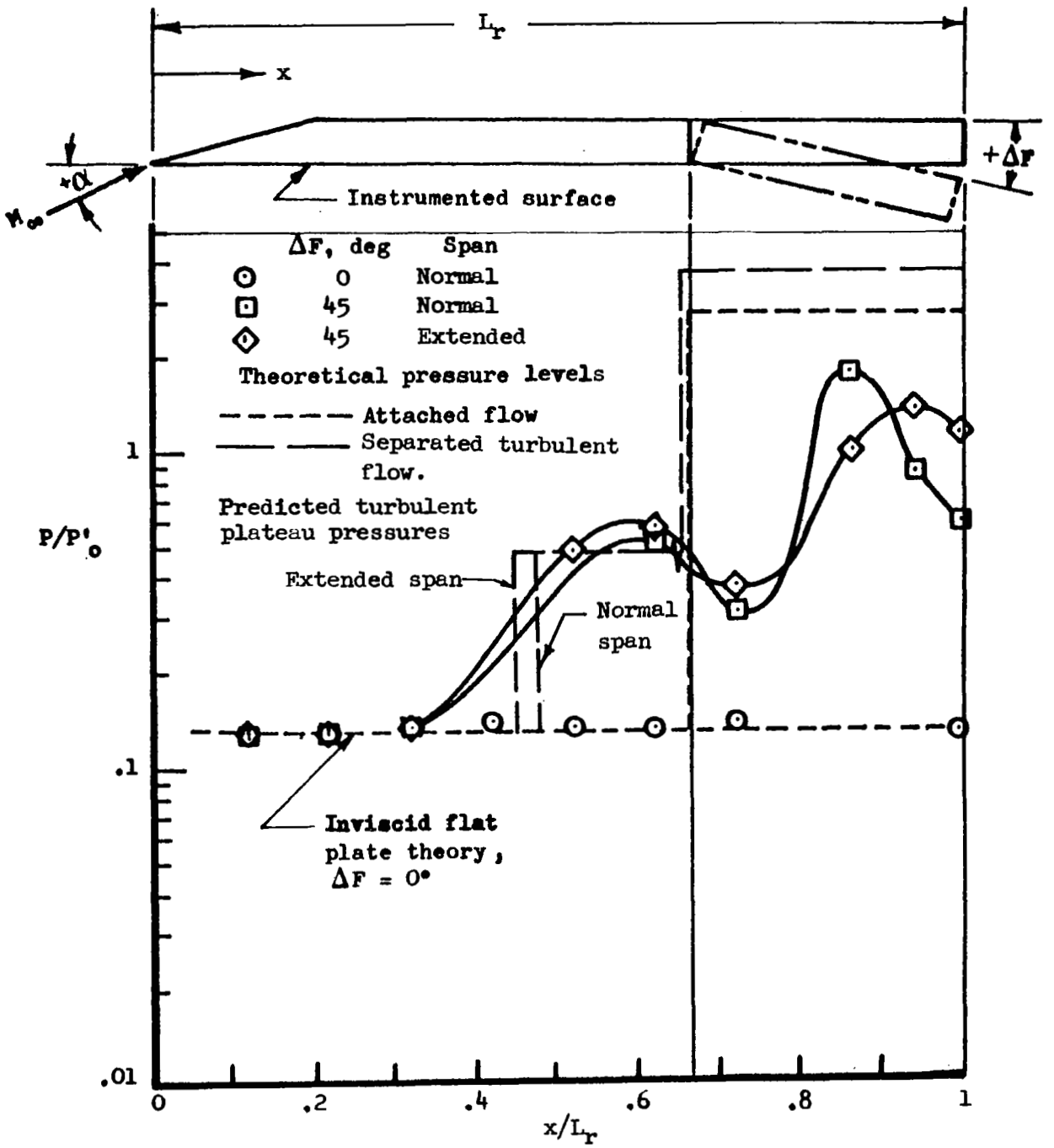

(b) $M_\infty = 6.38$; $\alpha = 15°$; $P'_o = 88.58$ psia; $H_o = 13.47 \times 10^6$ ft-lb/slug; $N_{Re,L_r} = 13.97 \times 10^6$

Figure 11.- Continued.

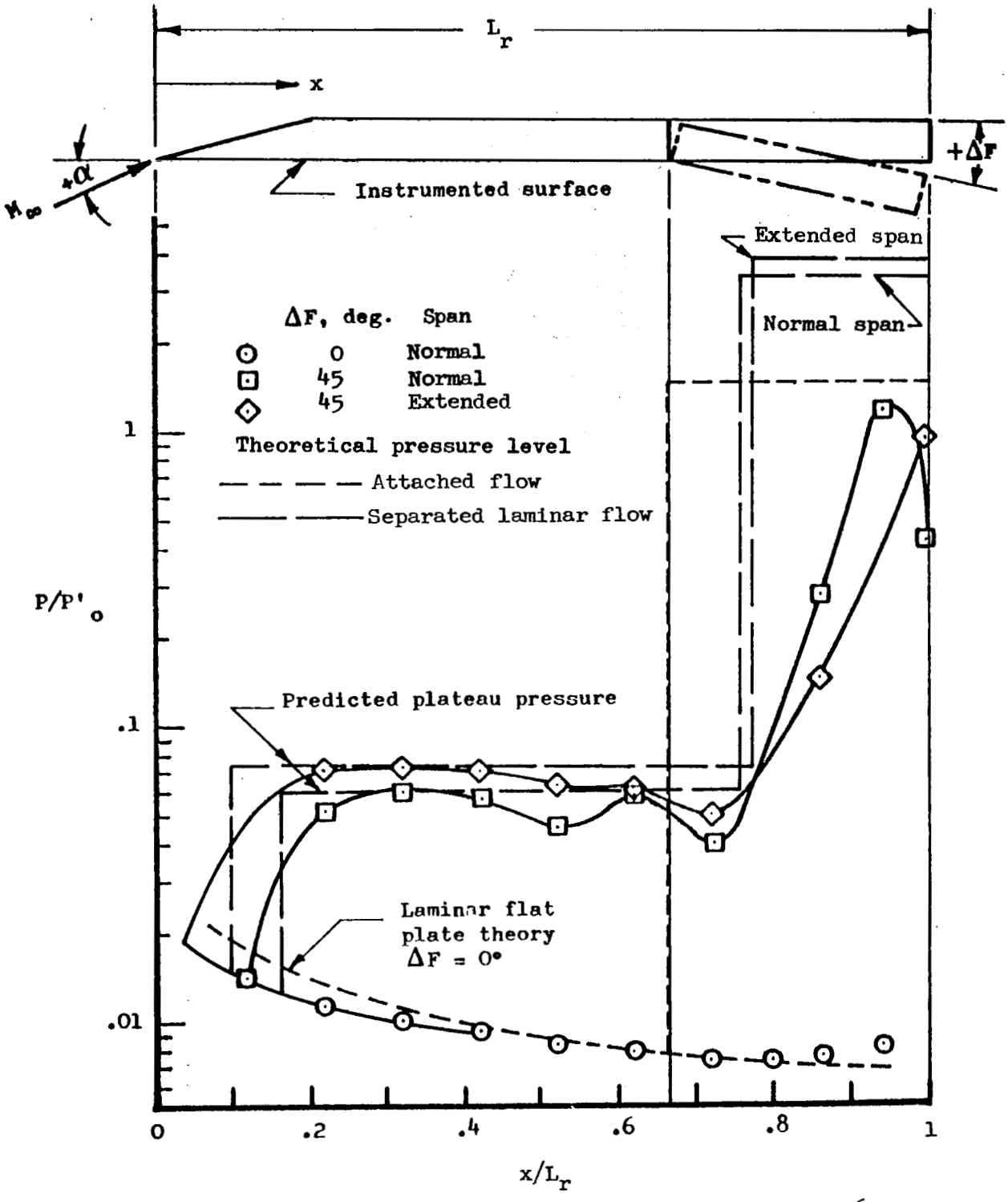

(c) $M_\infty = 15.15$; $\alpha = 0°$; $P'_o = .434$ psia; $H_o = 26.6 \times 10^6$ ft-lb/slug; $N_{Re,L_r} = .117 \times 10^6$

Figure 11.- continued.

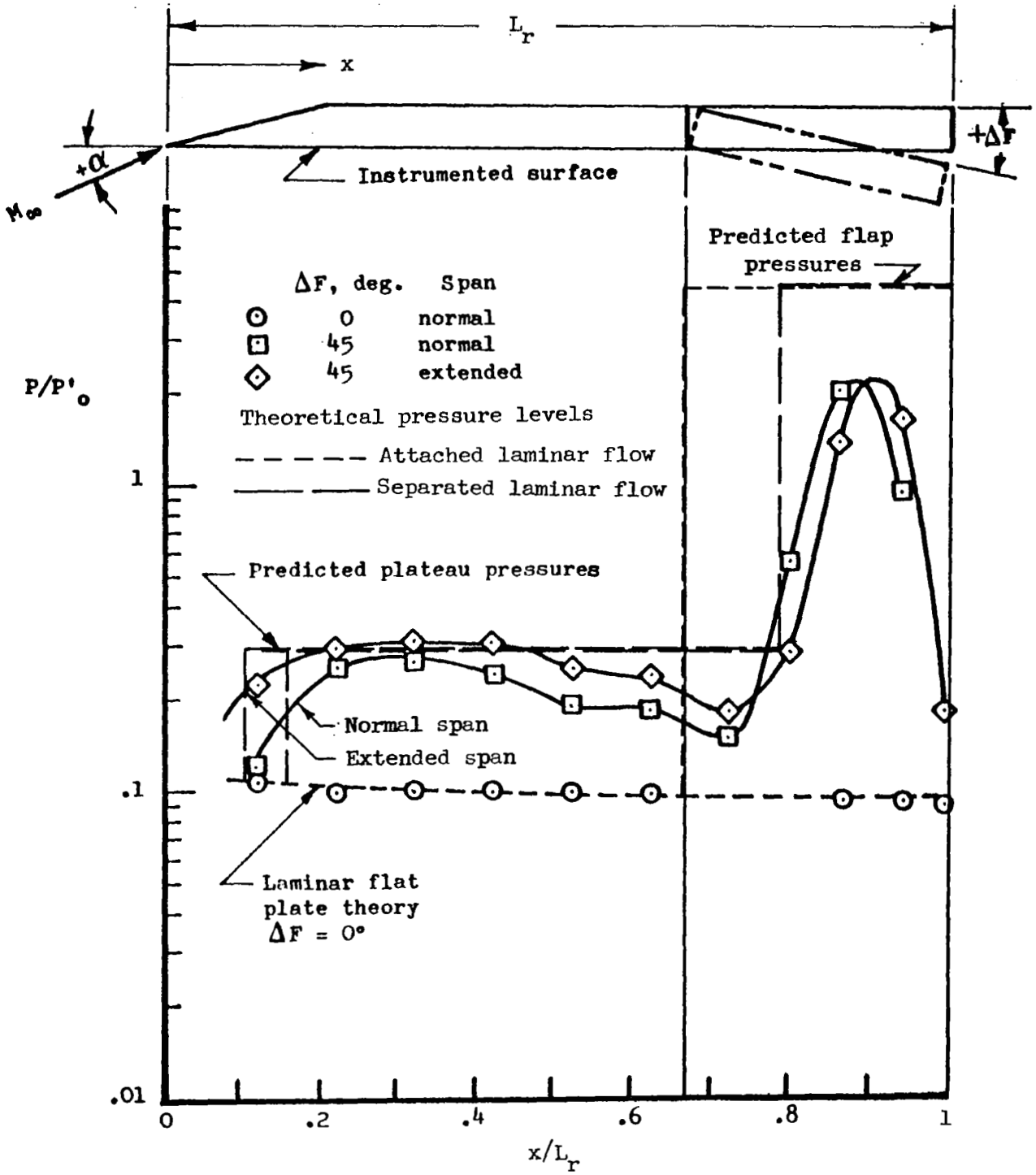

(d) M_∞ = 15.15; α = 15°; P'_o = .421 psia; H_o = 27.1 x 10^6 ft-lb/slug; N_{Re,L_r} = .112 x 10^6.

Figure 11.- Concluded.

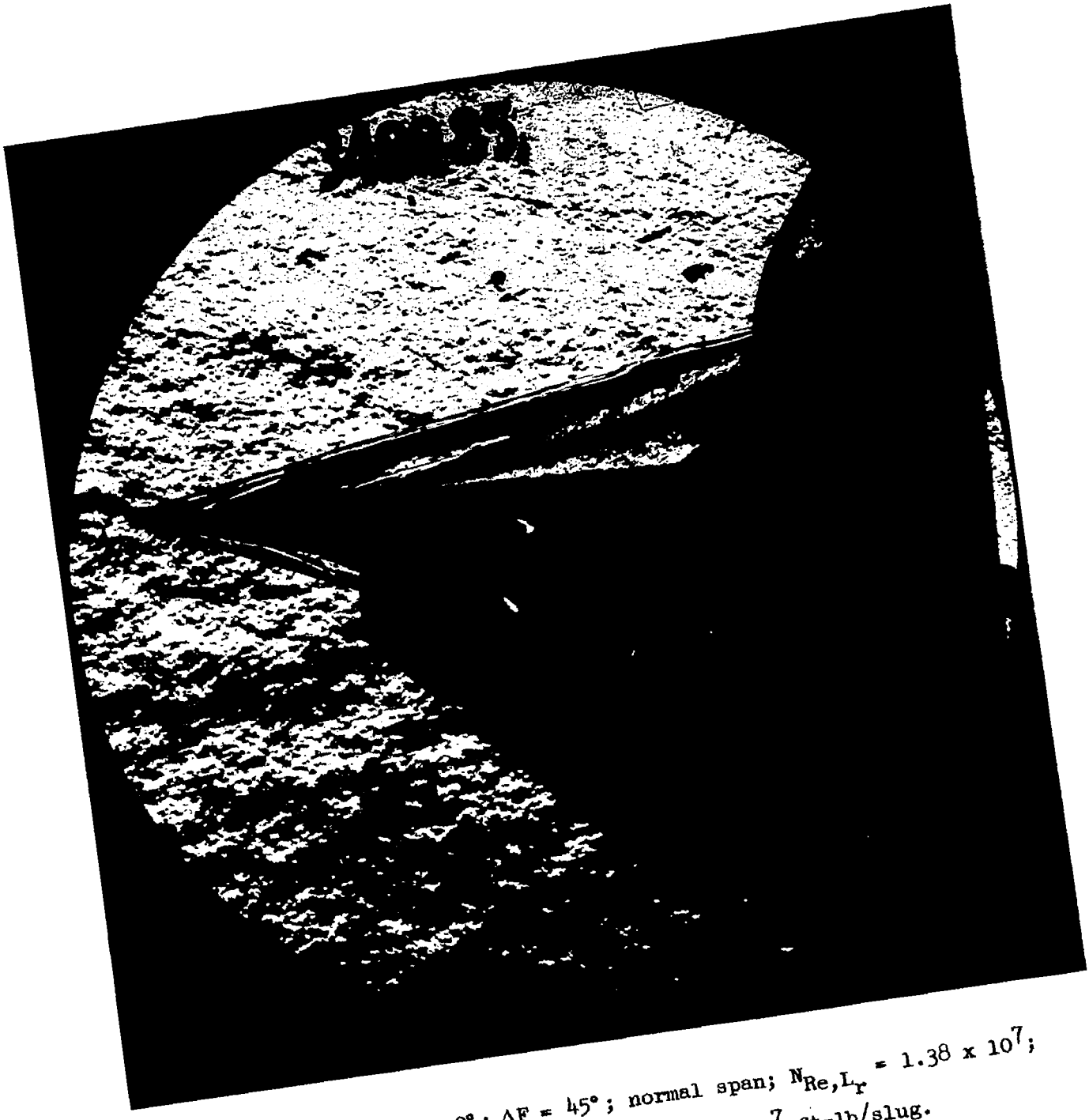

(a) $M_\infty = 6.37$; $\alpha = 0°$; $\Delta F = 45°$; normal span; $N_{Re,L_r} = 1.38 \times 10^7$; $P'_o = 39.58$ psia; $H_o = 1.37 \times 10^7$ ft-lb/slug.

Figure 12.- Schlieren photographs of separation on a flat plate model.

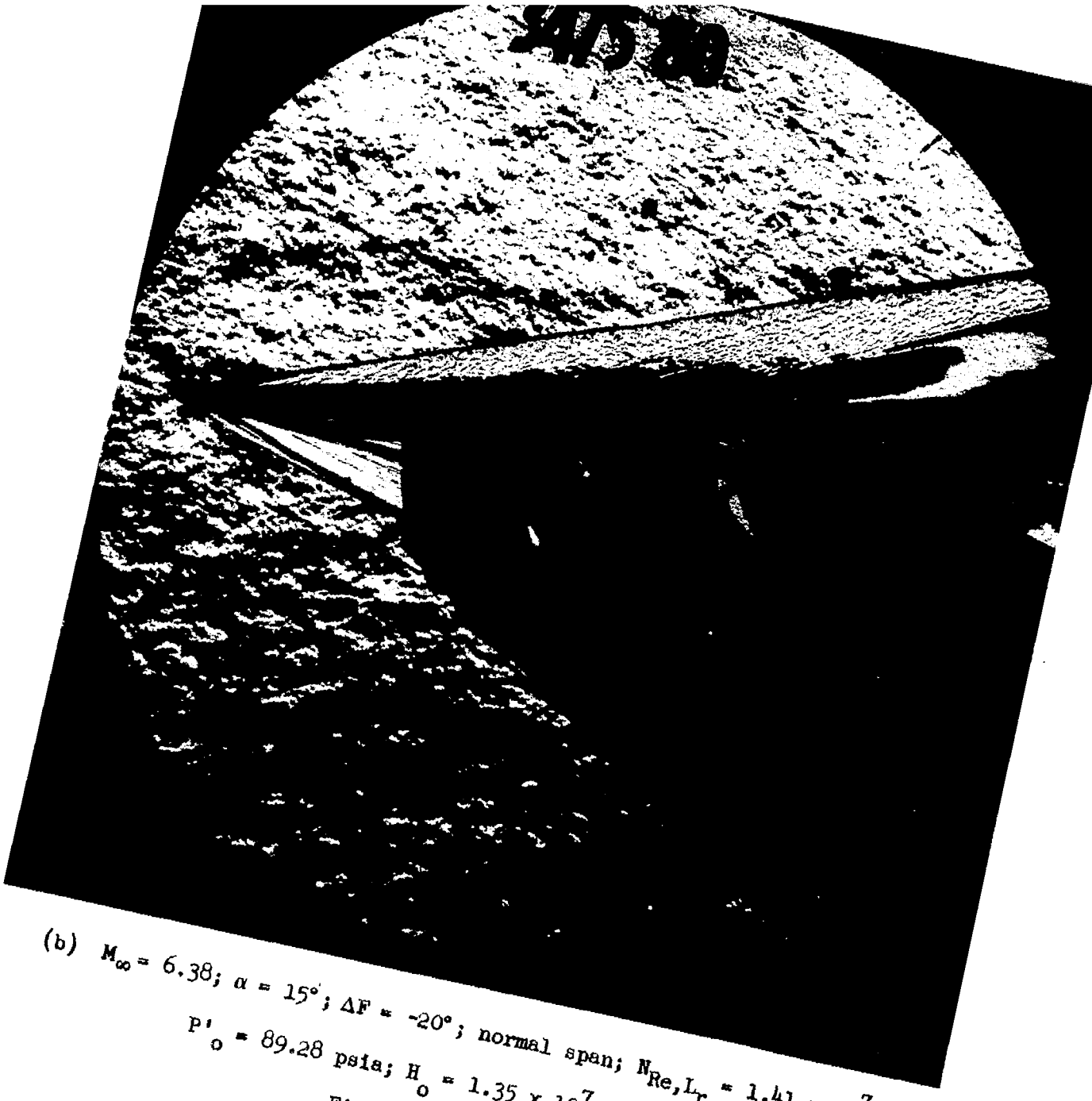

(b) $M_\infty = 6.38$; $\alpha = 15°$; $\Delta F = -20°$; normal span; $N_{Re,L_r} = 1.41 \times 10^7$; $P'_o = 89.28$ psia; $H_o = 1.35 \times 10^7$ ft-lb/slug.

Figure 12.- Continued.

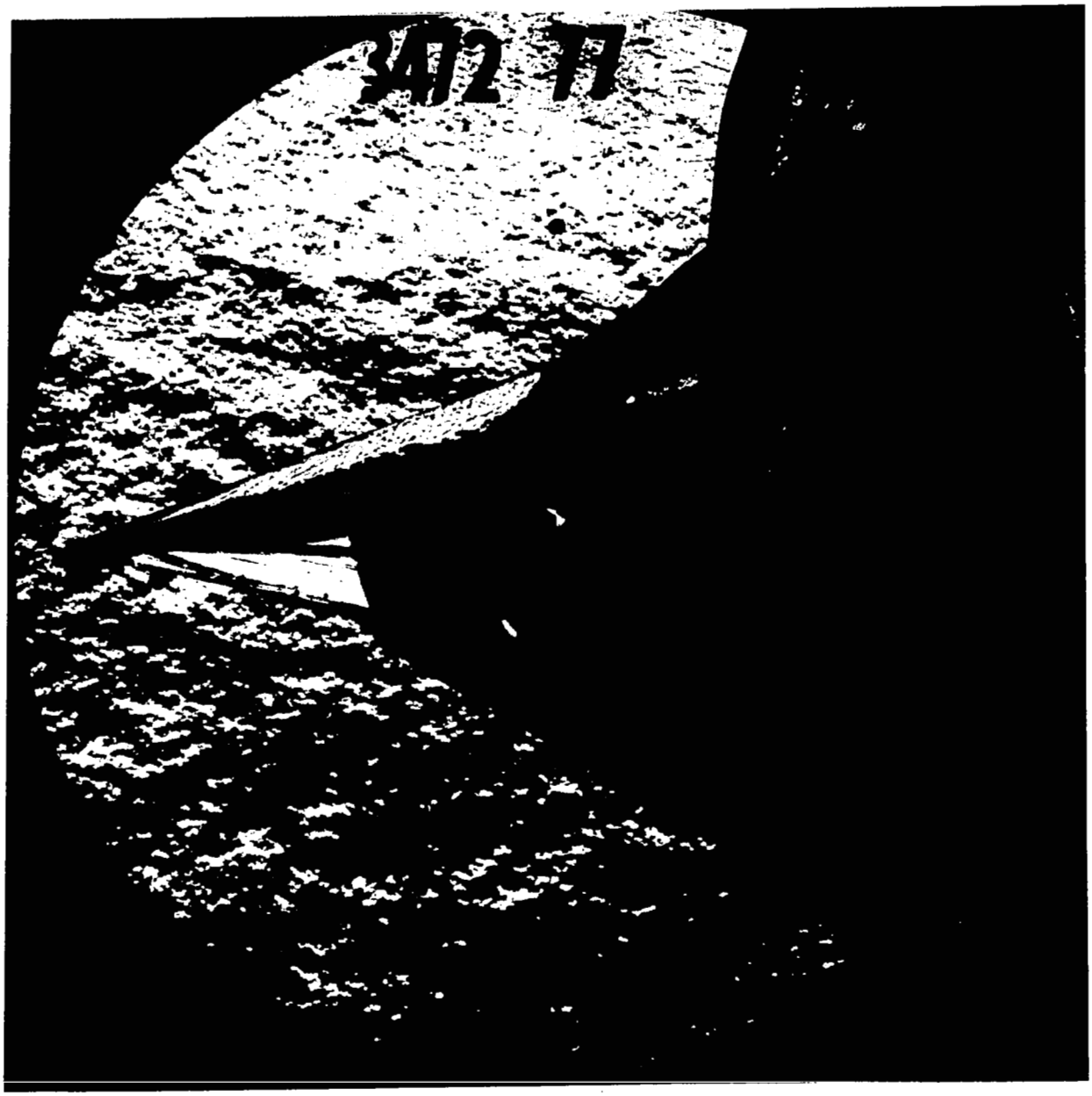

(c) $M_\infty = 6.38$; $\alpha = 15°$; $\Delta F = 45°$; normal span; $N_{Re,L_r} = 1.36 \times 10^7$; $P'_o = 86.37$ psia; $H_o = 1.35 \times 10^7$ ft-lb/slug.

Figure 12.- Continued.

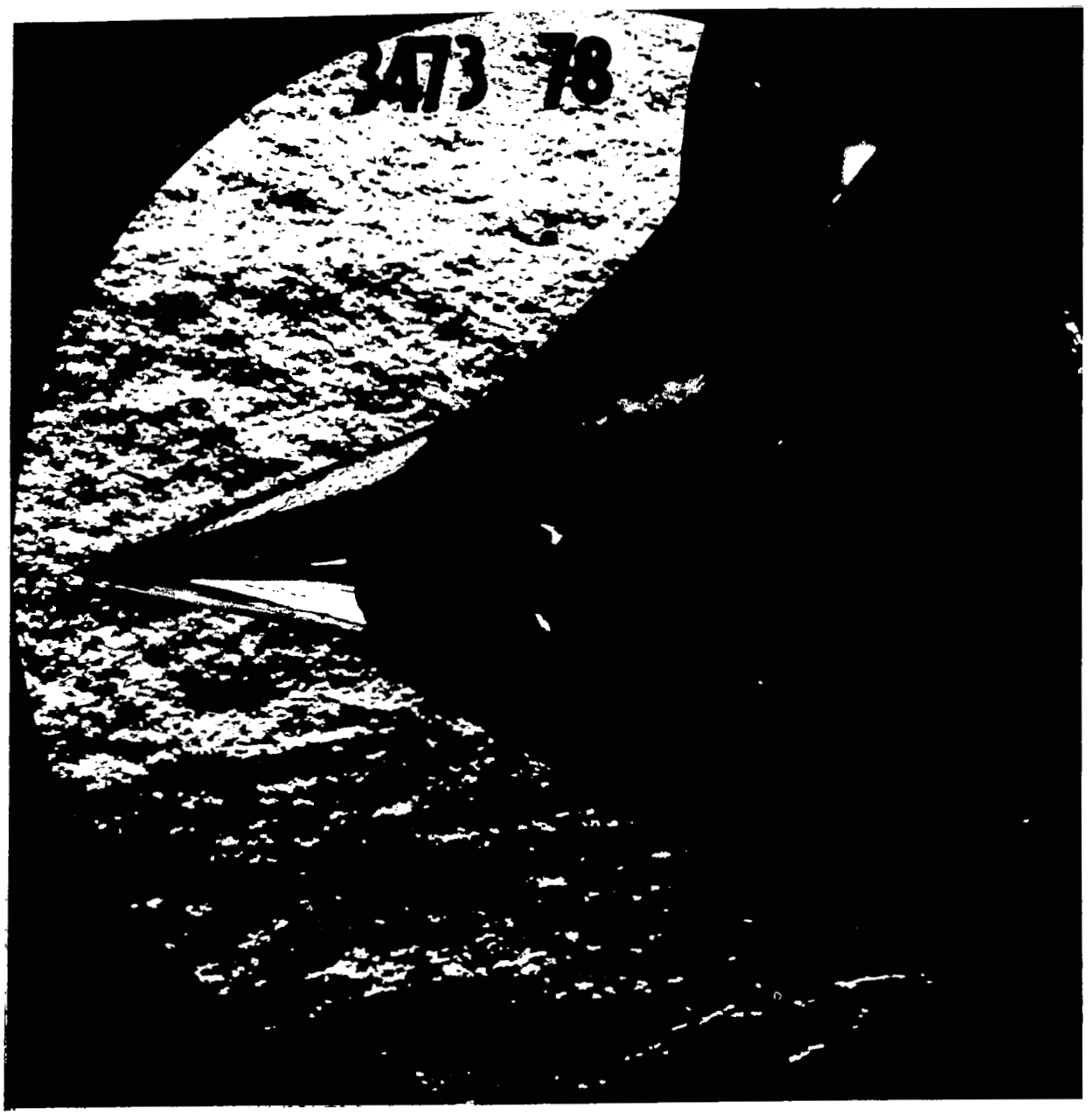

(d) $M_\infty = 6.37$; $\alpha = 15°$; $\Delta F = 45°$; extended span; $N_{Re,L_r} = 1.39 \times 10^7$; $P'_o = 89.52$ psia; $H_o = 1.36 \times 10^7$ ft-lb/slug.

Figure 12.- Continued.

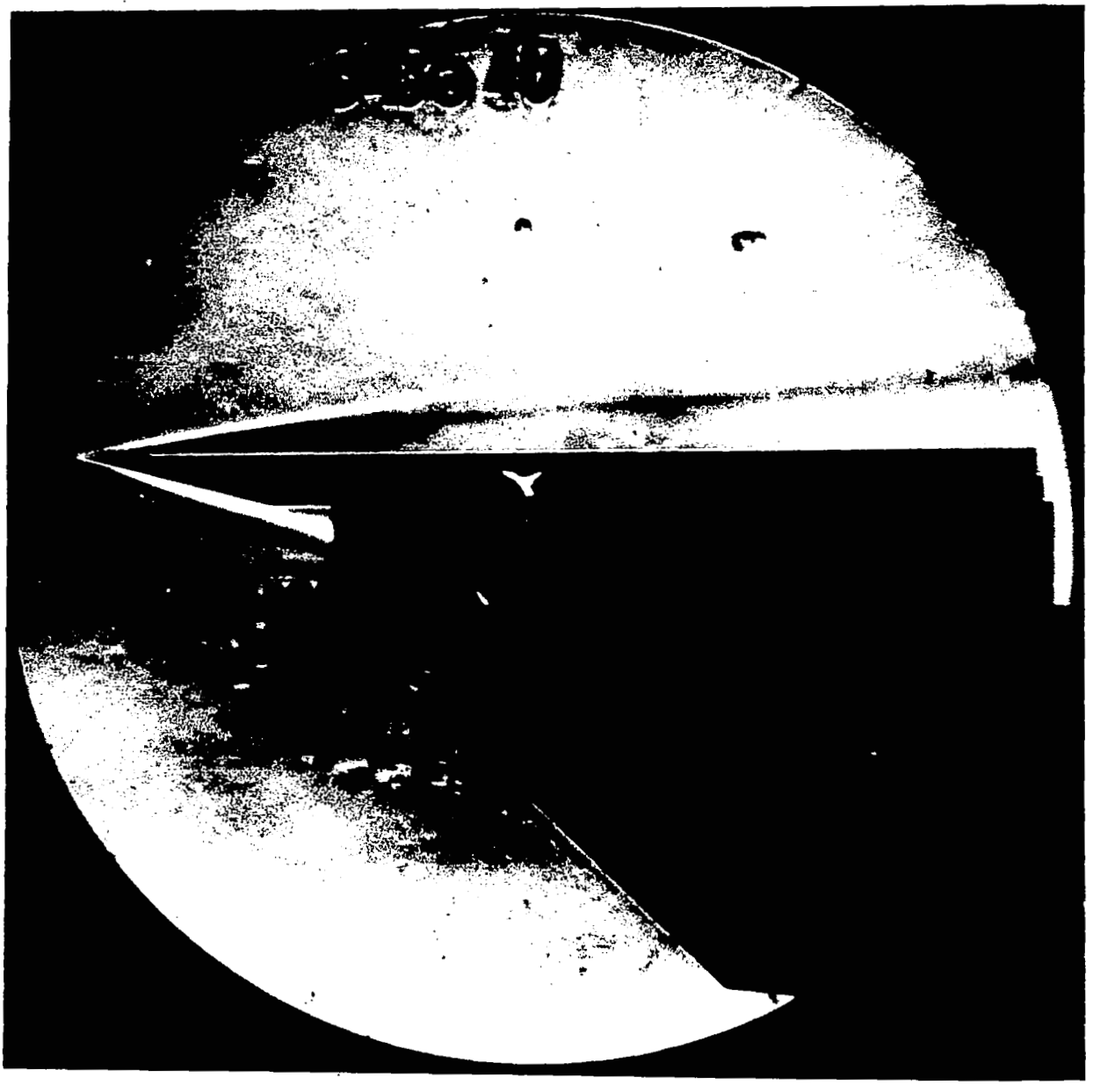

(e) $M = 15.15$; $\alpha = 0°$; $\Delta F = 0°$; normal span; $N_{Re,L_r} = 1.15 \times 10^5$; $P'_o = .4313$ psia; $H_o = 2.68 \times 10^7$ ft-lb/slug.

Figure 12.- Continued.

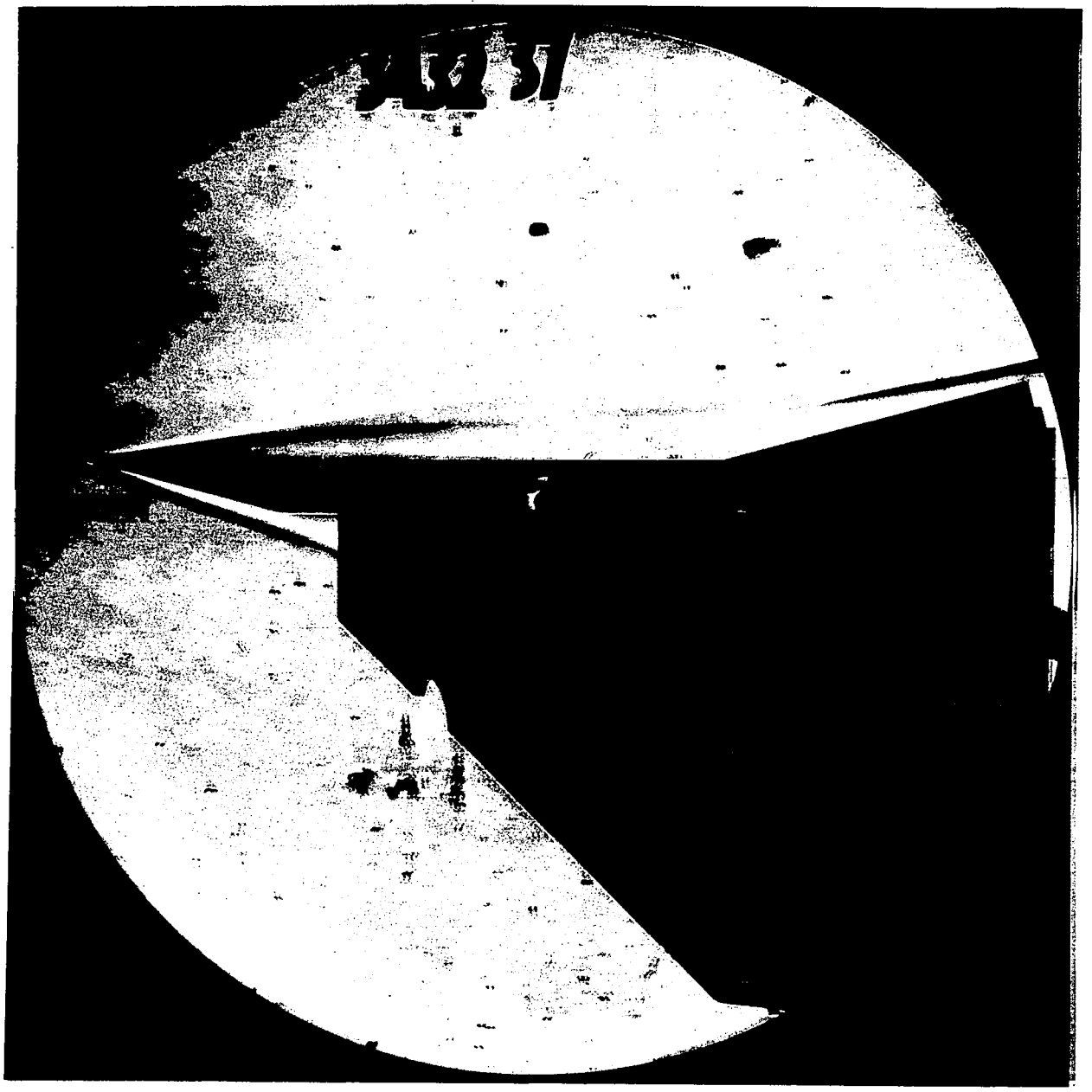

(f) $M_\infty = 15.14$; $\alpha = 0°$; $\Delta F = 15°$; normal span; $N_{Re,L_r} = 1.17 \times 10^5$; $P'_o = .4519$ psia; $H_o = 2.73 \times 10^7$ ft-lb/slug.

Figure 12.- Continued.

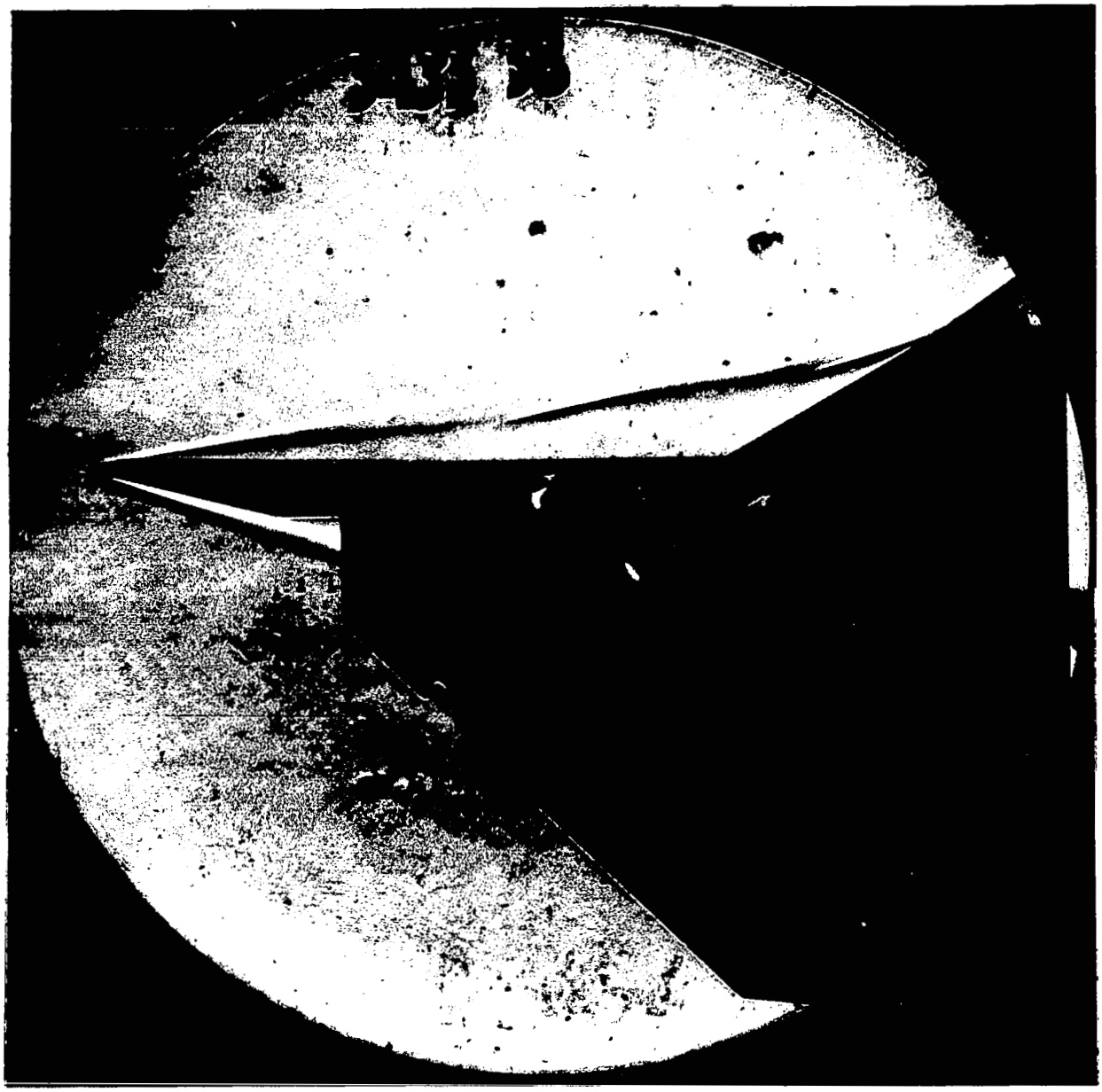

(g) $M_\infty = 15.12$; $\alpha = 0°$; $\Delta F = 30°$; normal span; $N_{Re,L_r} = 1.15 \times 10^5$; $P'_o = .4474$ psia; $H_o = 2.74 \times 10^7$ ft-lb/slug.

Figure 12.- Continued.

(h) $M_\infty = 15.23$; $\alpha = 0°$; $\Delta F = 45°$; extended span; $N_{Re,L_r} = 1.21 \times 10^5$; $P'_o = .4268$ psia; $H_o = 2.59 \times 10^7$ ft-lb/slug.

Figure 12.- Concluded.

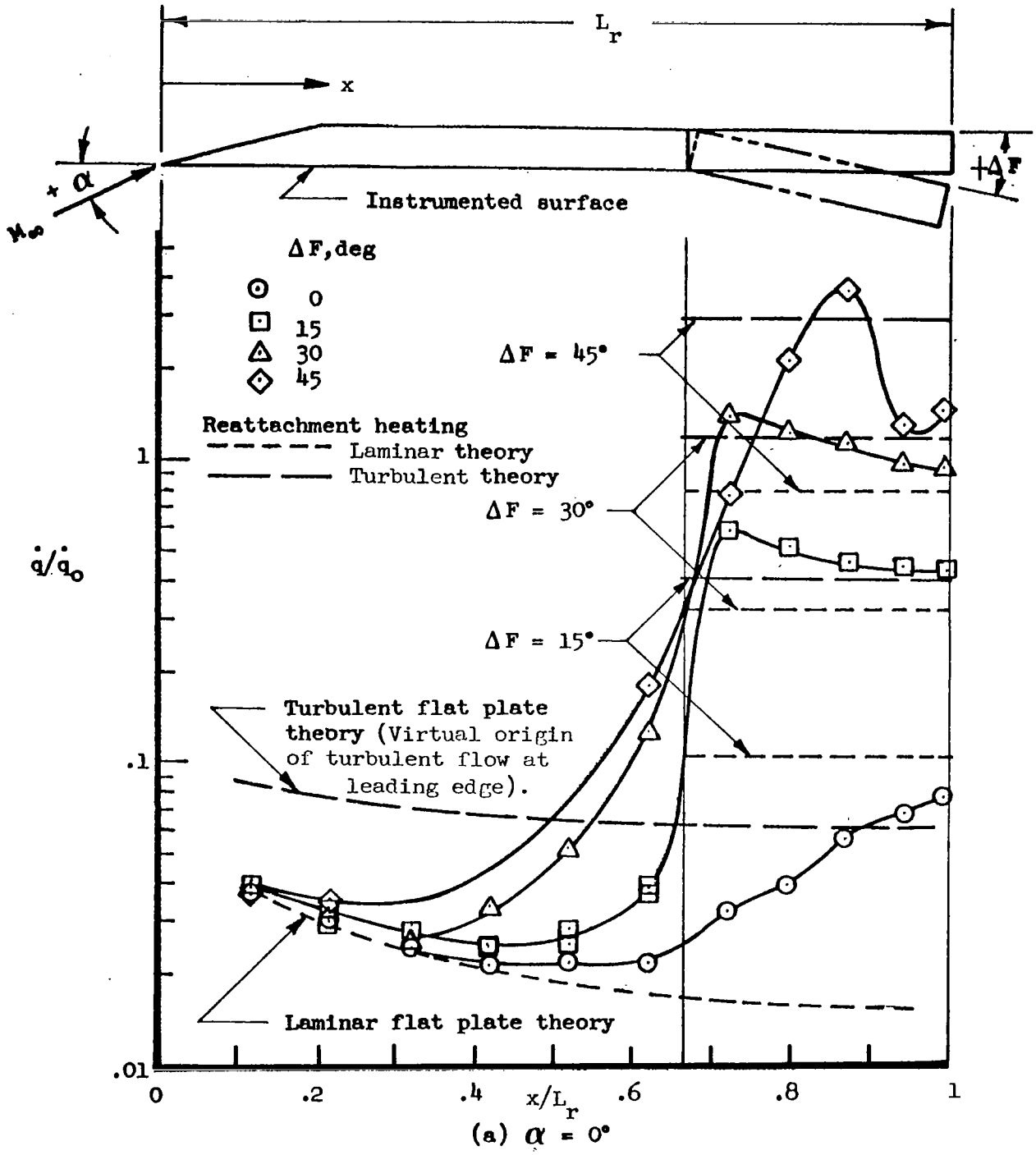

(a) α = 0°

Figure 13.- Heating rate distribution on sharp flat plate with deflected flap. M_∞ = 6.38; P'_o = 89.3 psia; H_o = 13.5 x 10^6 ft-lb/slug; N_{Re,L_r} = 14.08 x 10^6; $\dot{q}_o$ = 196 Btu/ft^2-sec.

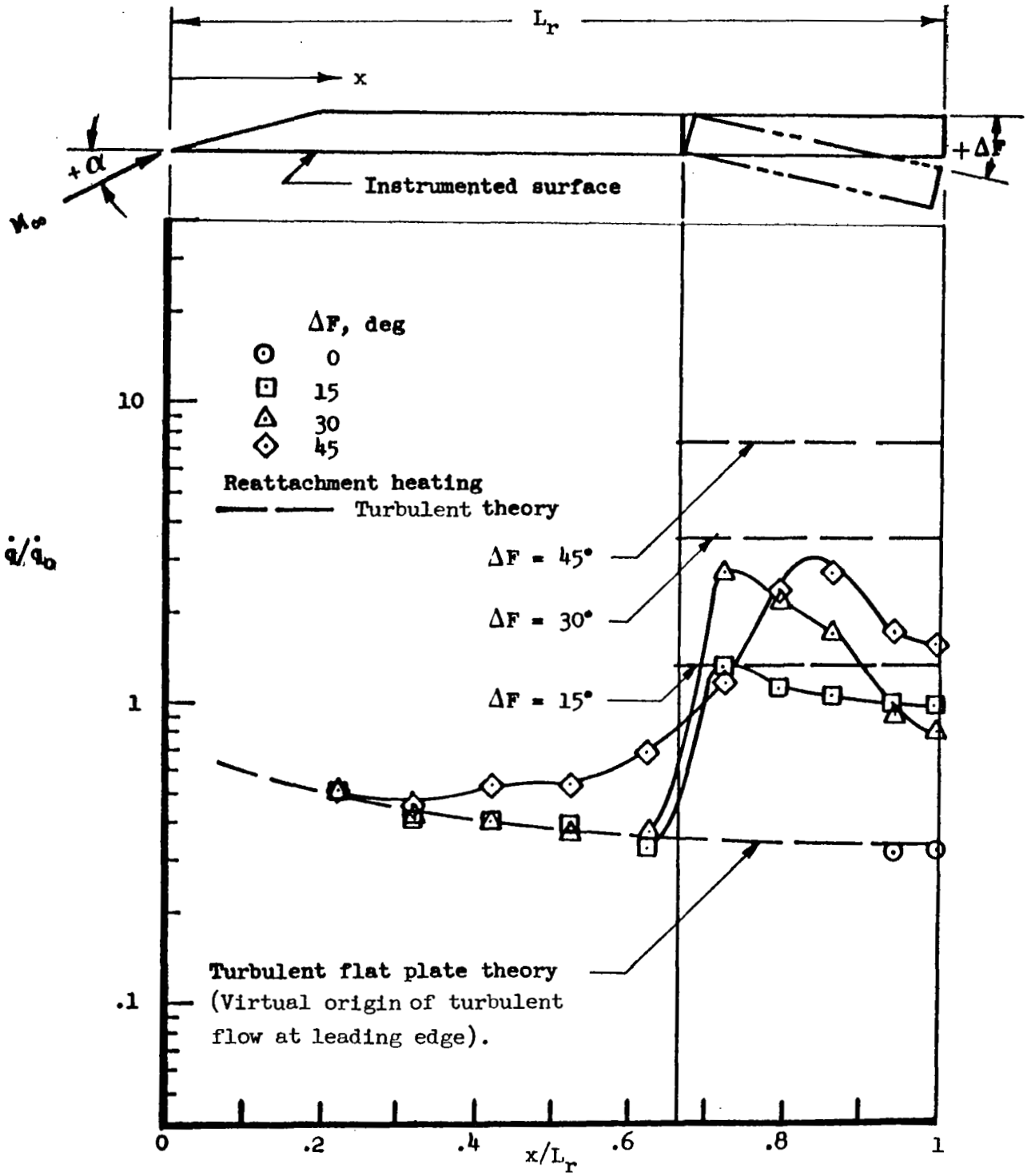

(b) $\alpha = 15°$

Figure 13.- Concluded.

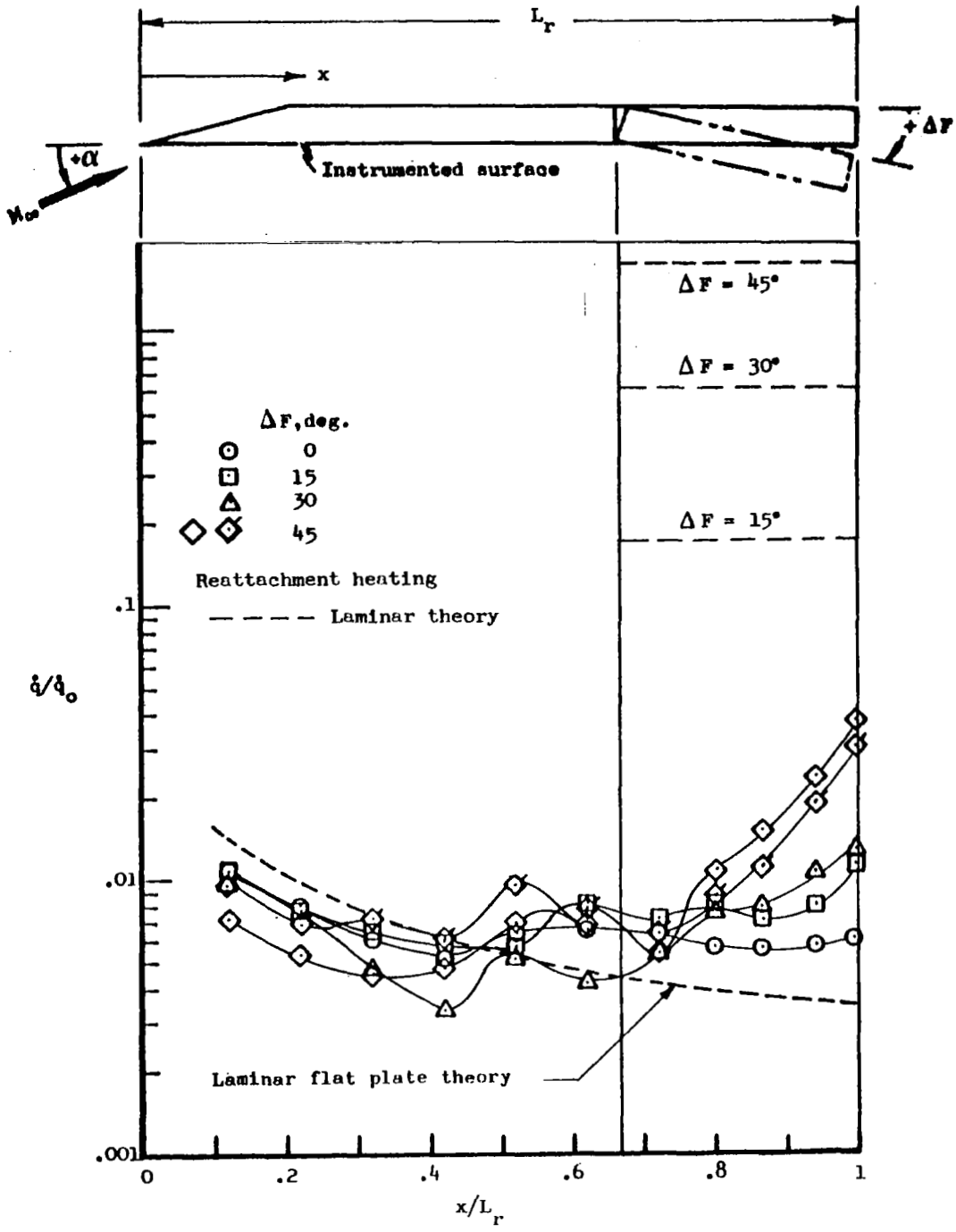

(a) α = -15°

Figure 14.-Heating rate distribution on sharp flat plate with deflected flaps. M_∞ = 15.15; P'_o = .424 psia; H_o = 27.2 x 10^6;ft-lb/slug; N_{Re,L_r} = .112 x 10^6; $\dot{q}_o$ = 32.9 Btu/ft^2-sec.

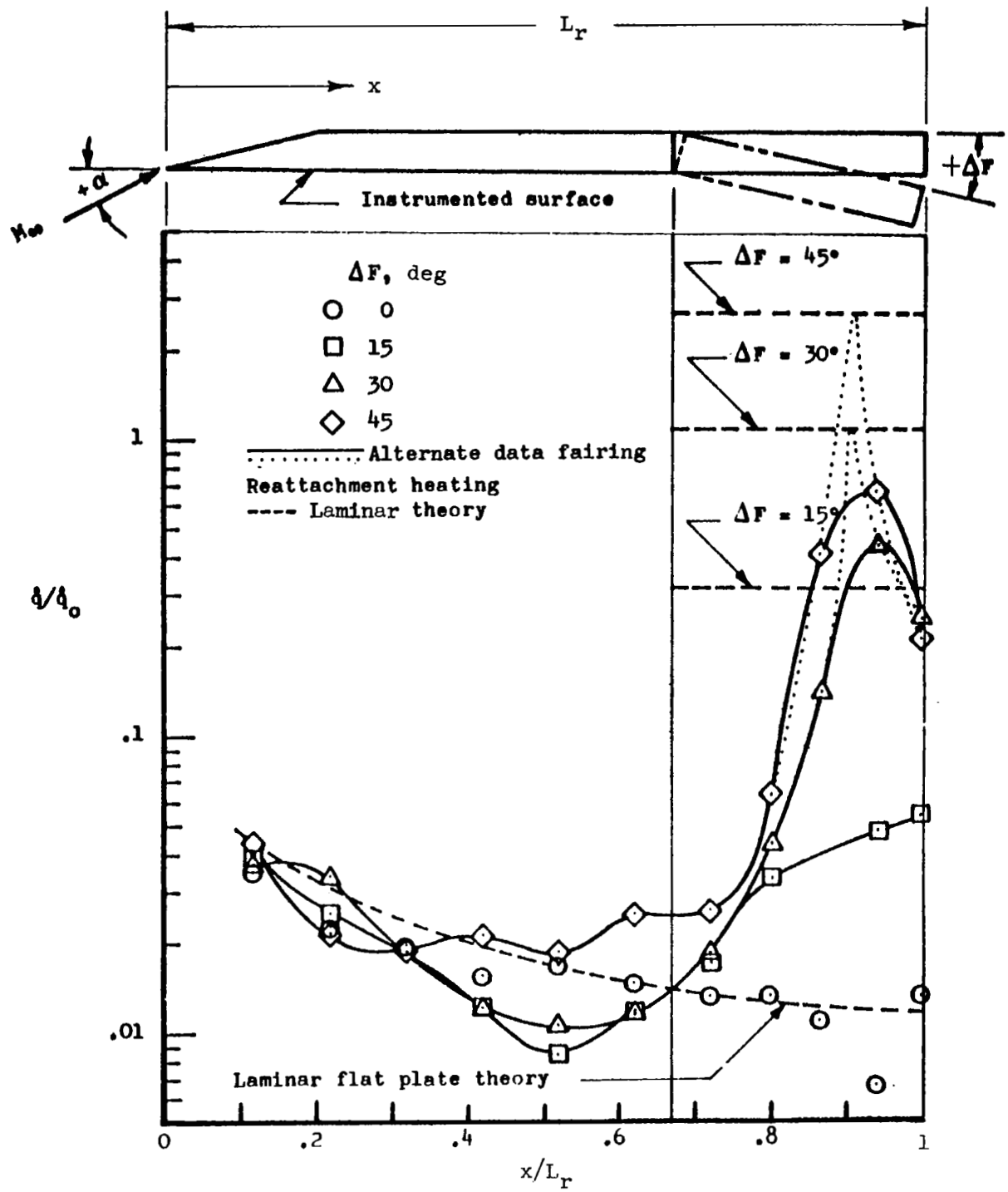

(b) α = 0°

Figure 14.- Continued.

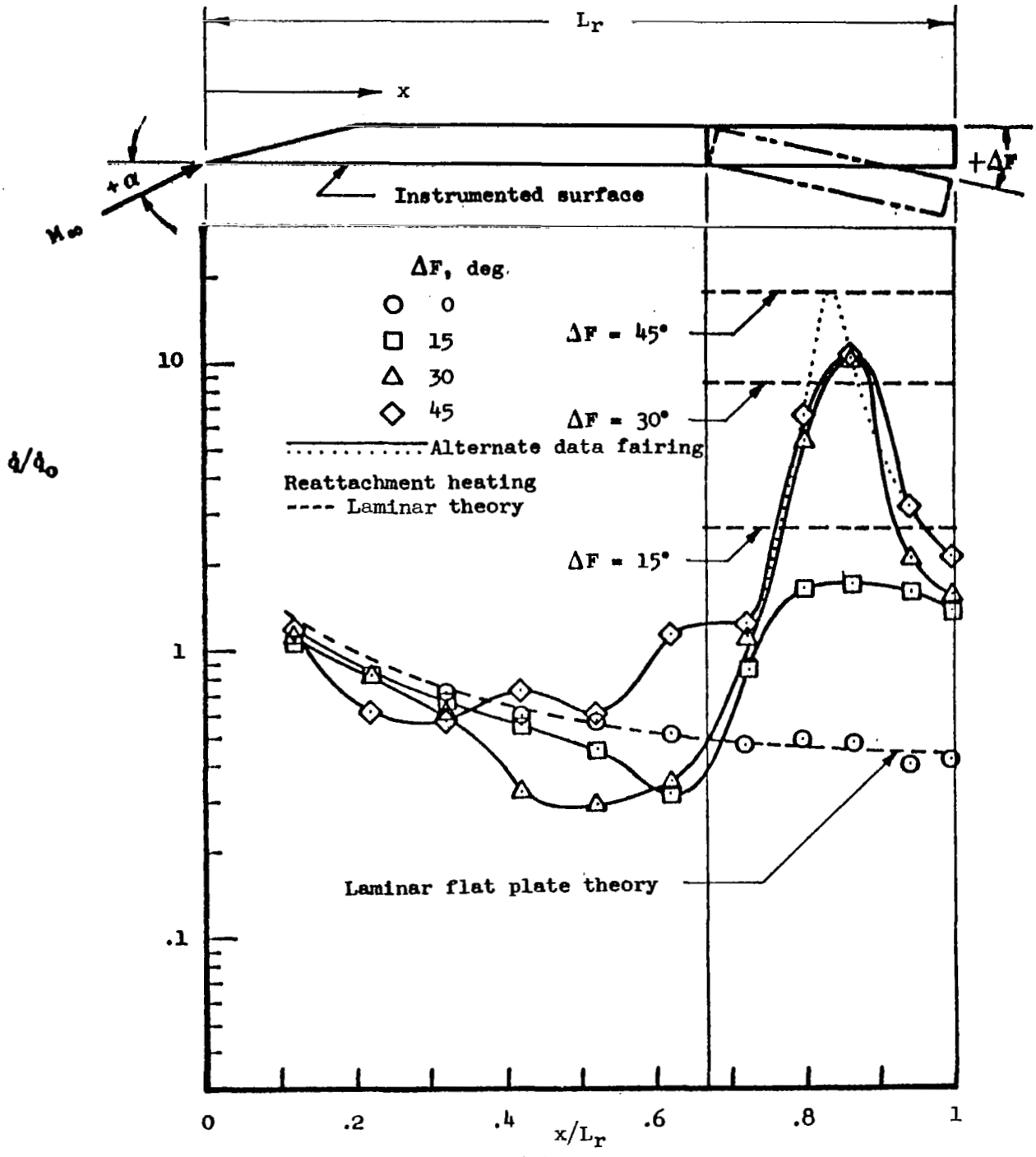

(c) α = 15°

Figure 14.- Concluded.

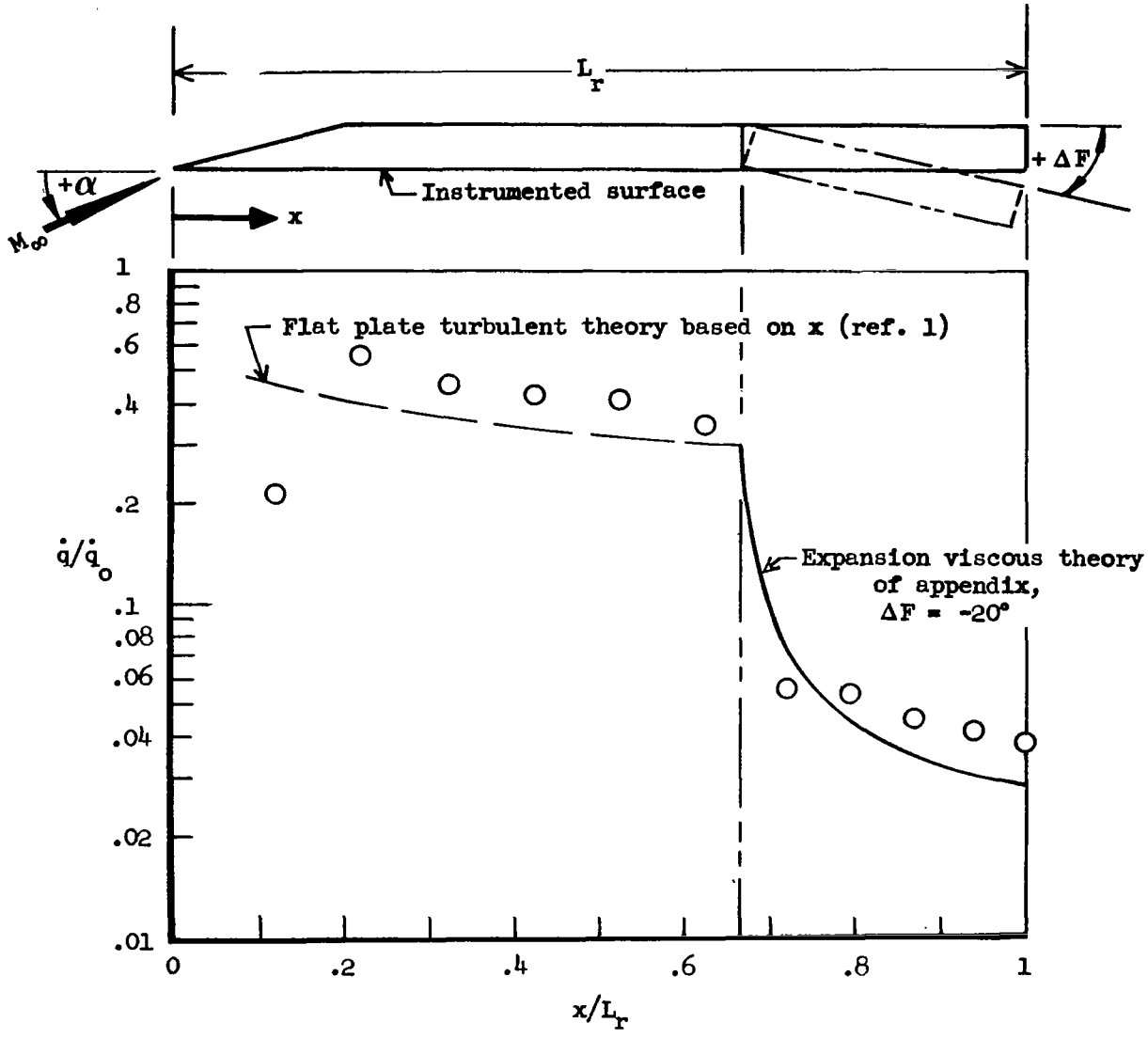

(a) $M_\infty = 6.38$; $N_{Re,L_r} = 14.09 \times 10^6$; turbulent boundary layer;
$P'_o = 89.28$ psia; $H_o = 13.3 \times 10^6$ ft-lb/slug;
$\dot{q}_o = 199$ Btu/ft^2-sec

Figure 15.- Heating rate distribution on a sharp flat plate with expanding flow over a deflected flap. $\alpha = 15°$.

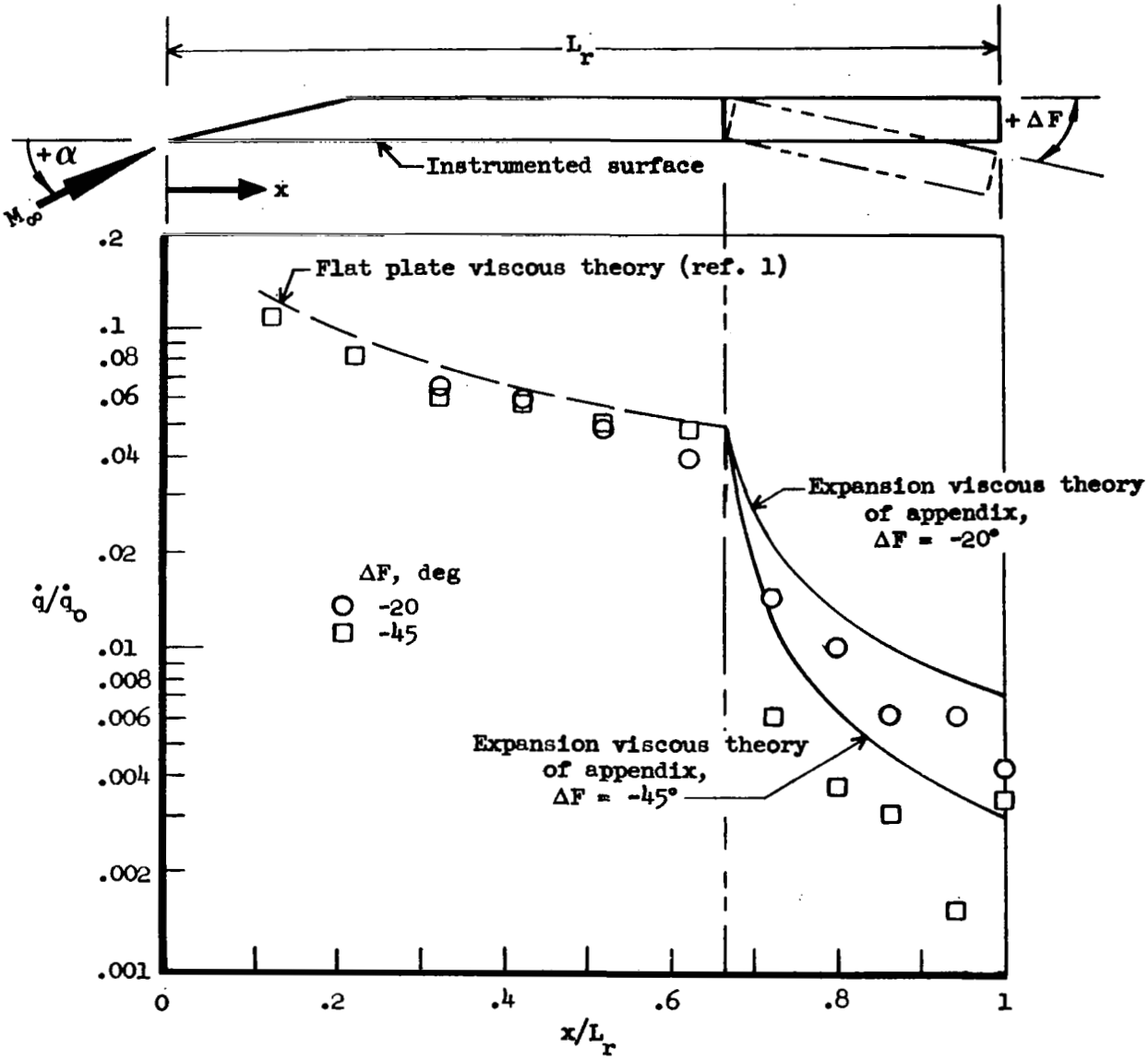

(b) $M_\infty = 15.15$; $N_{Re,L_r} = .109 \times 10^6$; laminar boundary layer;

$P'_o = .423$ psia; $H_o = 22.4 \times 10^6$ ft-lb/slug;

$\dot{q}_o = 33.6$ Btu/ft^2-sec

Figure 15.- Concluded.

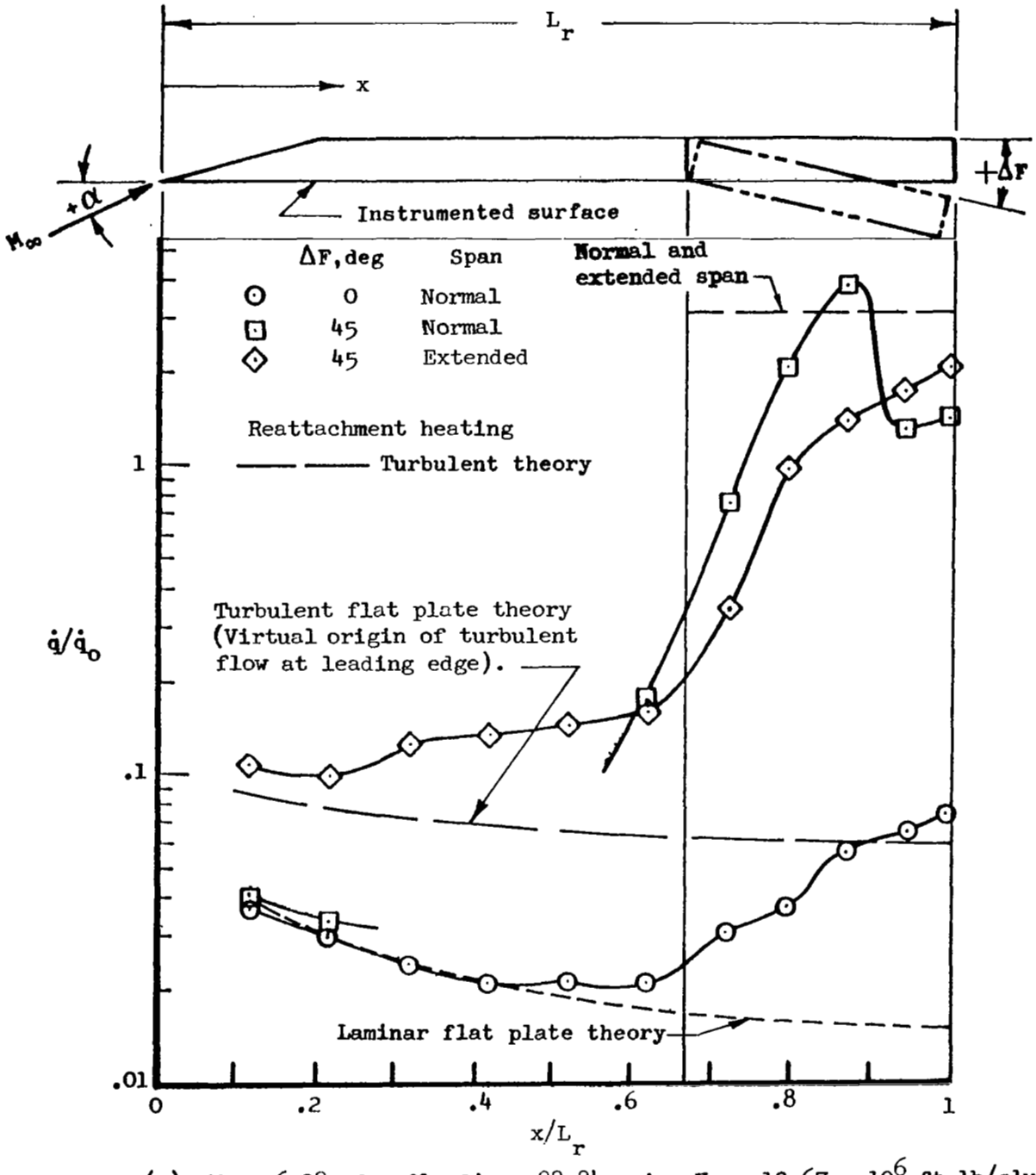

(a) $M_\infty = 6.38$; $\alpha = 0°$; $P'_o = 88.84$ psia; $H_o = 13.67 \times 10^6$ ft-lb/slug; $N_{Re,L_r} = 13.69 \times 10^6$; $\dot{q}_o = 199$ Btu/ft^2-sec.

Figure 16.- Effect of span on heating rate distribution on a sharp flat plate with deflected flap.

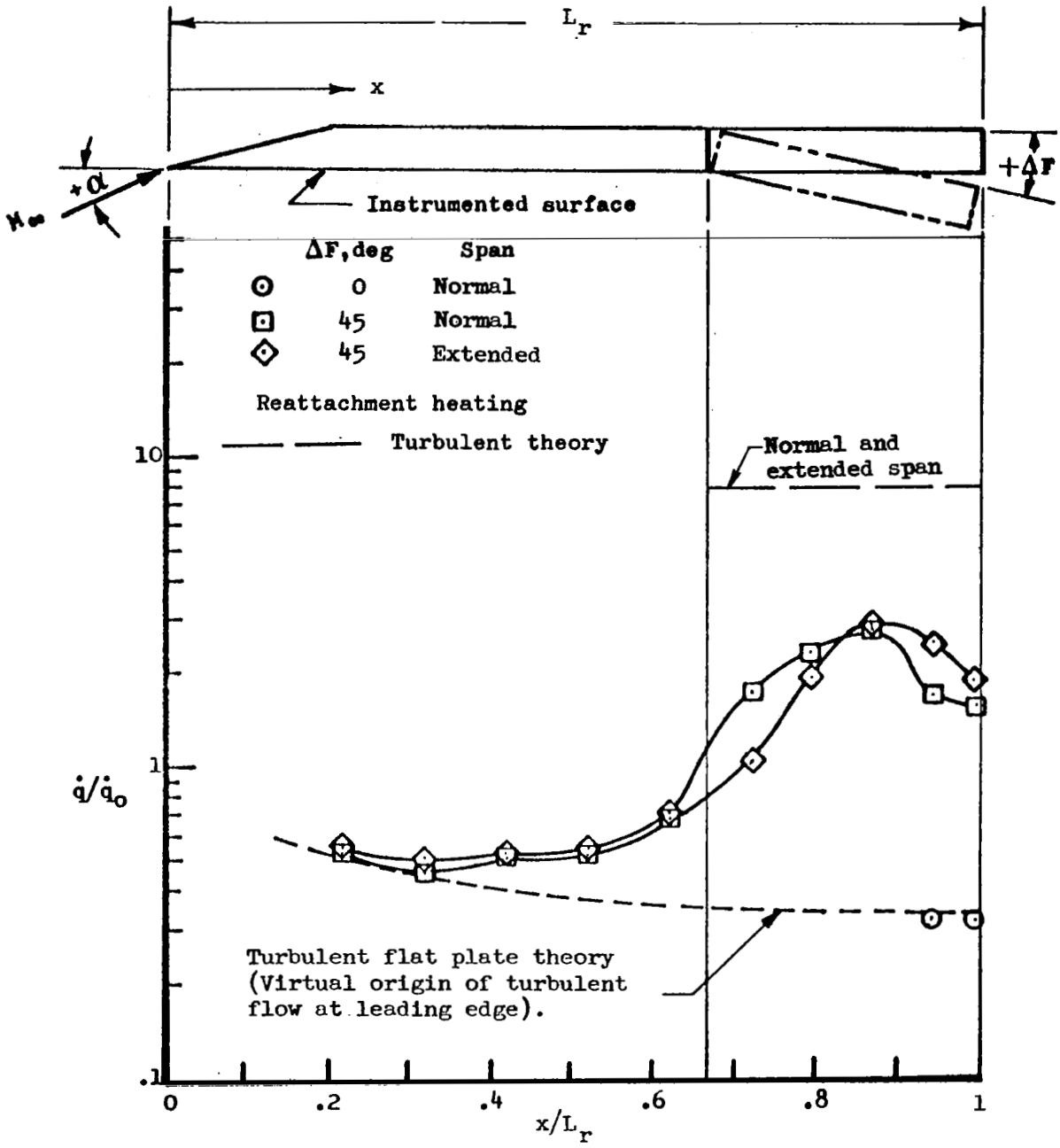

(b) $M_\infty = 6.38$; $\alpha = 15°$; P' = 88.58 psia; $H_o = 13.47 \times 10^6$ ft-lb/slug;

$N_{Re,L_r} = 13.97 \times 10^6$; $\dot{q}_o = 194$ Btu/ft^2-sec.

Figure 16.- Continued.

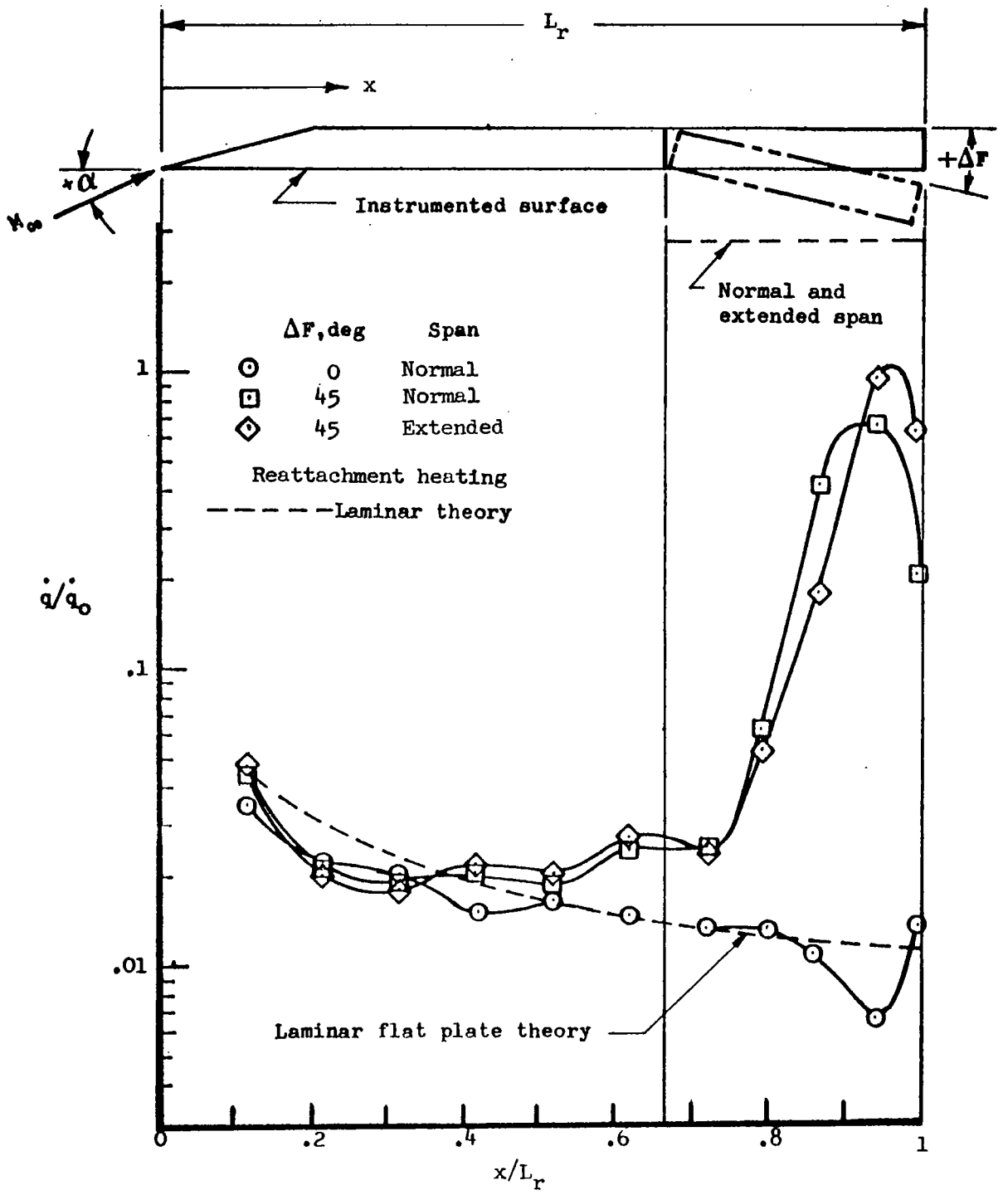

(c) $M_\infty = 15.15$; $\alpha = 0^o$; $P'_o = .434$ psia; $H_o = 26.6 \times 10^6$ ft-lb/slug;

$N_{Re,L_r} = .117 \times 10^6$; $\dot{q}_o = 32.27$ Btu/ft^2-sec.

Figure 16.- Continued.

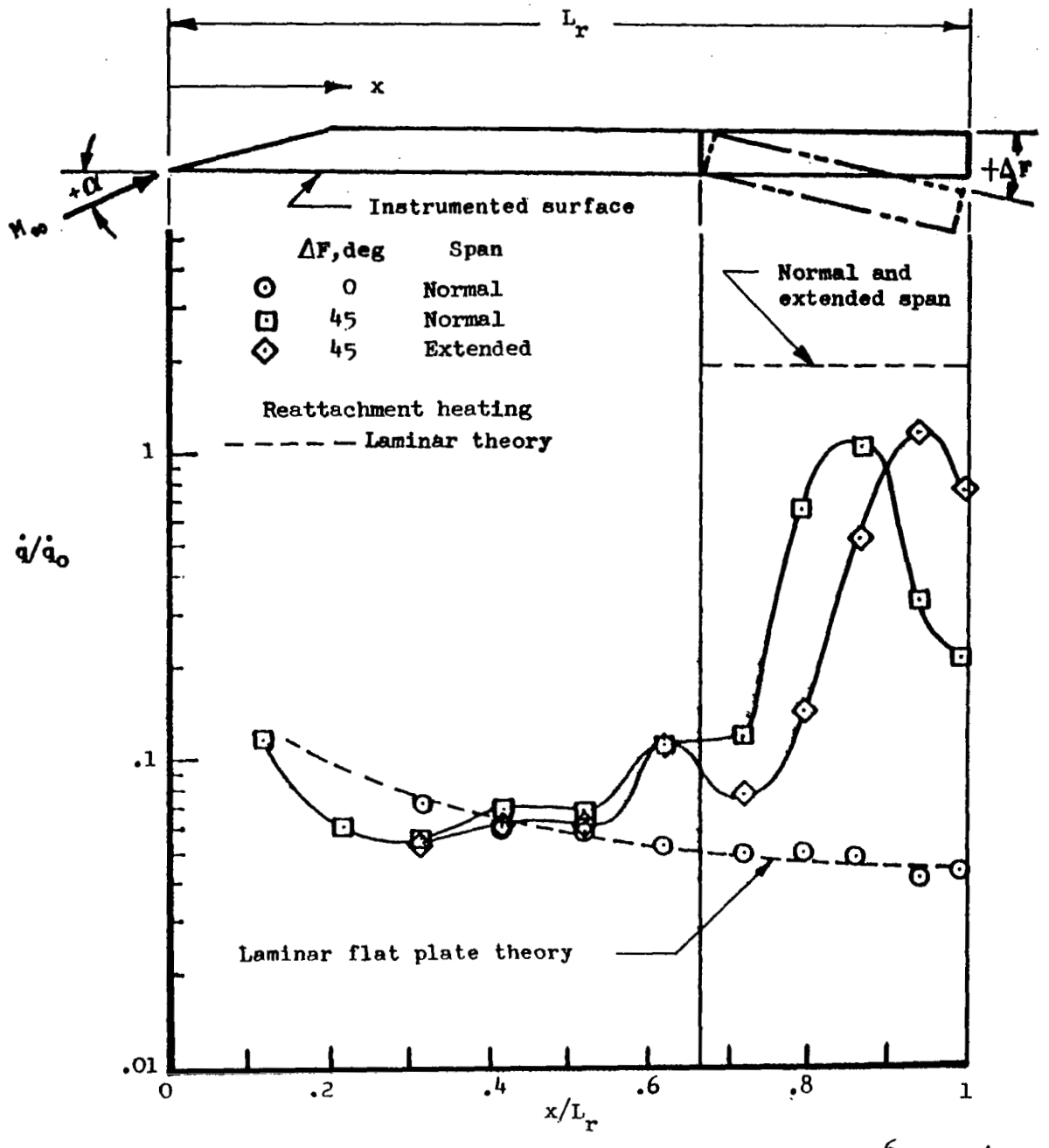

(d) $M_\infty = 15.15$; $\alpha = 15°$; $P'_o = .421$ psia; $H_o = 27.1 \times 10^6$ ft-lb/slug;

$N_{Re,L_r} = .112 \times 10^6$; $\dot{q}_o = 32.3 \times$ Btu/ft^2-sec.

Figure 16.- Concluded.

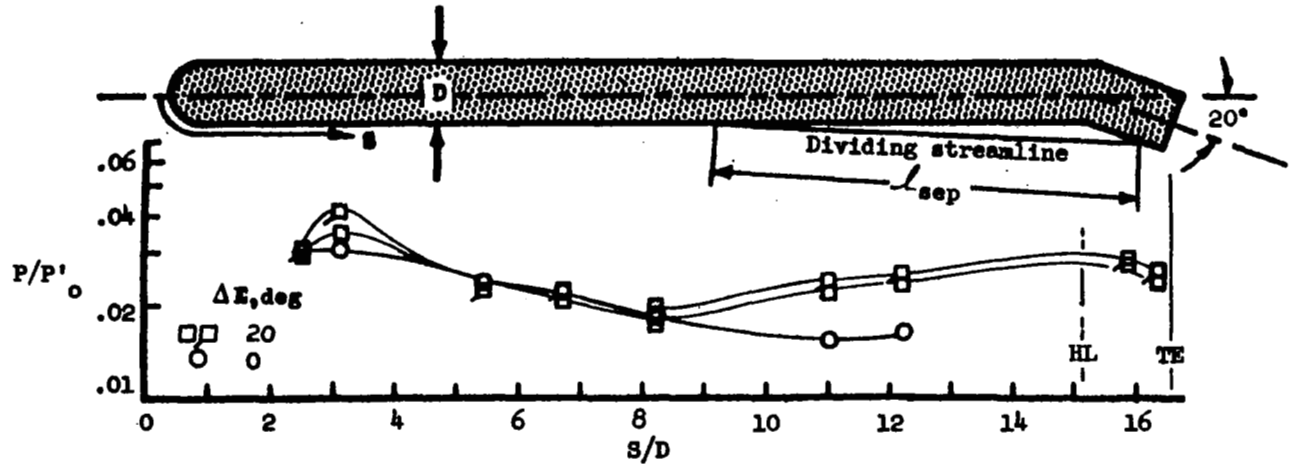

(a) $\alpha = 0^\circ$, $\Delta E = 20^\circ$

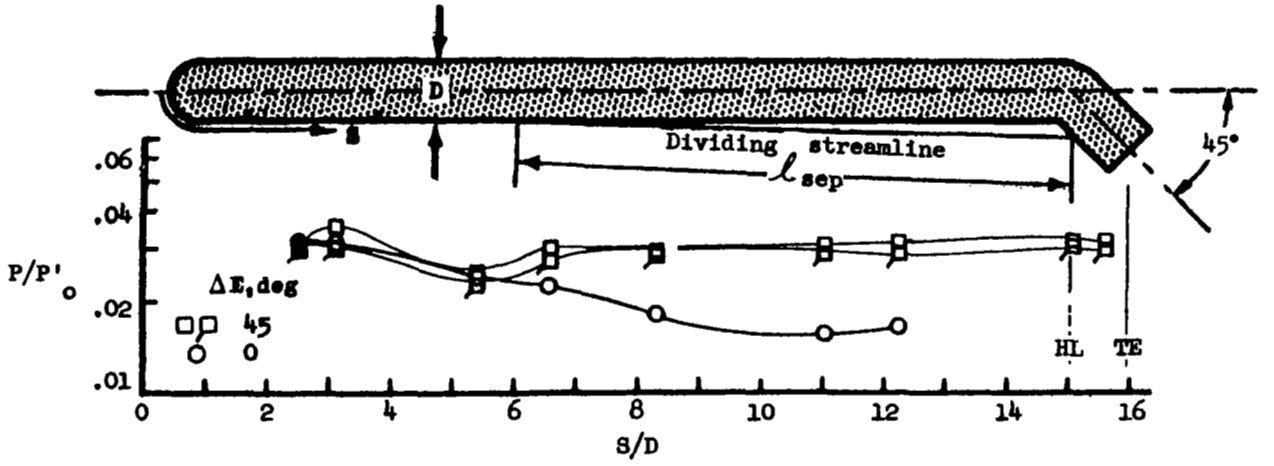

(b) $\alpha = 0^\circ$, $\Delta E = 45^\circ$

Figure 17.- Pressure distribution along a 6° ray line on the lower surface of a blunt delta wing with deflected elevons.

$M_\infty = 8.08$; $\Lambda = 73^\circ$; $N_{Re,L_r} = 1.202 \times 10^6$;

$P'_o = 1.63$ psia; $H_o = 7.5 \times 10^6$ ft-lb/slug.

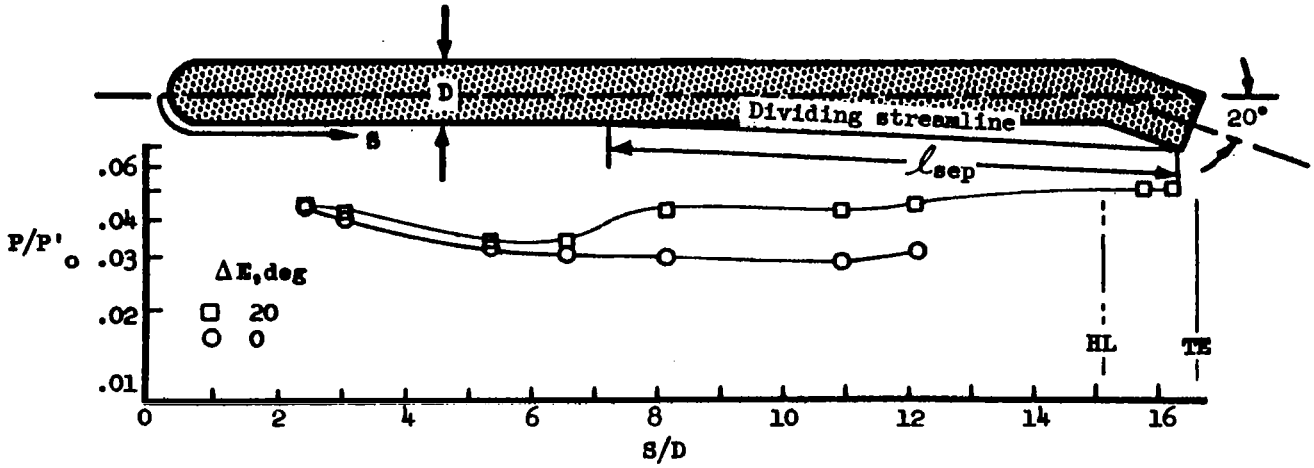

(c) $\alpha = 5^{\circ}$, $\Delta E = 20^{\circ}$

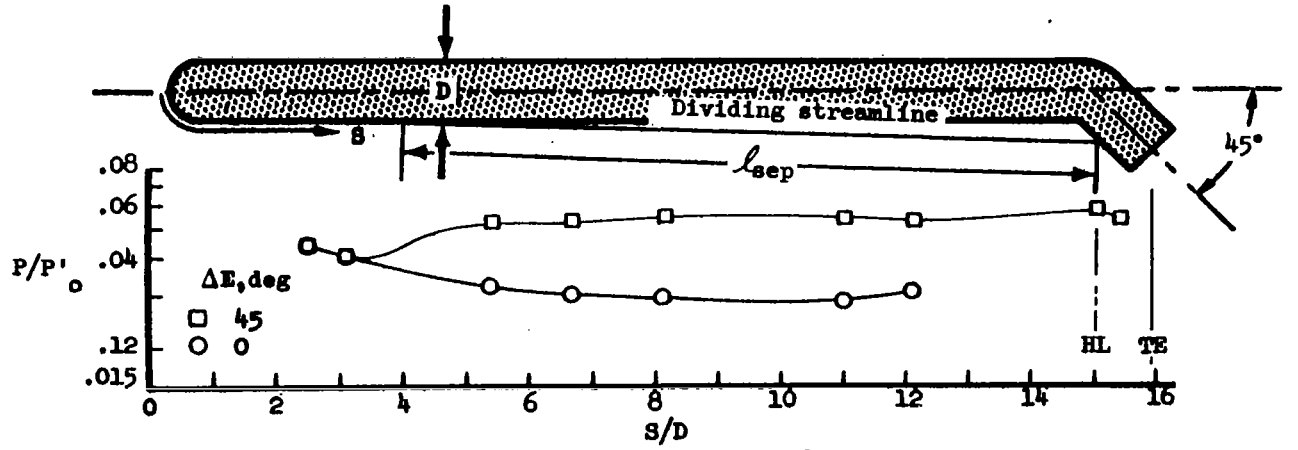

(d) $\alpha = 5^{\circ}$, $\Delta E = 45^{\circ}$

Figure 17.- Continued.

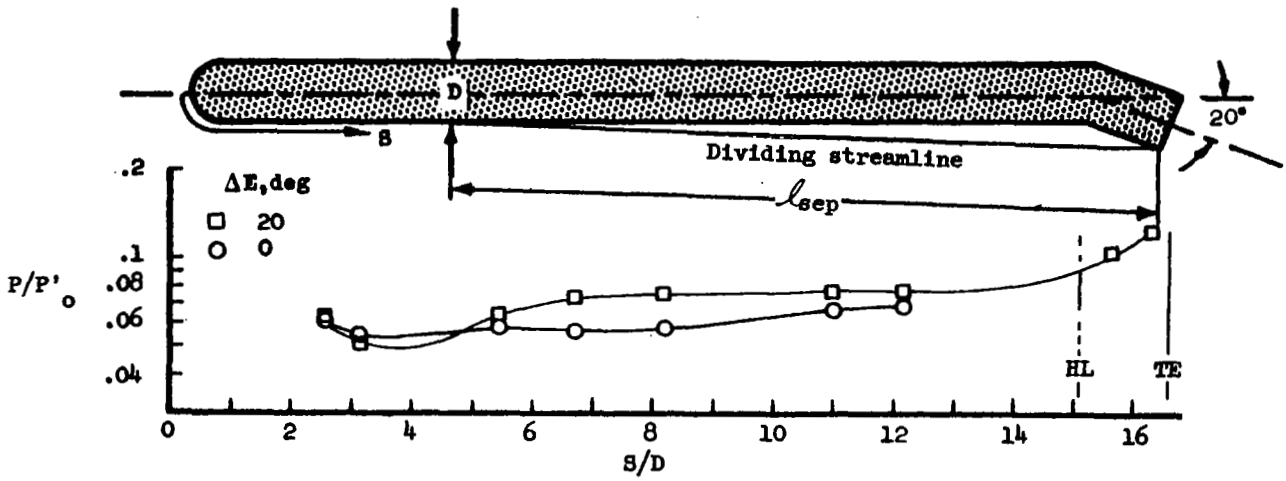

(e) $\alpha = 10°$, $\Delta E = 20°$

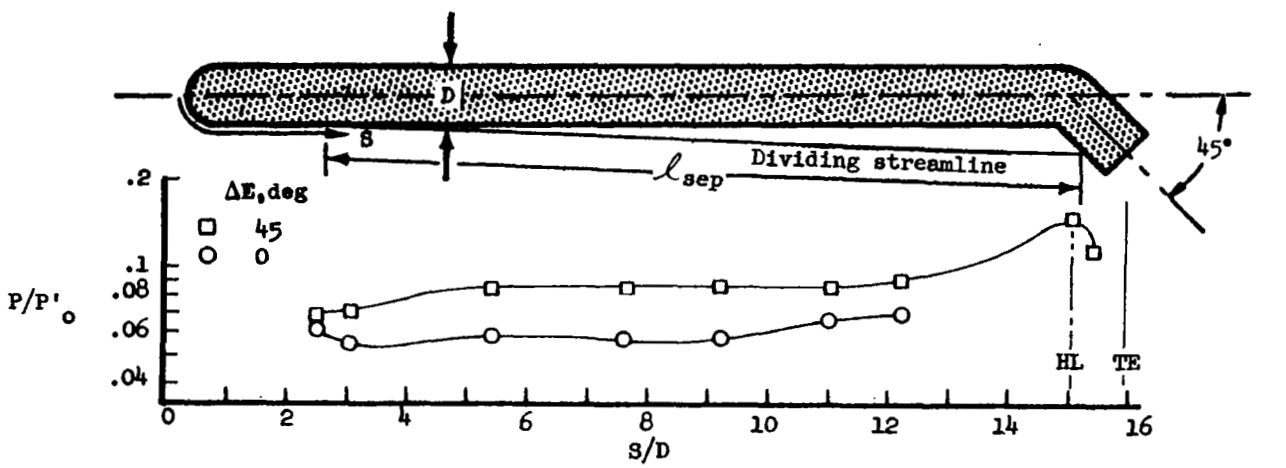

(f) $\alpha = 10°$, $\Delta E = 45°$

Figure 17.- Continued.

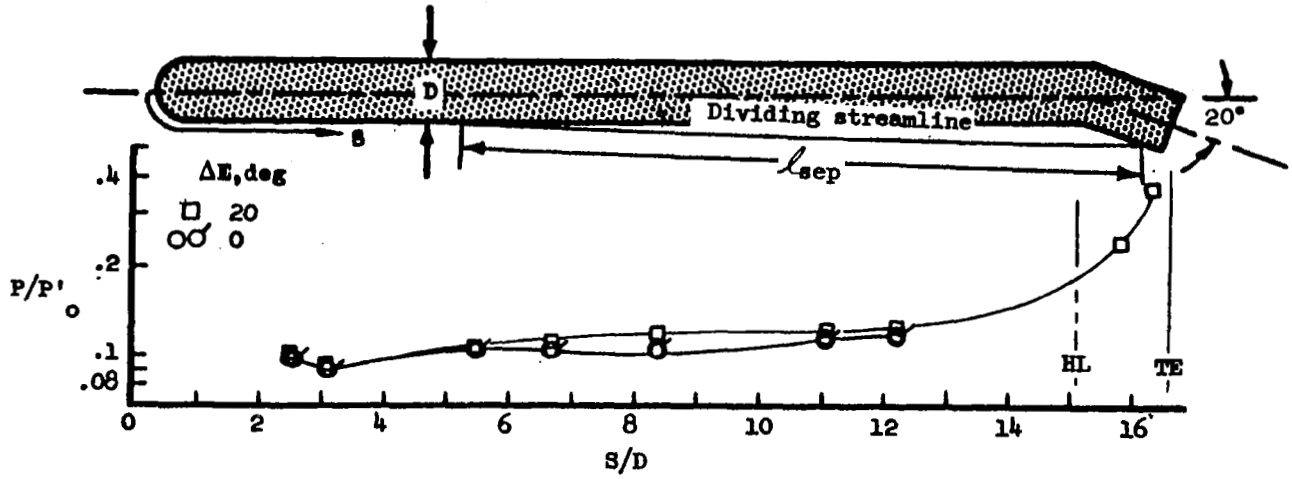

(g) $\alpha = 15°$, $\Delta E = 20°$

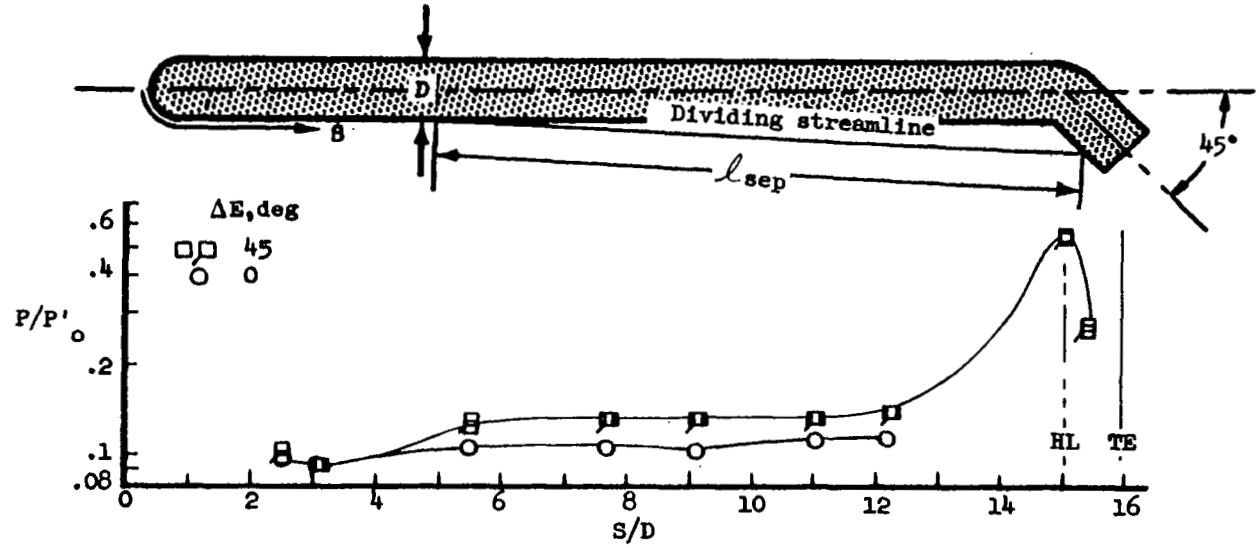

(h) $\alpha = 15°$, $\Delta E = 45°$

Figure 17.- Continued.

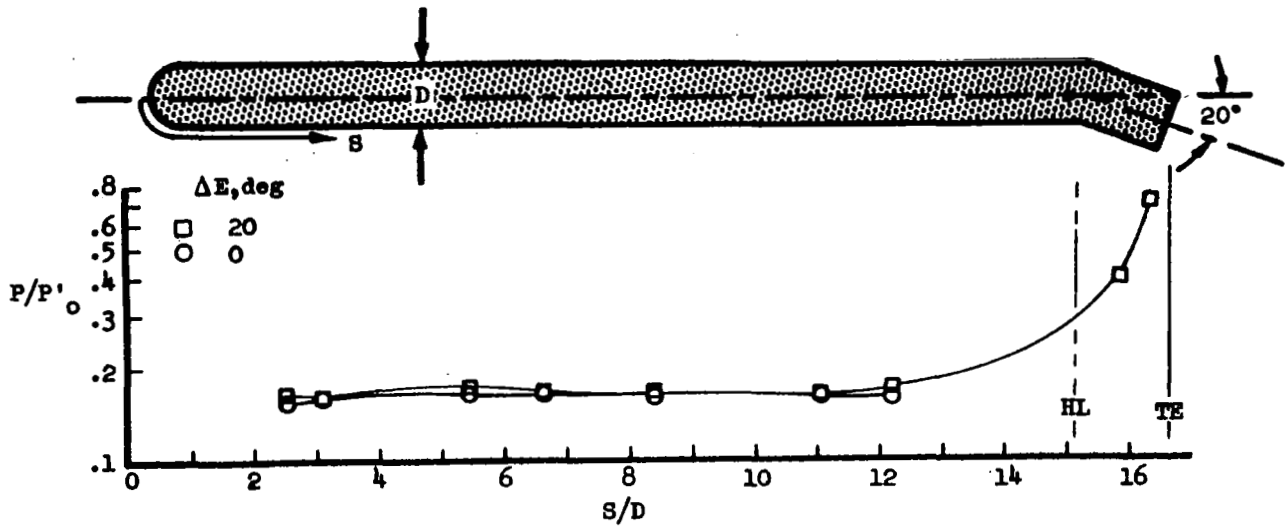

(i) $\alpha = 20^{\circ}$, $\Delta E = 20^{\circ}$

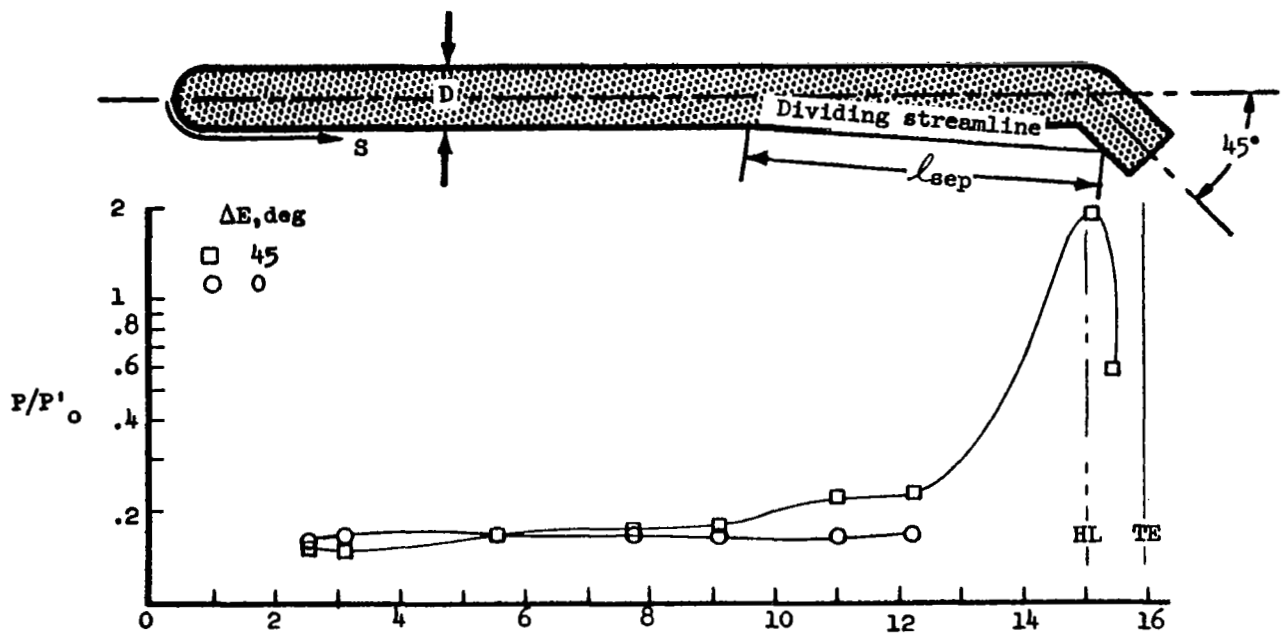

(j) $\alpha = 20^{\circ}$, $\Delta E = 45^{\circ}$

Figure 17.- Continued.

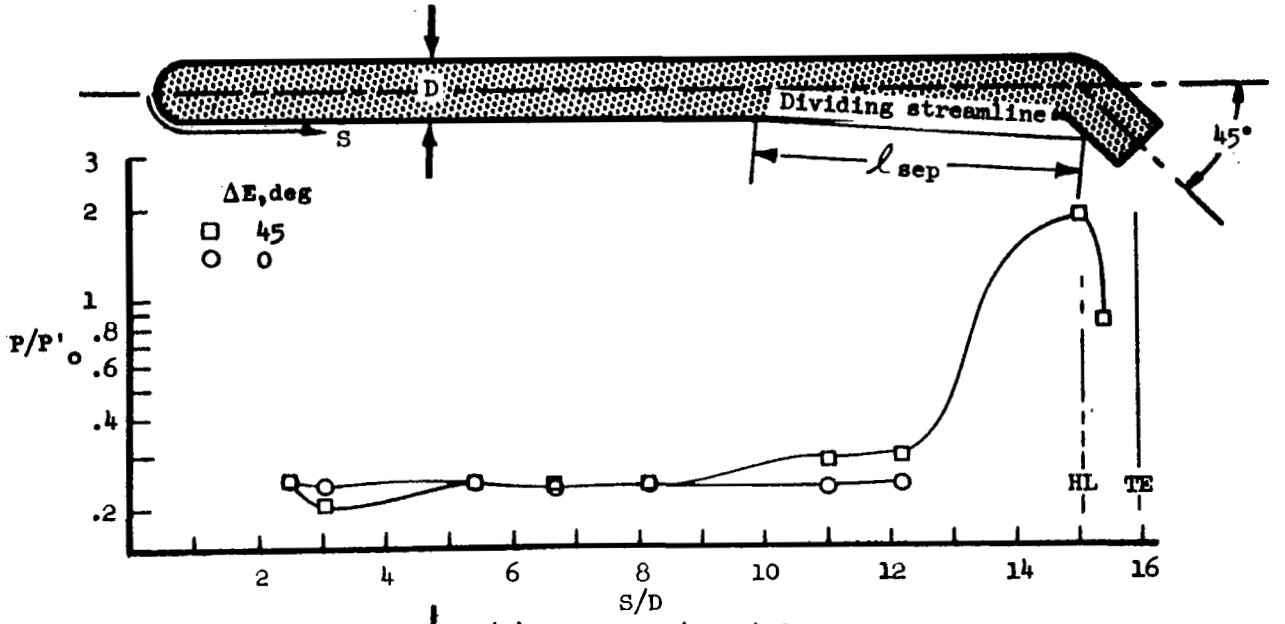

(k) $\alpha = 25°$, $\Delta E = 45°$

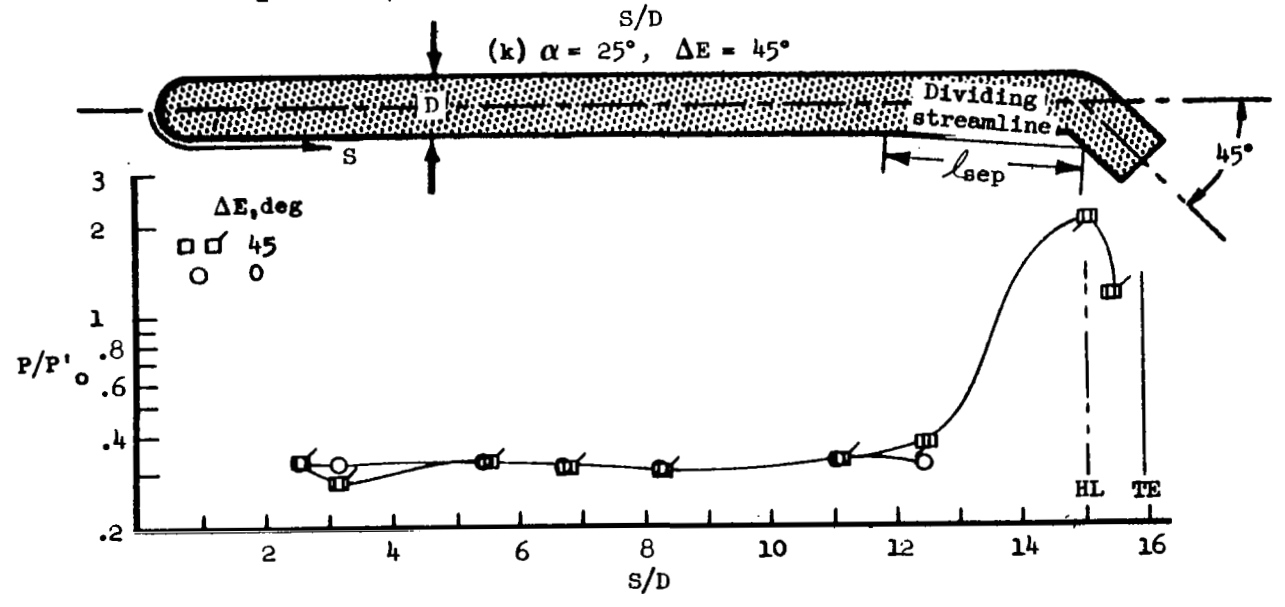

(l) $\alpha = 30°$, $\Delta E = 45°$

Figure 17.- Concluded.

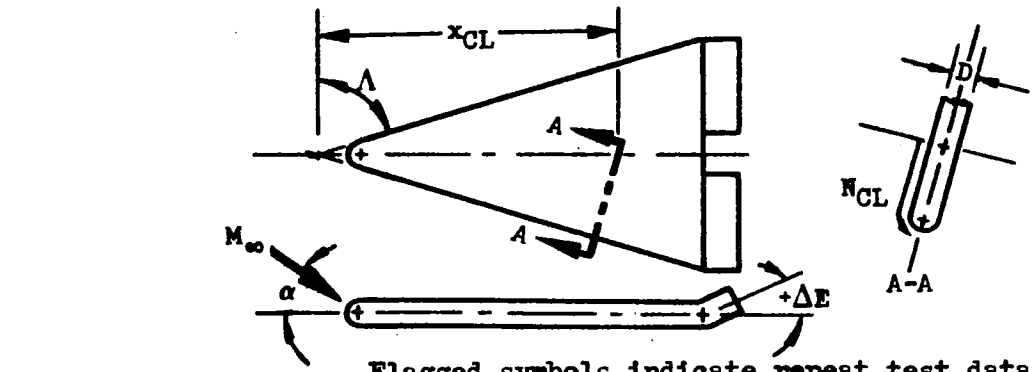

Flagged symbols indicate repeat test data

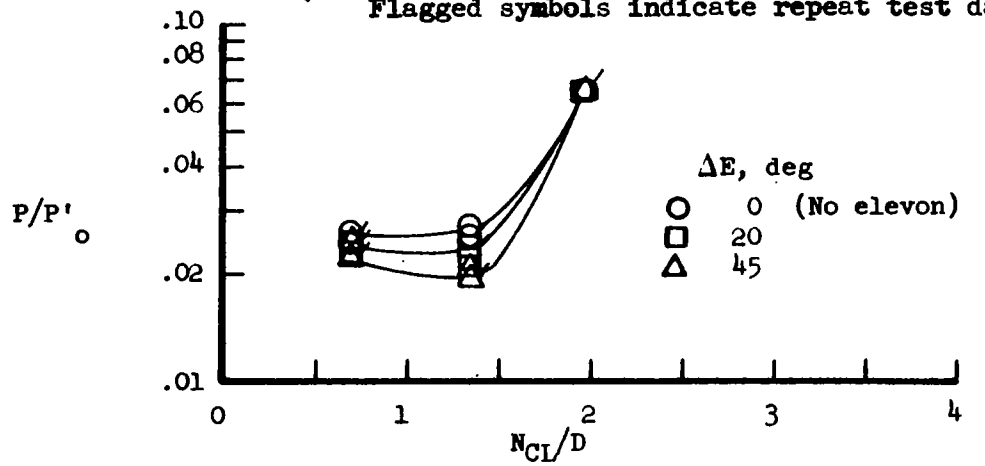

(a) $\alpha = 0°$, $x_{CL}/D = 6.38$

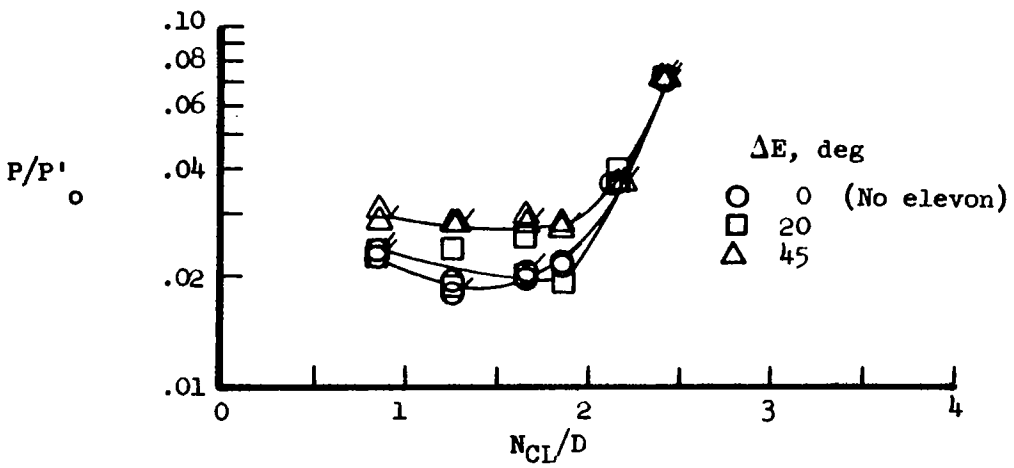

(b) $\alpha = 0°$, $x_{CL}/D = 7.85$

Figure 18.- Lower surface spanwise pressure distribution on a blunt delta wing with deflected elevons.
$M_\infty = 8.08$; $\Lambda = 73°$; $N_{Re,L_r} = 1.202 \times 10^6$;
$P'_o = 1.63$ psia; $H_o = 7.5 \times 10^6$ ft-lb/slug.

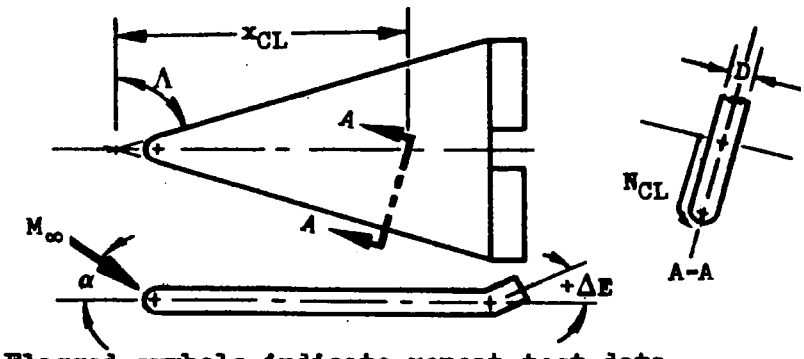

Flagged symbols indicate repeat test data

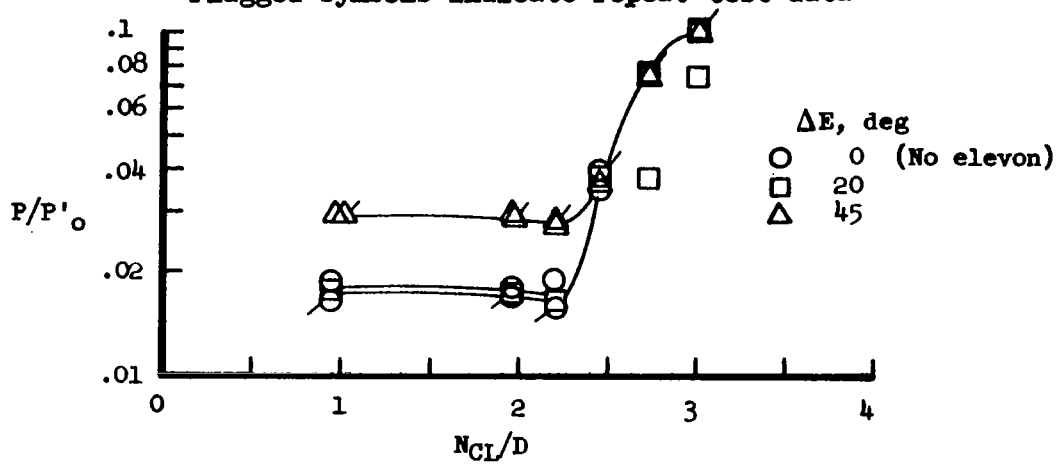

(c) $\alpha = 0°$, $x_{CL}/D = 9.32$

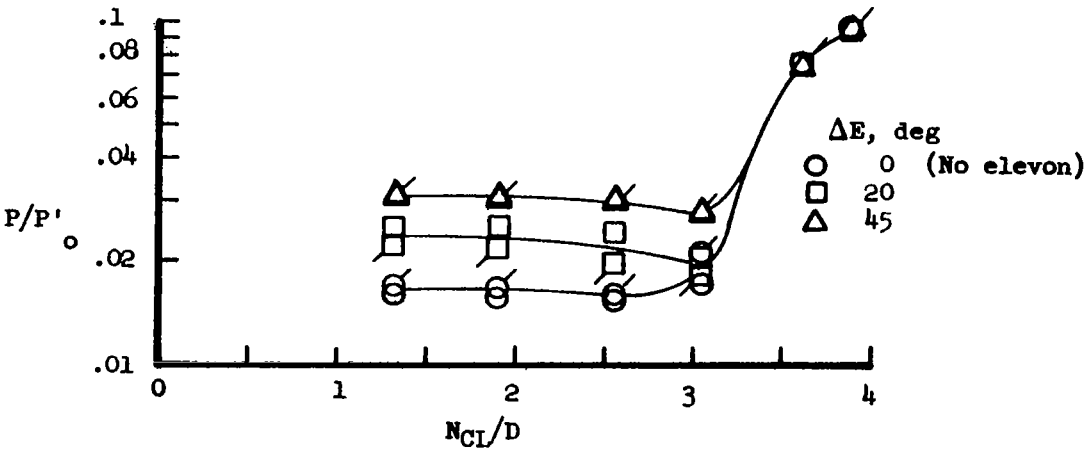

(d) $\alpha = 0°$, $x_{CL}/D = 12.26$

Figure 18.- Continued.

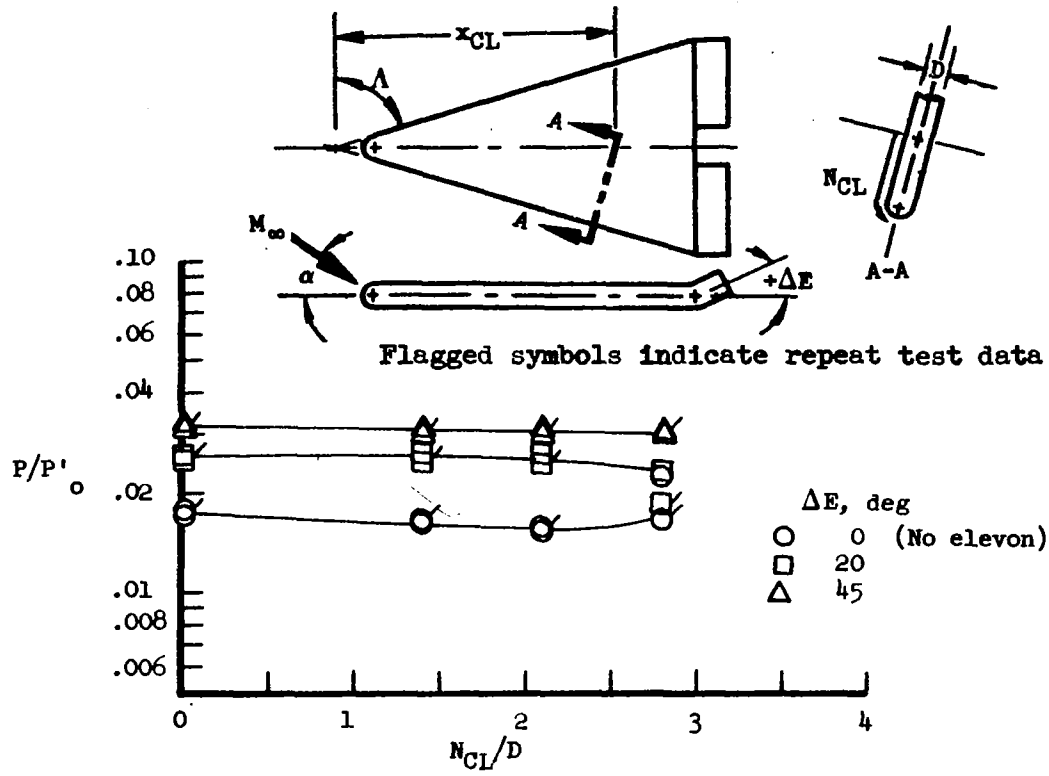

(e) $\alpha = 0°$, $x_{CL}/D = 13.44$

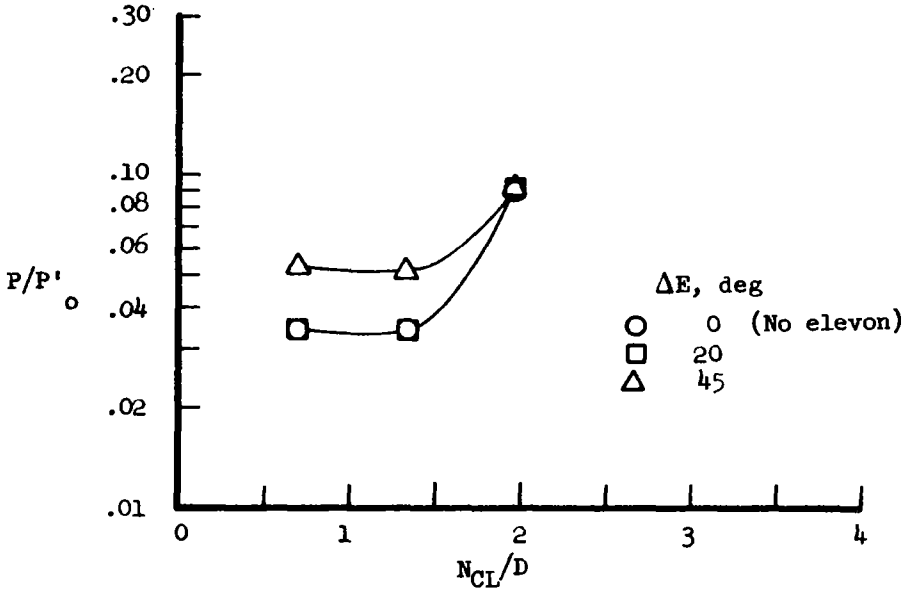

(f) $\alpha = 5°$, $x_{CL}/D = 6.38$

Figure 18.- Continued.

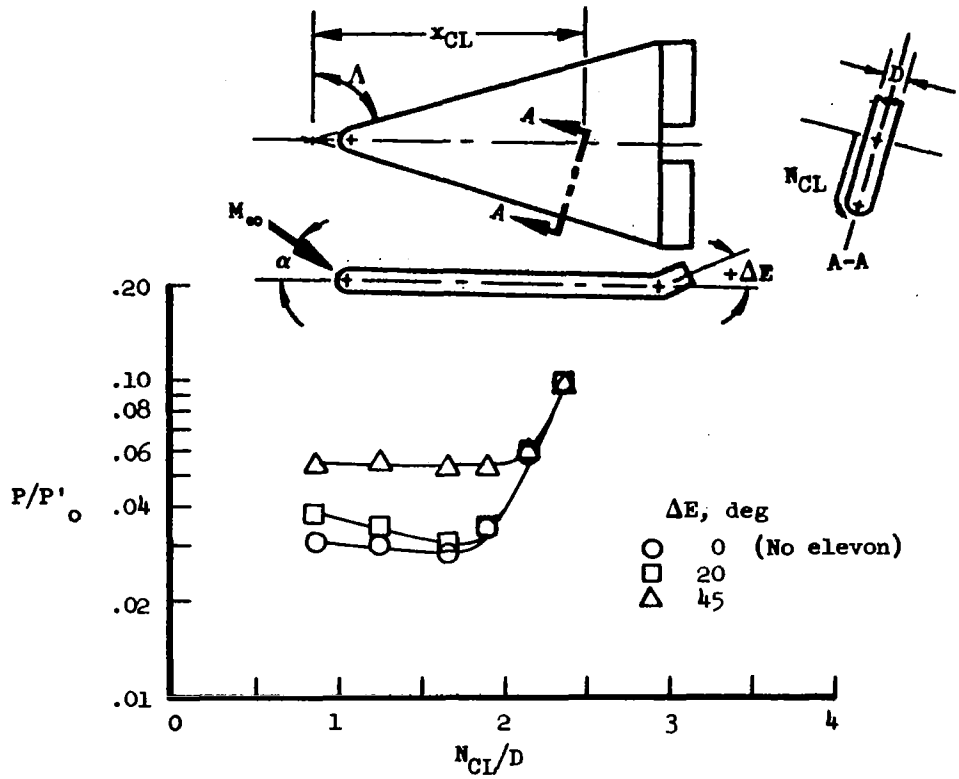

(g) $\alpha = 5°$, $x_{CL}/D = 7.85$

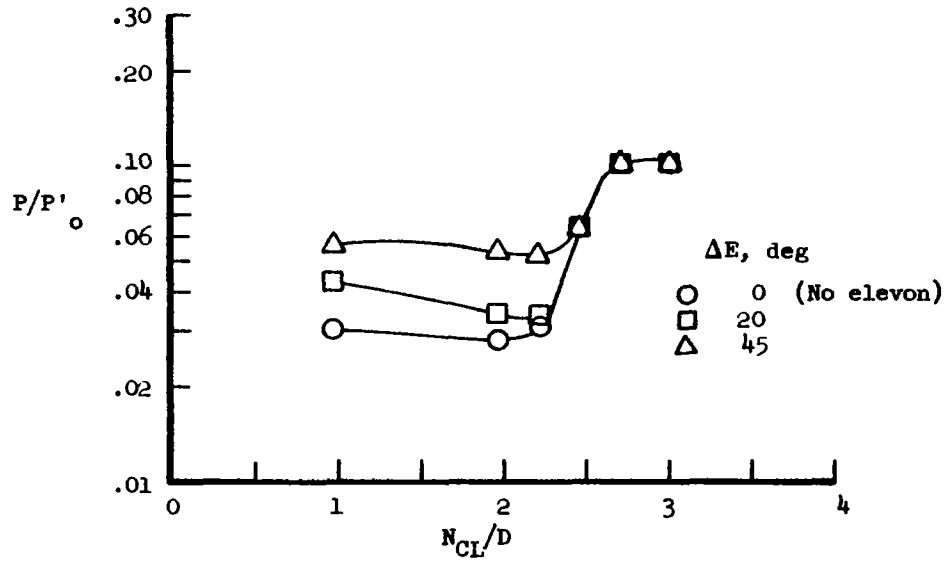

(h) $\alpha = 5°$, $x_{CL}/D = 9.32$

Figure 18.- Continued.

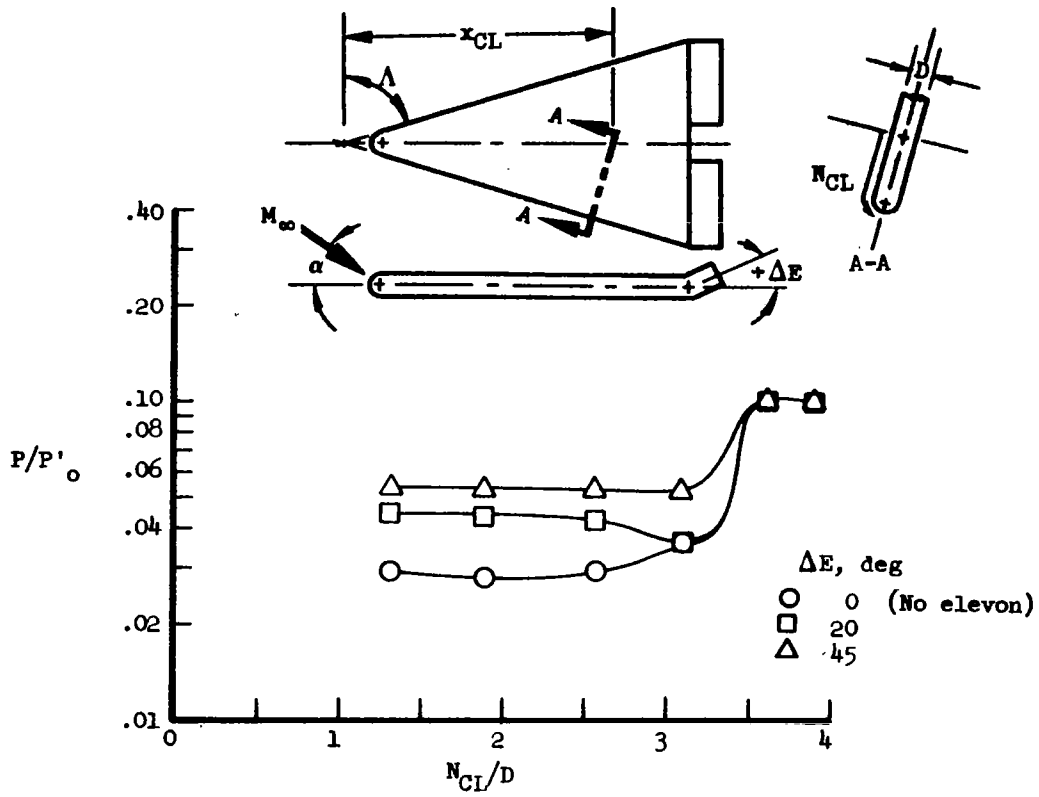

(i) $\alpha = 5°$, $x_{CL}/D = 12.26$

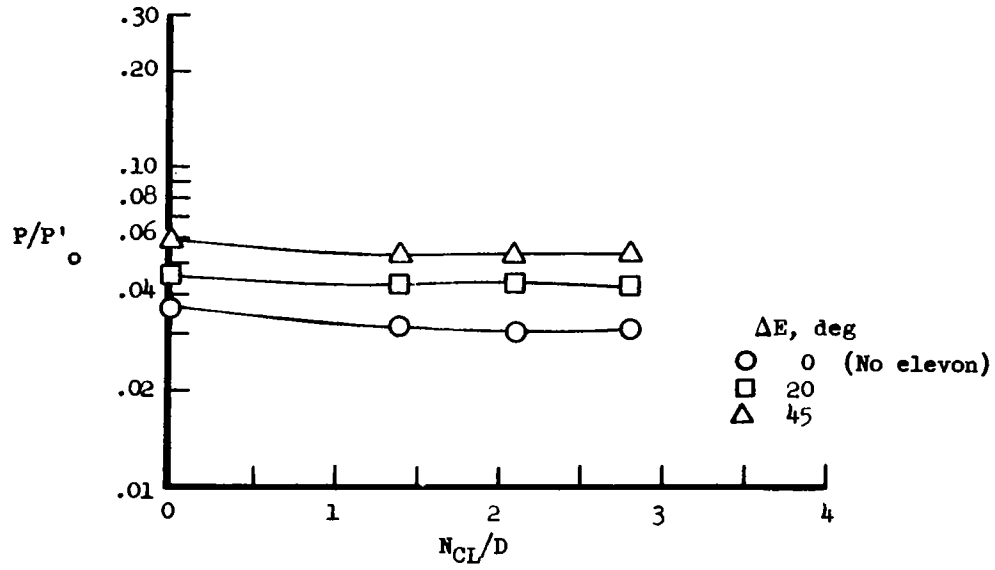

(j) $\alpha = 5°$, $x_{CL}/D = 13.44$

Figure 18.- Continued.

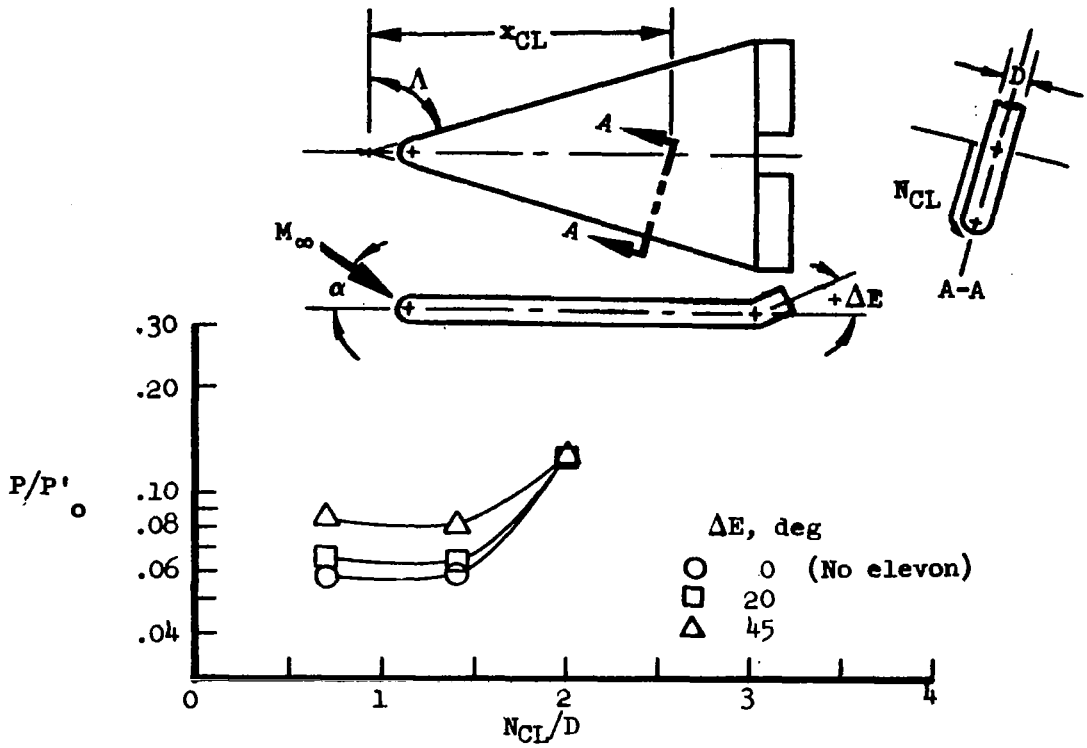

(k) $\alpha = 10°$, $x_{CL}/D = 6.38$

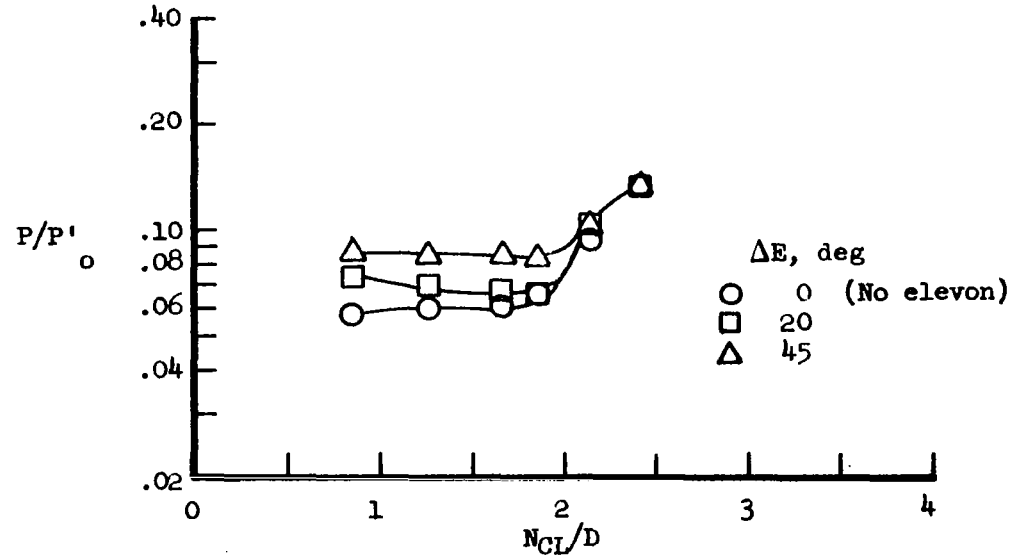

(l) $\alpha = 10°$, $x_{CL}/D = 7.85$

Figure 18.- Continued.

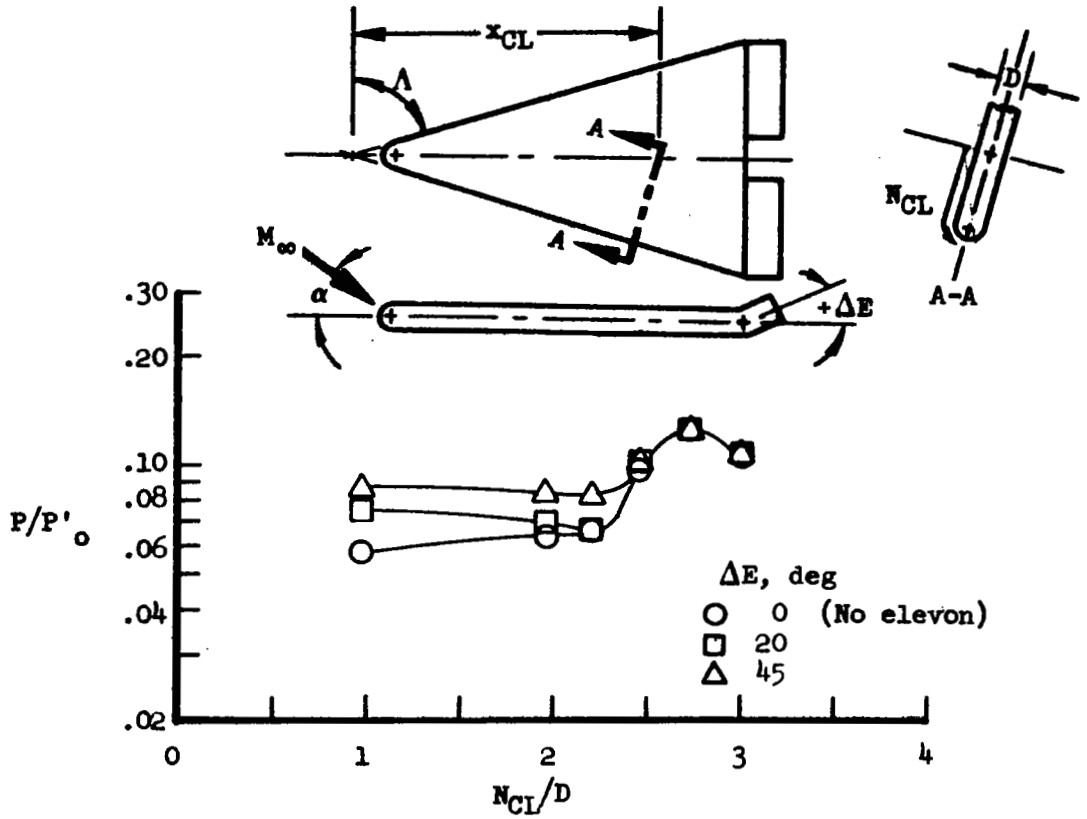

(m) α = 10°, x_{CL}/D = 9.32

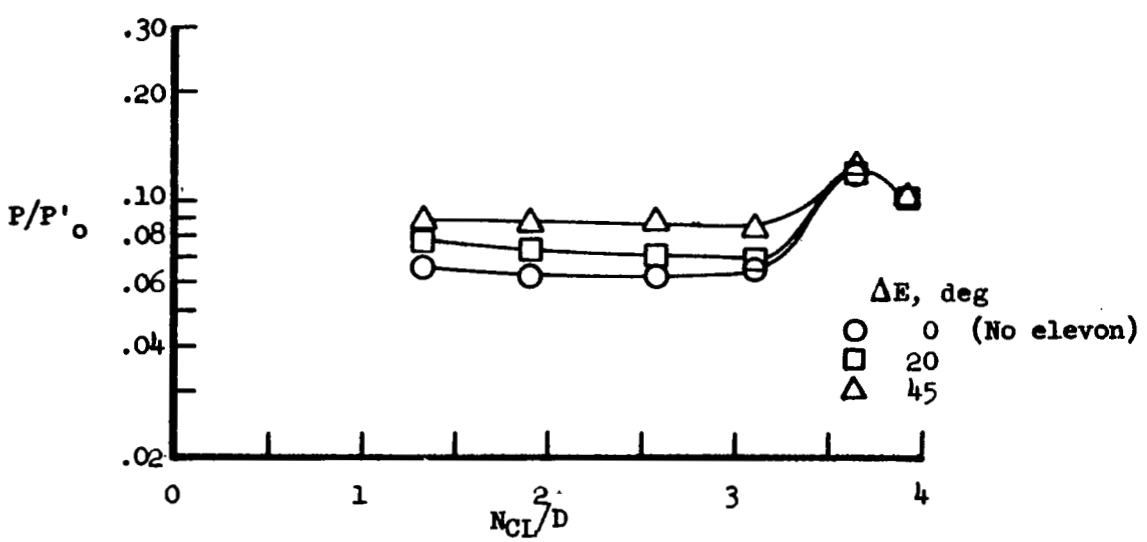

(n) α = 10°, x_{CL}/D = 12.26

Figure 18.- Continued.

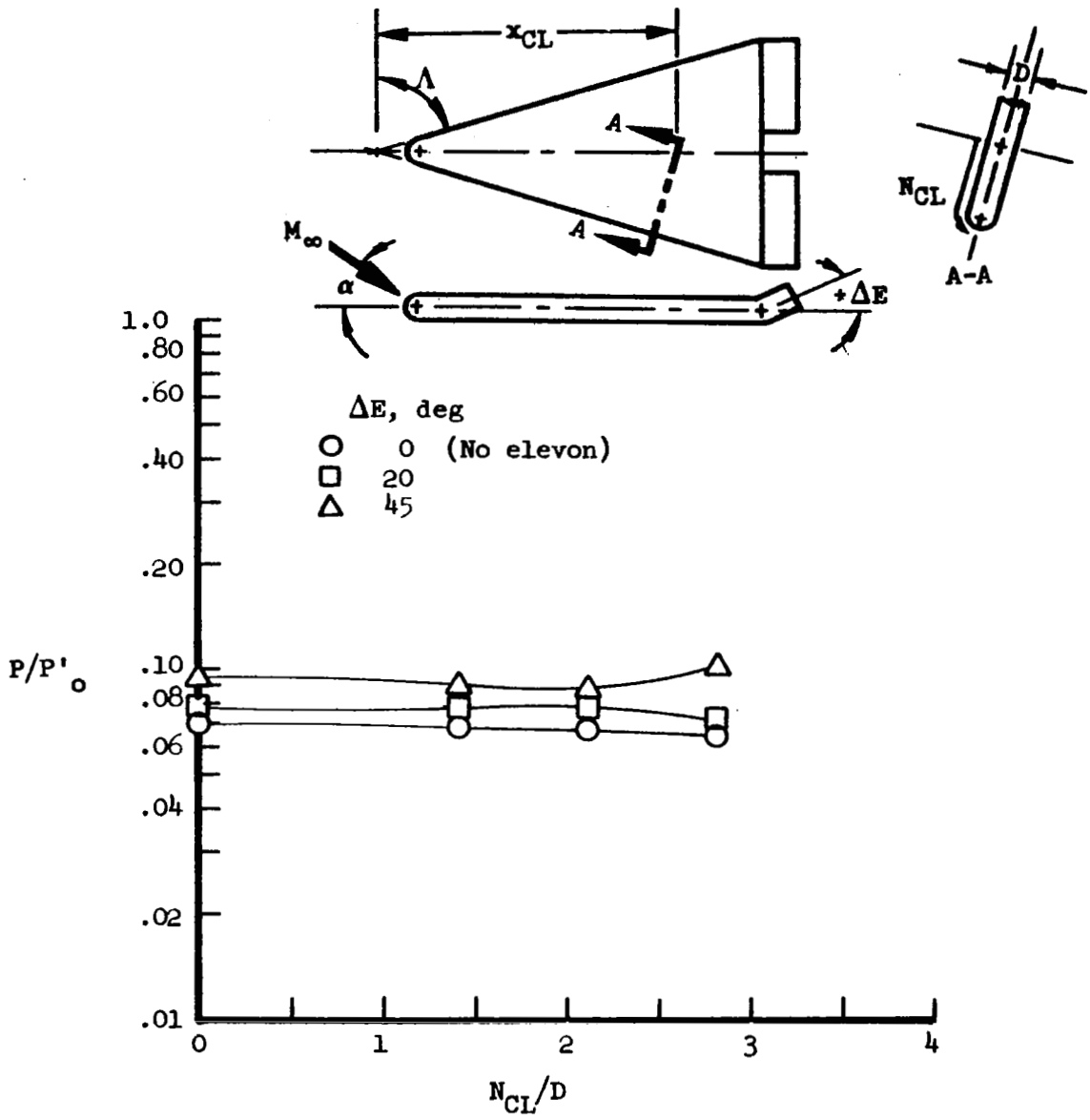

(o) $\alpha = 10°$, $x_{CL}/D = 13.44$

Figure 18.- Concluded.

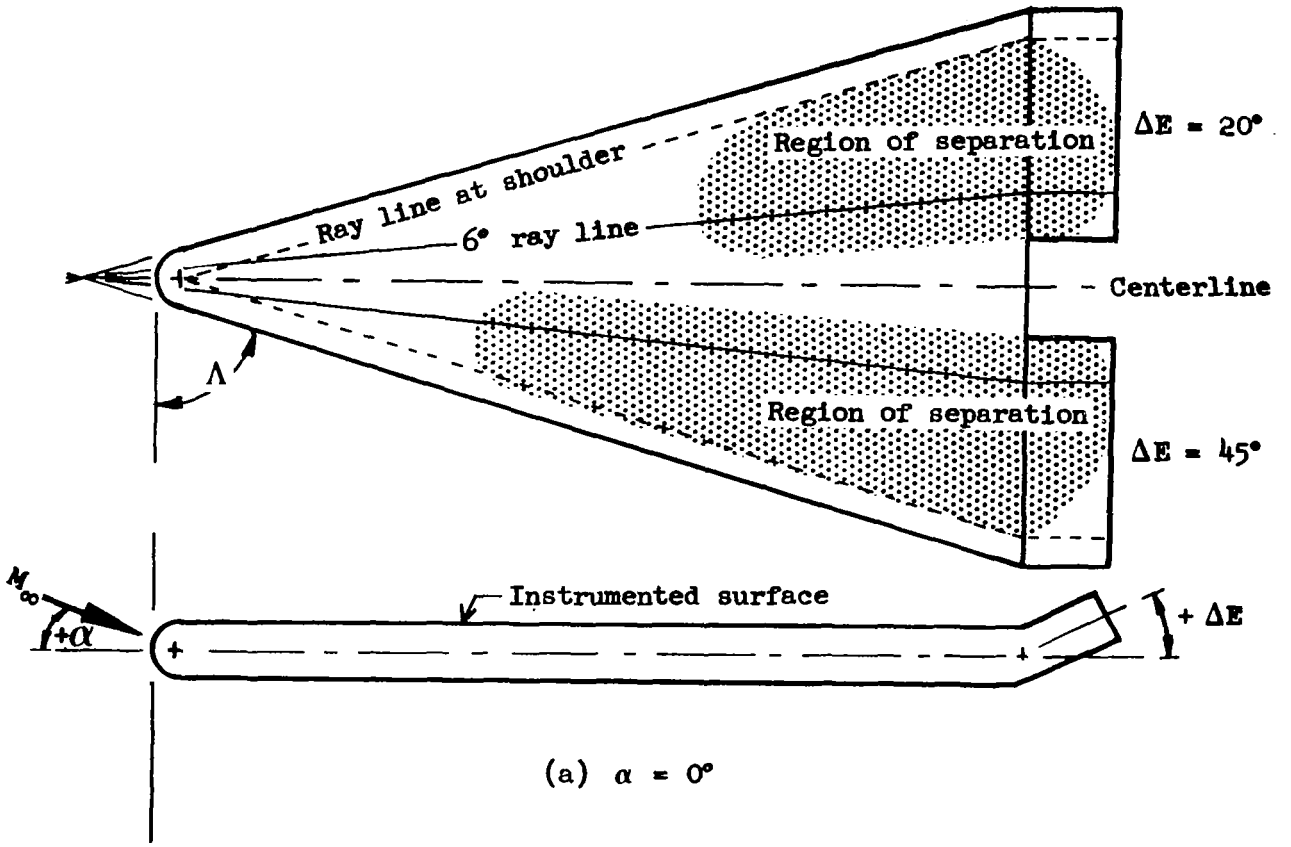

(a) $\alpha = 0°$

Figure 19.- Extent of separation on the lower surface of a blunt delta wing due to elevon deflection.
$M_\infty = 8.08$; $\Lambda = 73°$; $N_{Re,L_r} = 1.202 \times 10^6$;
$P'_o = 1.63$ psia; $H_o = 7.5 \times 10^6$ ft-lb/slug.

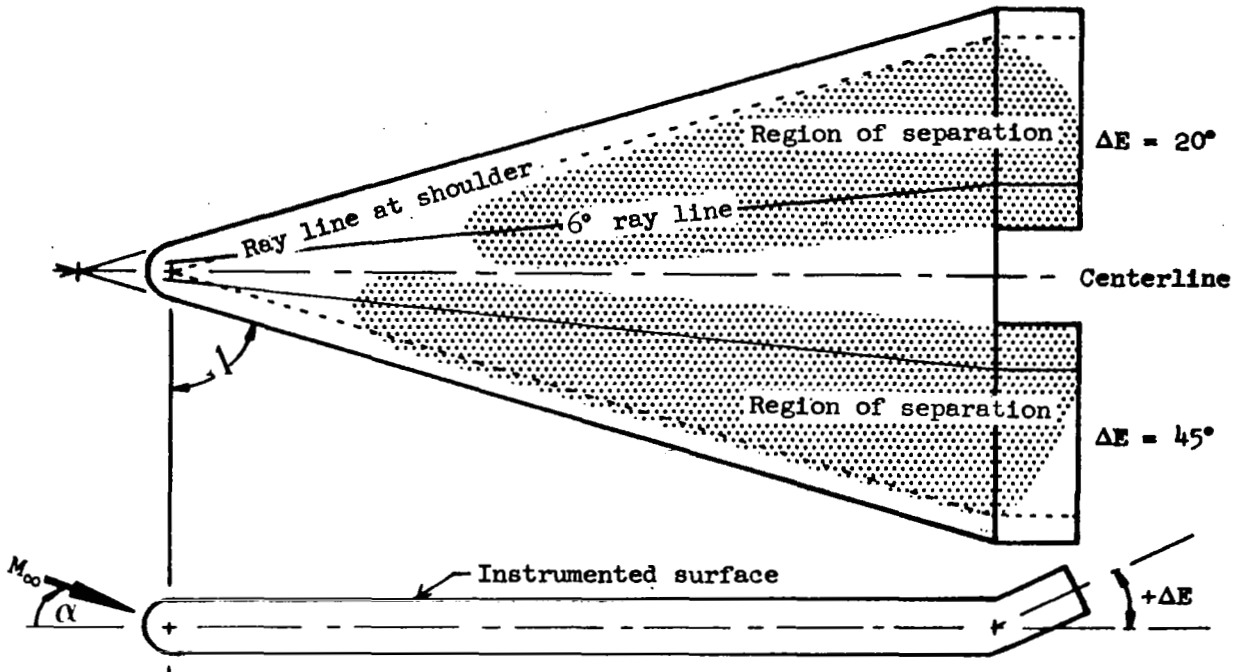

(b) $\alpha = 5°$

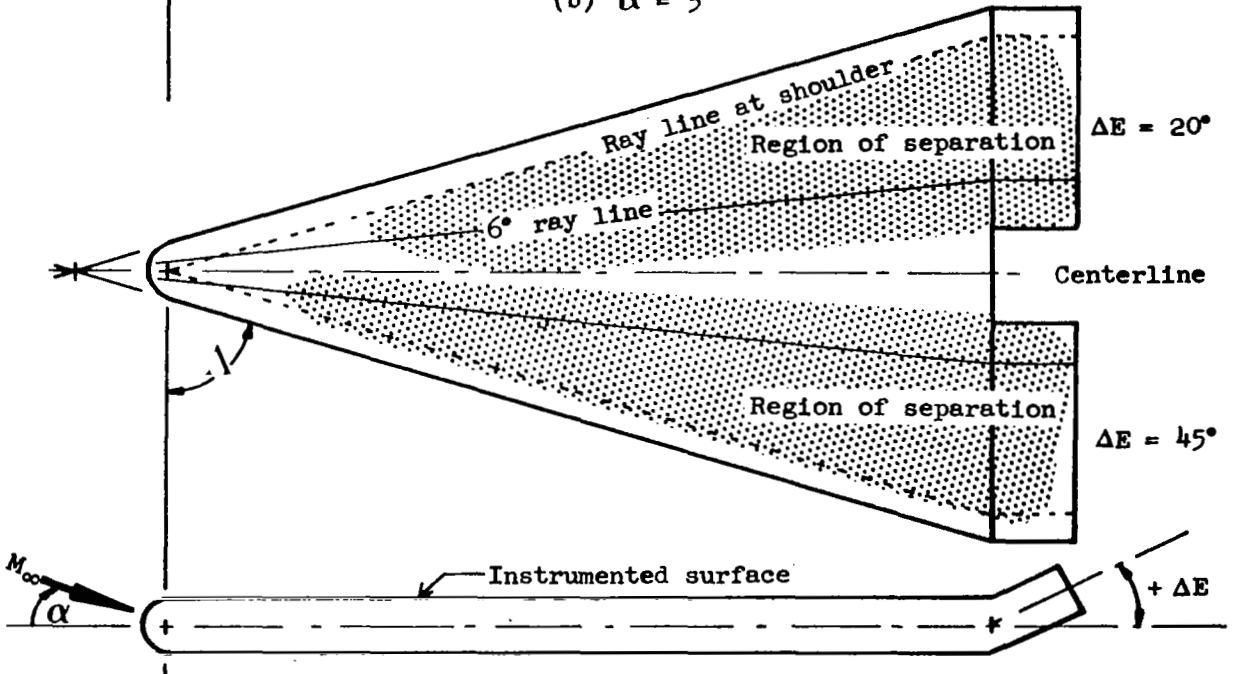

(c) $\alpha = 10°$

Figure 19.- Continued.

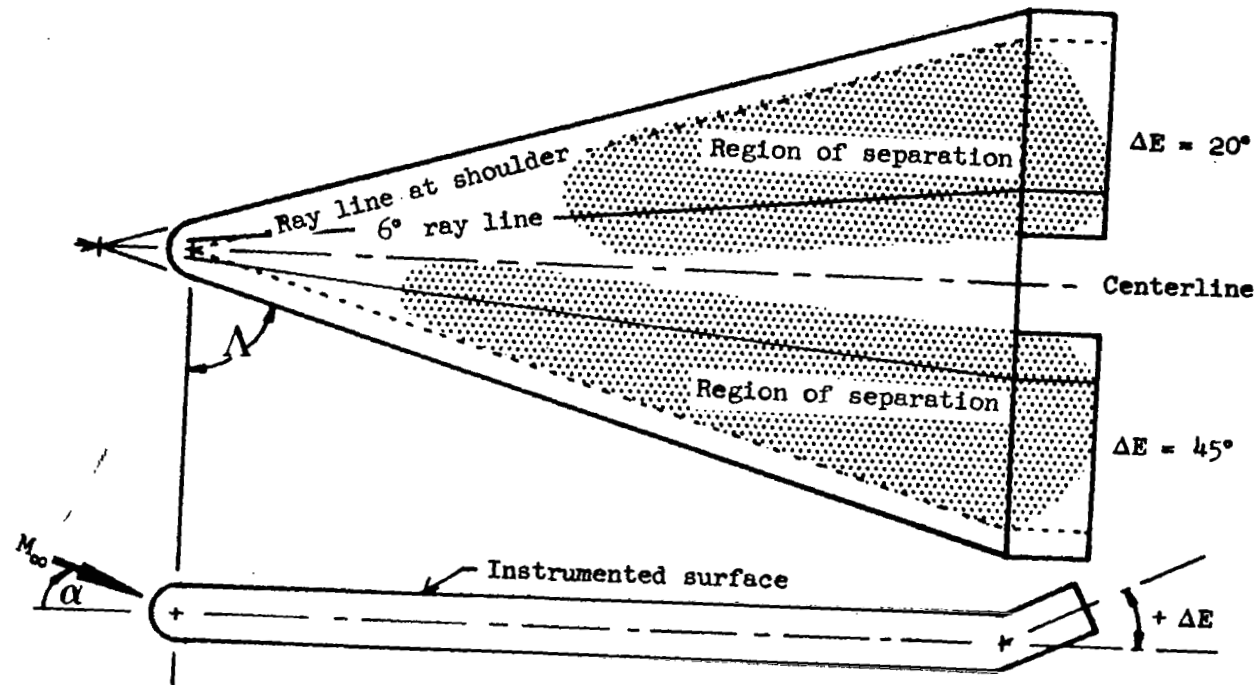

(d) α = 15°

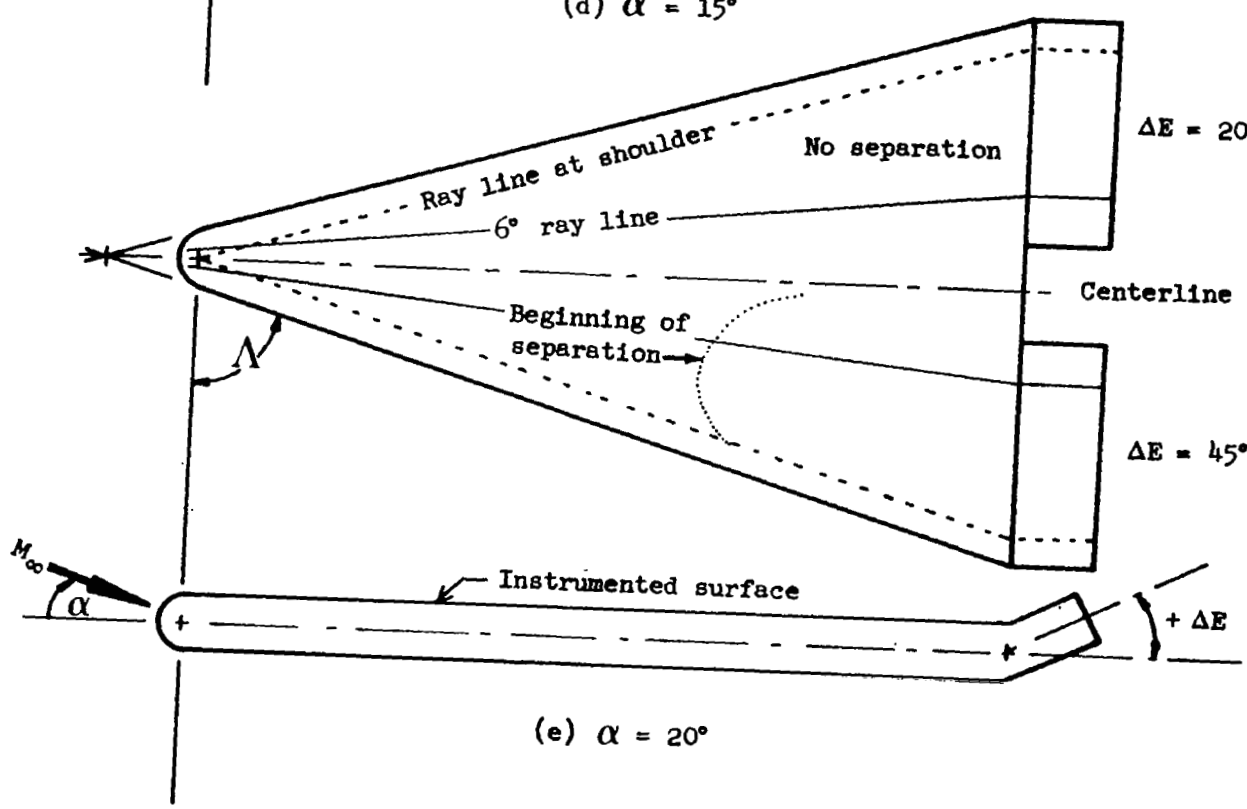

(e) α = 20°

Figure 19.- Continued.

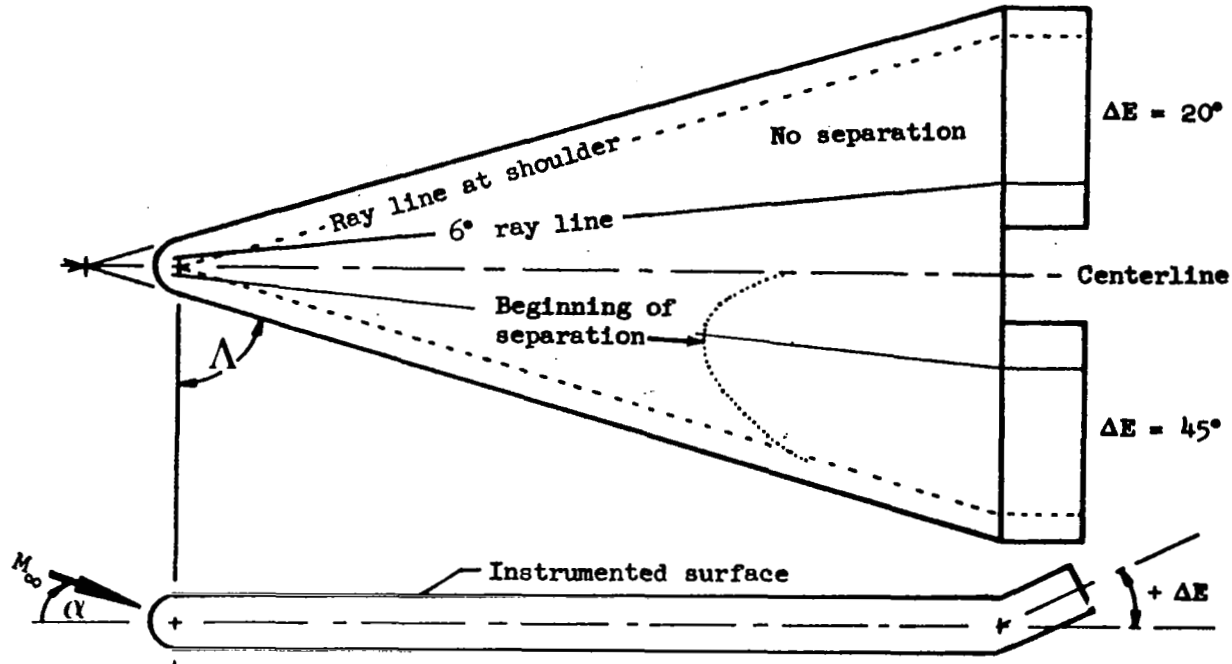

(f) α = 25°

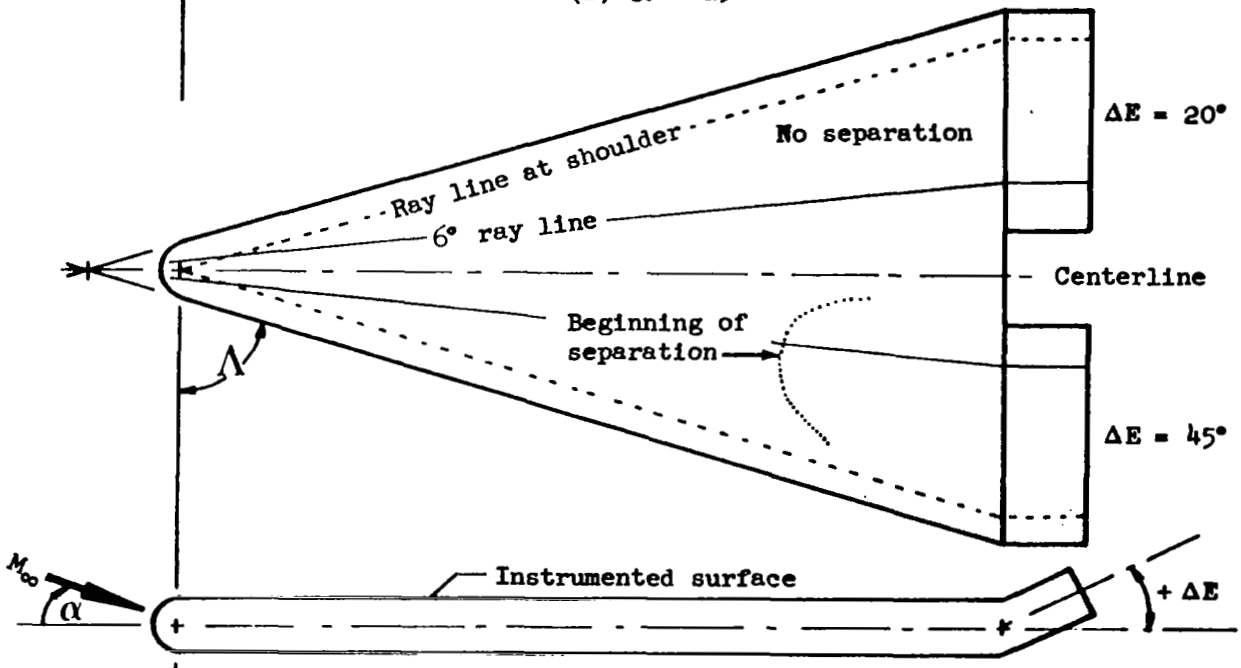

(g) α = 30°

Figure 19.- Concluded.

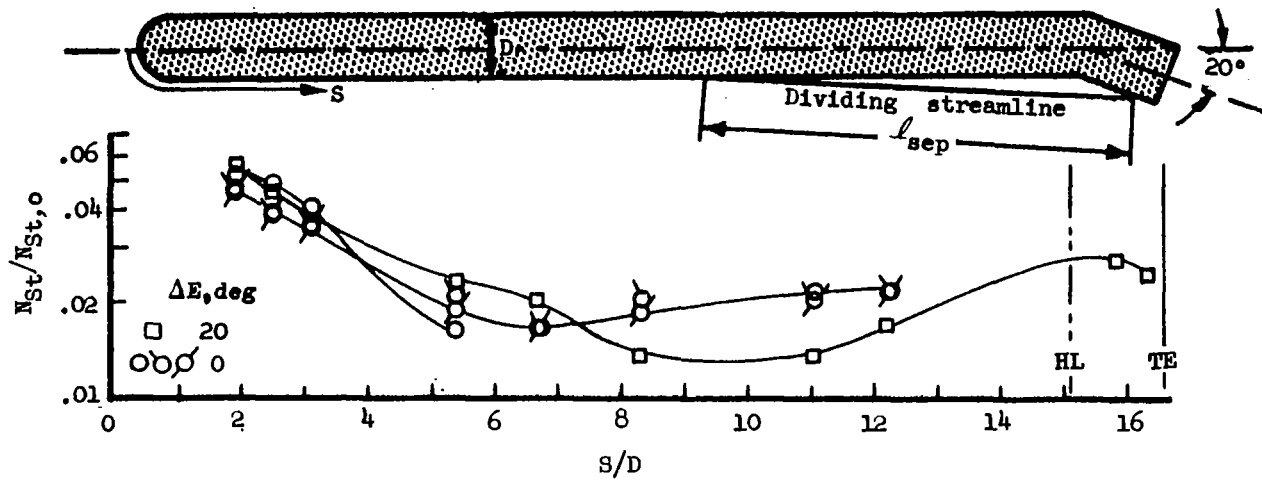

(a) $\alpha = 0°$, $\Delta E = 20°$

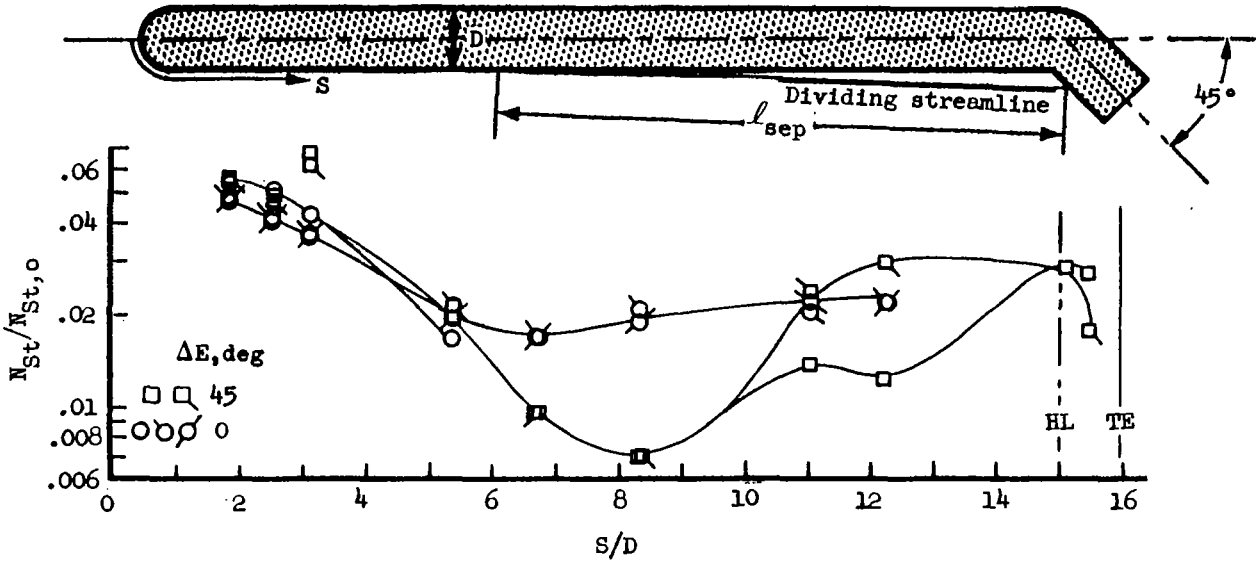

(b) $\alpha = 0°$, $\Delta E = 45°$

Figure 20.- Heating distribution along a 6° ray line on the lower surface of a blunt delta wing with deflected elevons.

$M_\infty = 8.08$; $\Lambda = 73°$; $N_{Re,L_r} = 1.202 \times 10^6$;

$P'_o = 1.63$ psia; $H_o = 7.5 \times 10^6$ ft-lb/slug; $N_{St,o} = .0277$.

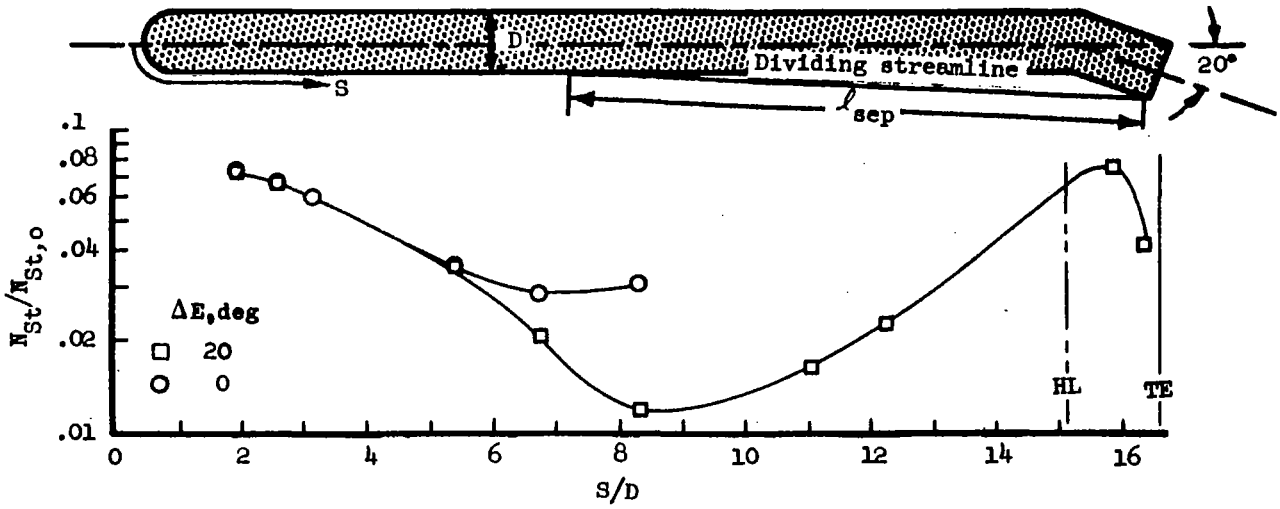

(c) $\alpha = 5°$, $\Delta E = 20°$

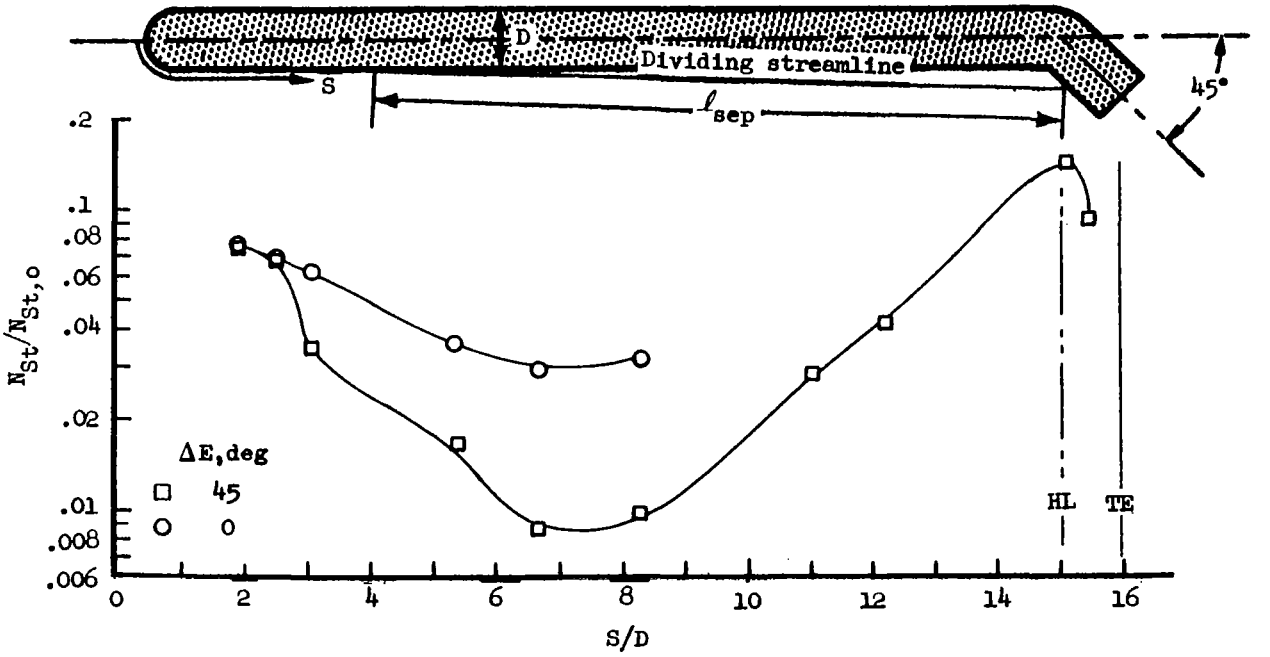

(d) $\alpha = 5°$, $\Delta E = 45°$

Figure 20.- Continued.

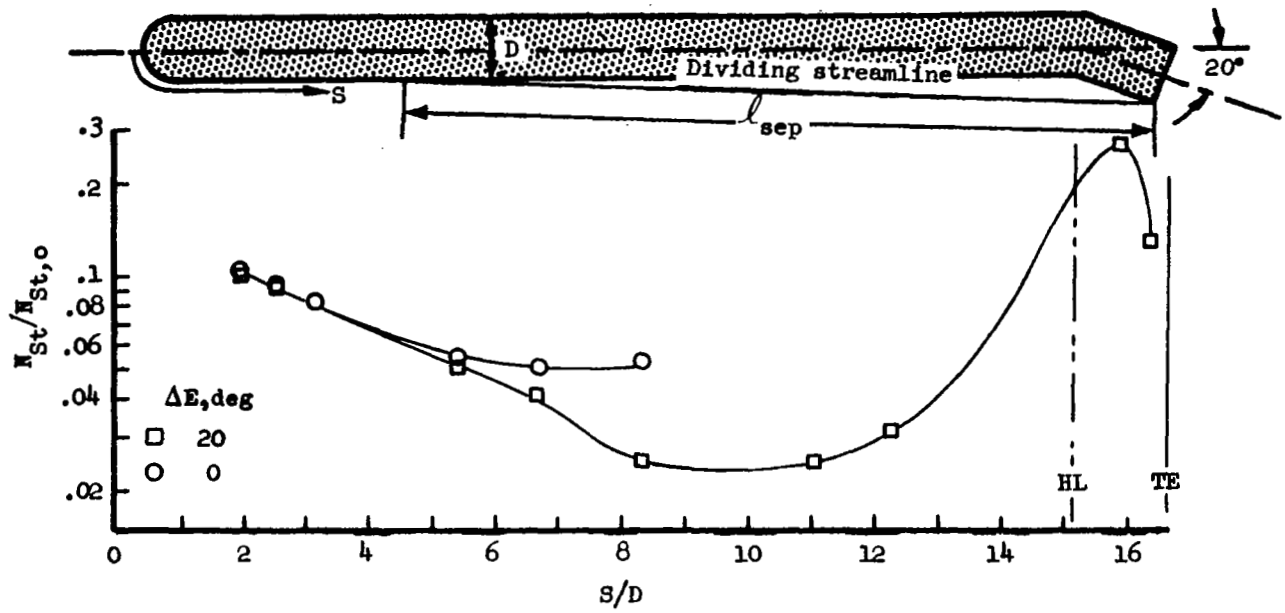

(e) $\alpha = 10°$, $\Delta E = 20°$

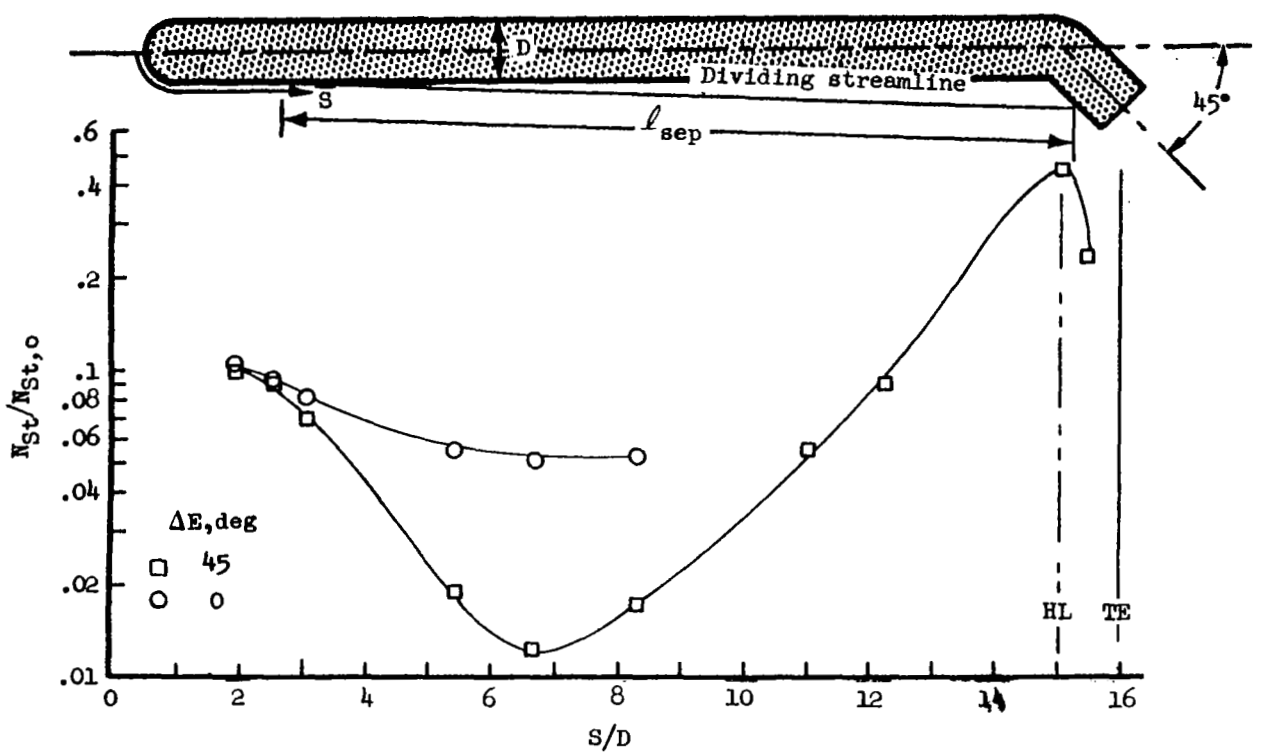

(f) $\alpha = 10°$, $\Delta E = 45°$

Figure 20.- Continued.

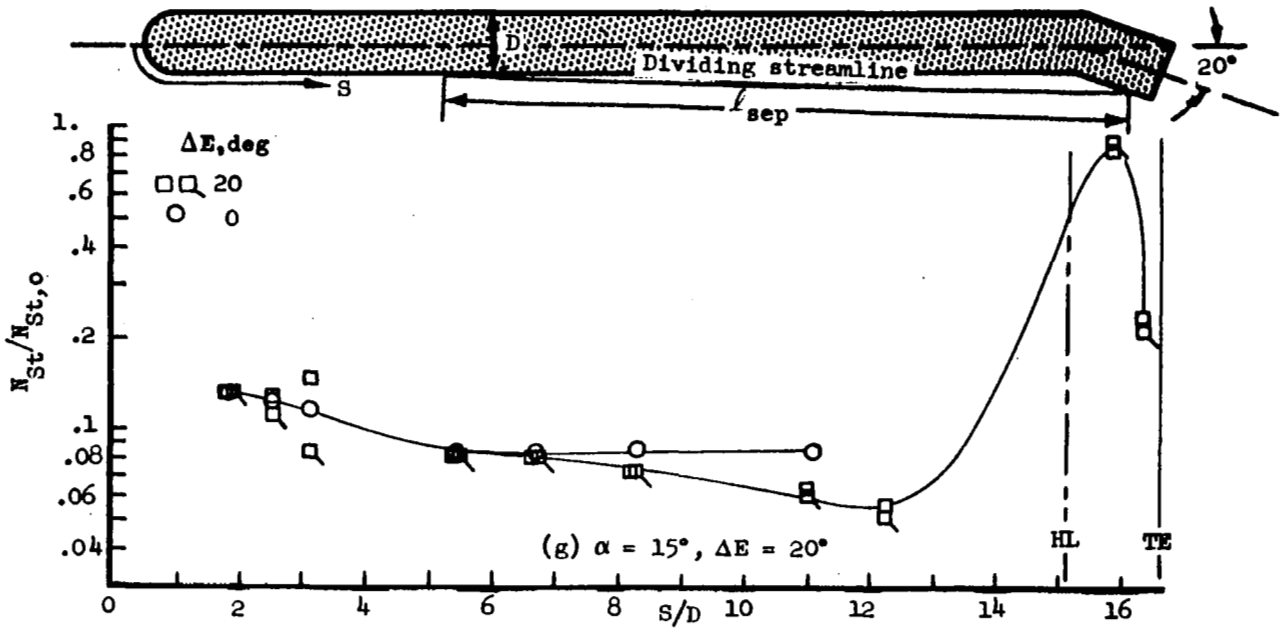

(g) α = 15°, ΔE = 20°

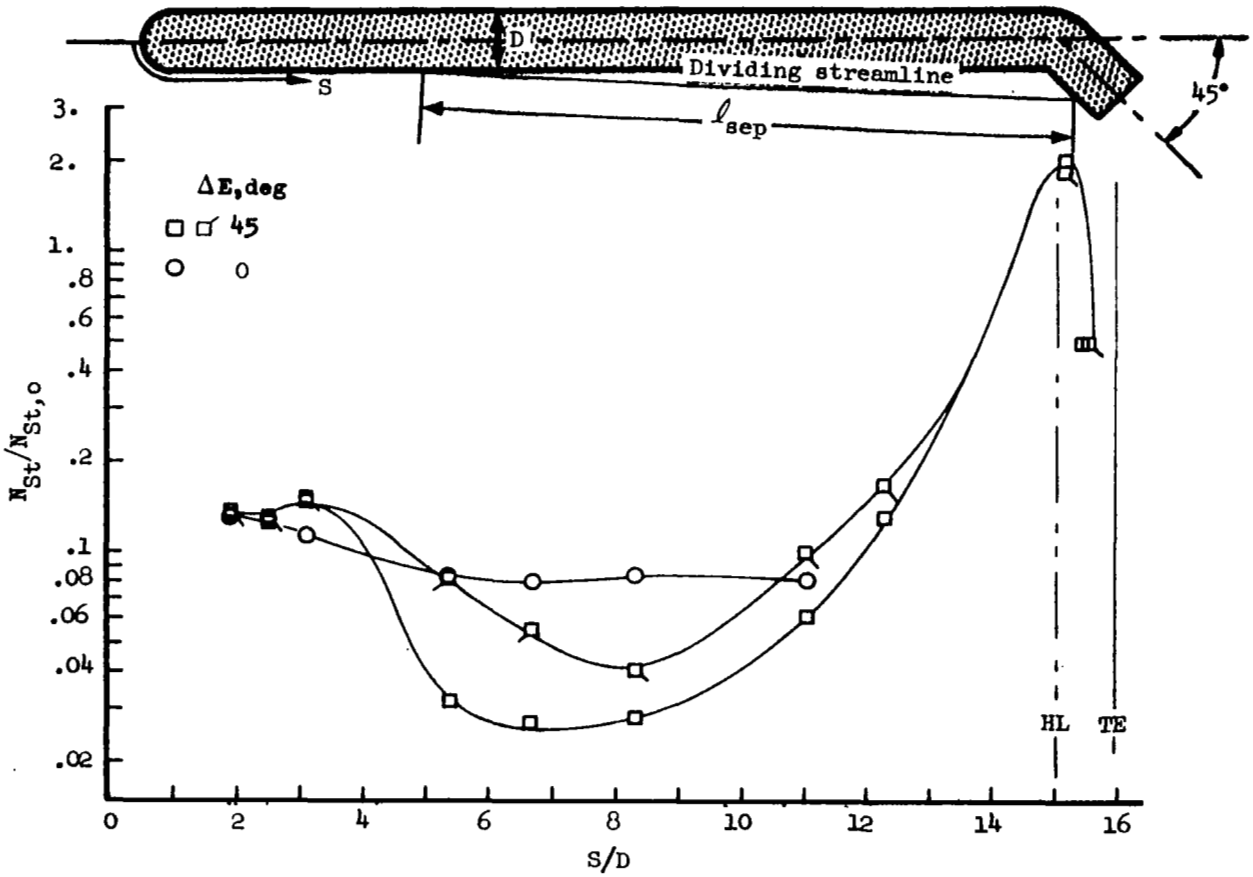

(h) α = 15°, ΔE = 45°

Figure 20.- Continued.

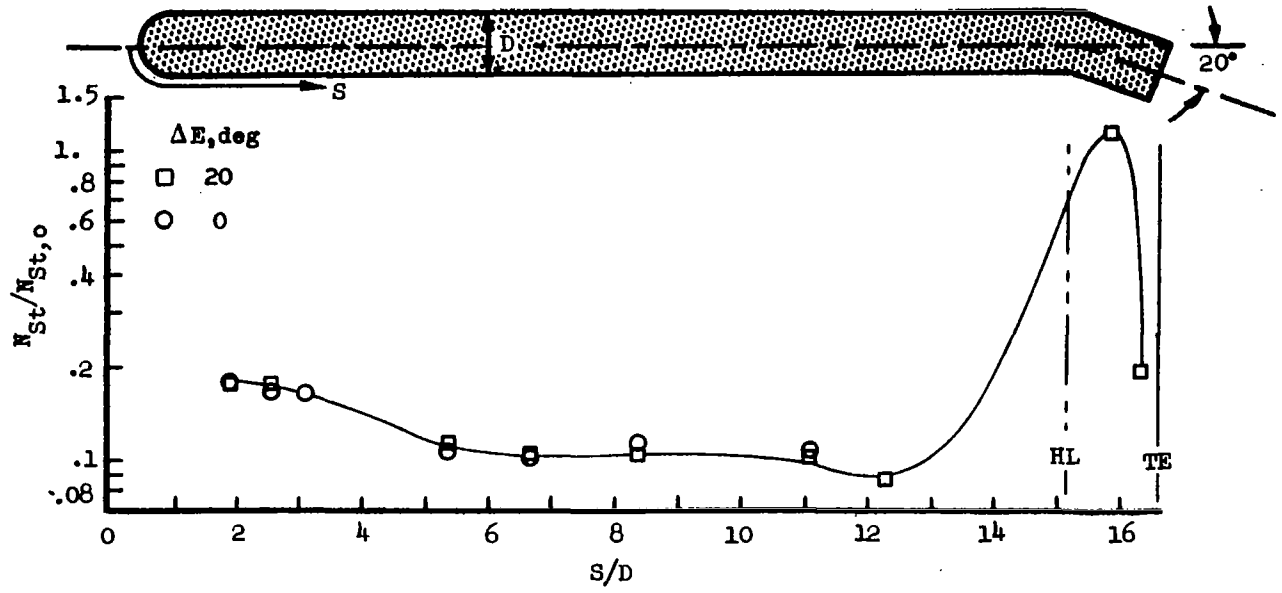

(i) α = 20°, ΔE = 20°

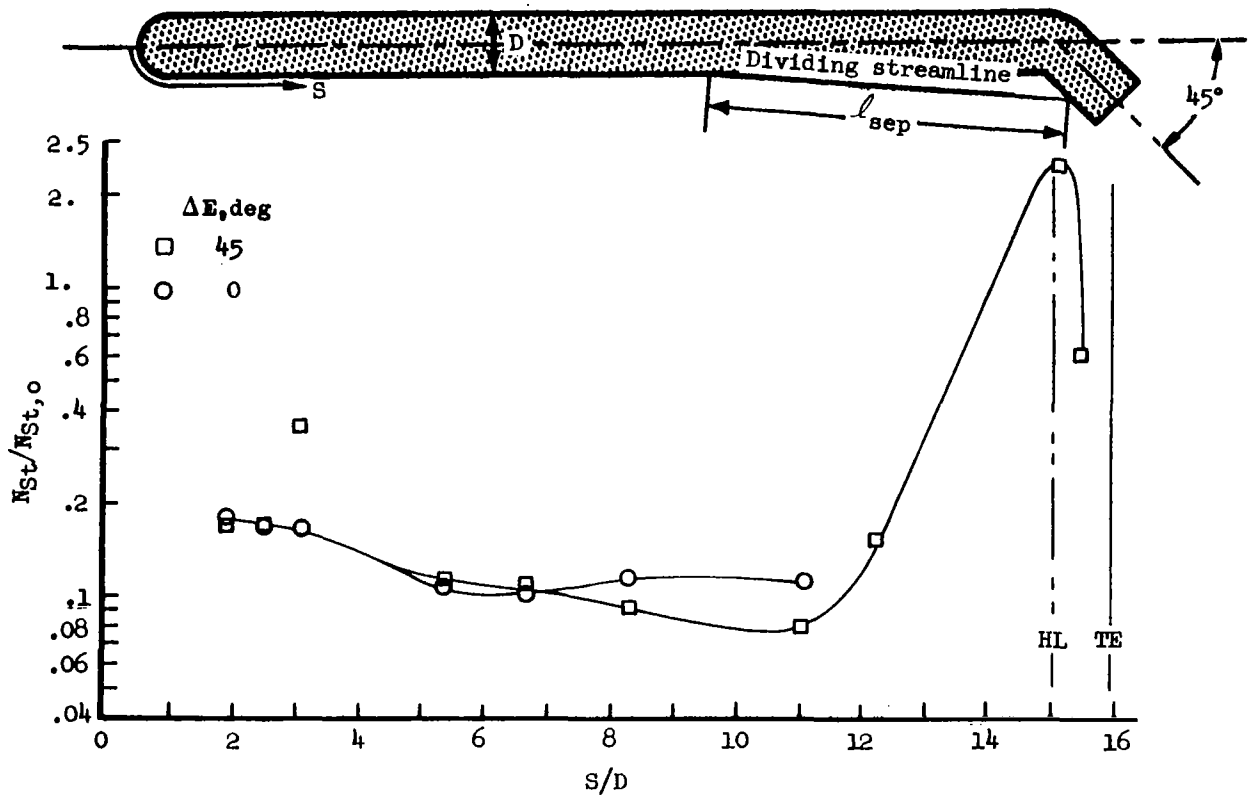

(j) α = 20°, ΔE = 45°

Figure 20.- Continued.

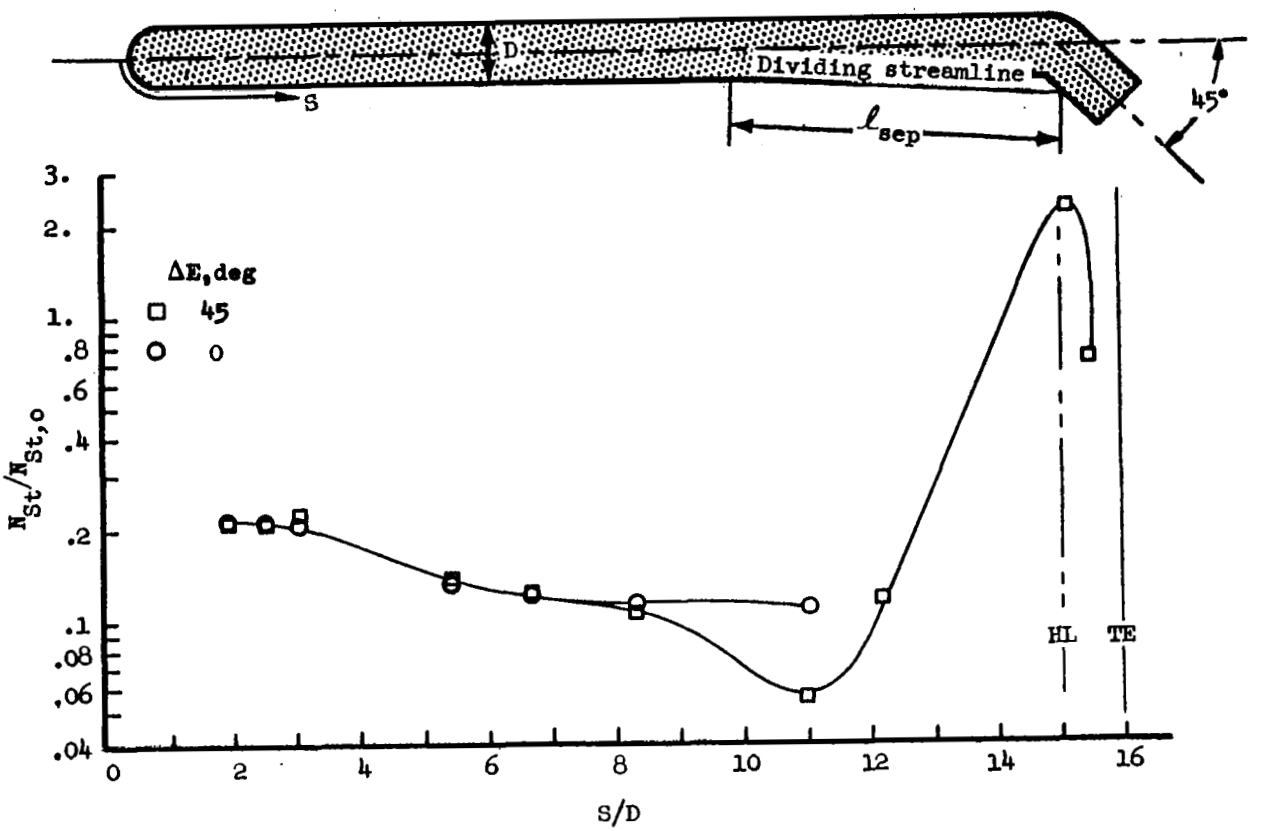

(k) $\alpha = 25°$, $\Delta E = 45°$

Figure 20.- Concluded.

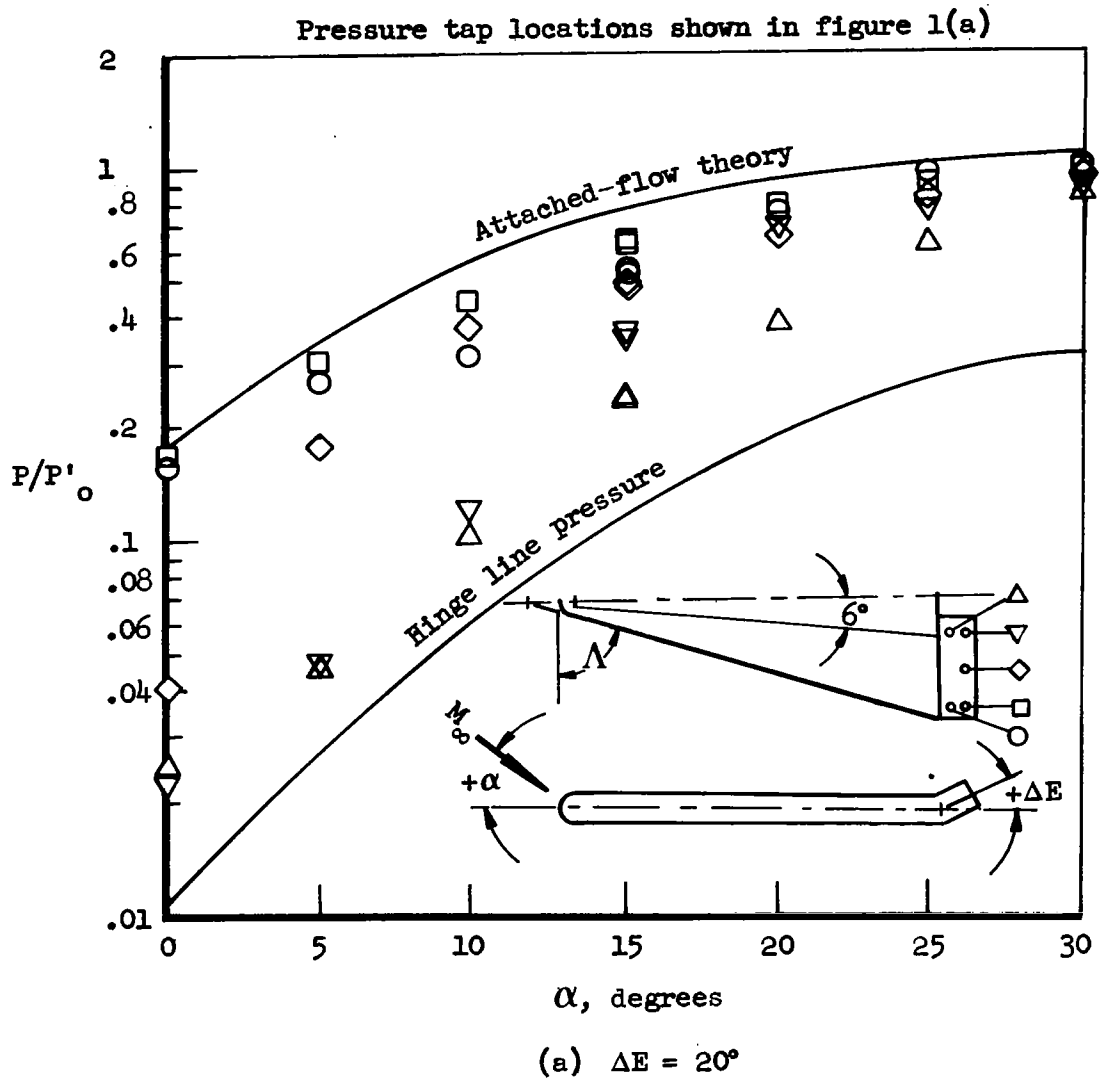

(a) $\Delta E = 20°$

Figure 21.- Pressure distribution on a deflected elevon attached to a blunt delta wing. $M_\infty = 8.08$; $\Lambda = 73°$; $N_{Re,L_r} = 1.202 \times 10^6$; $P'_o = 1.63$ psia; $H_o = 7.5 \times 10^6$ ft-lb/slug.

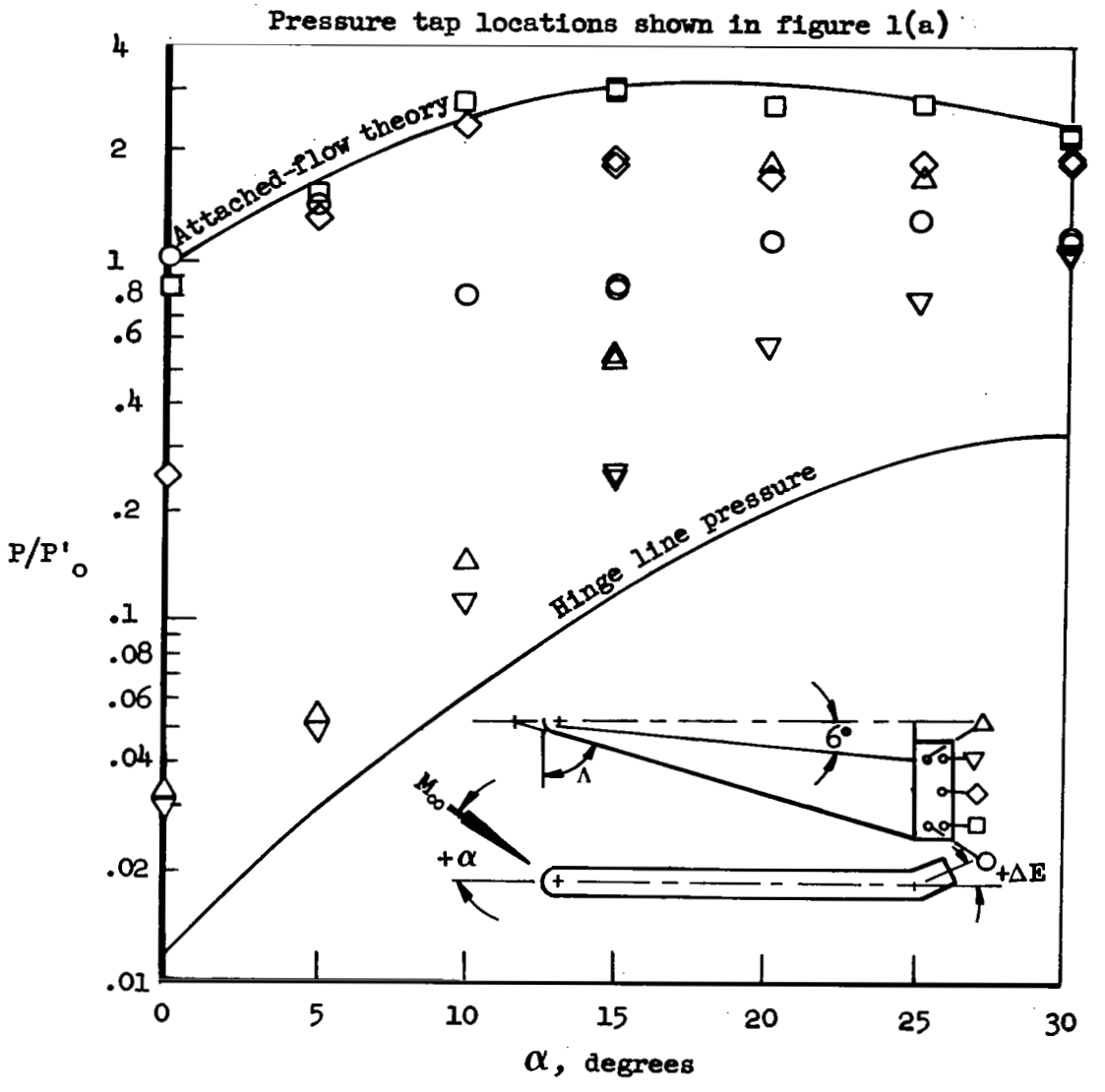

(b) $\Delta E = 45°$

Figure 21.- Concluded.

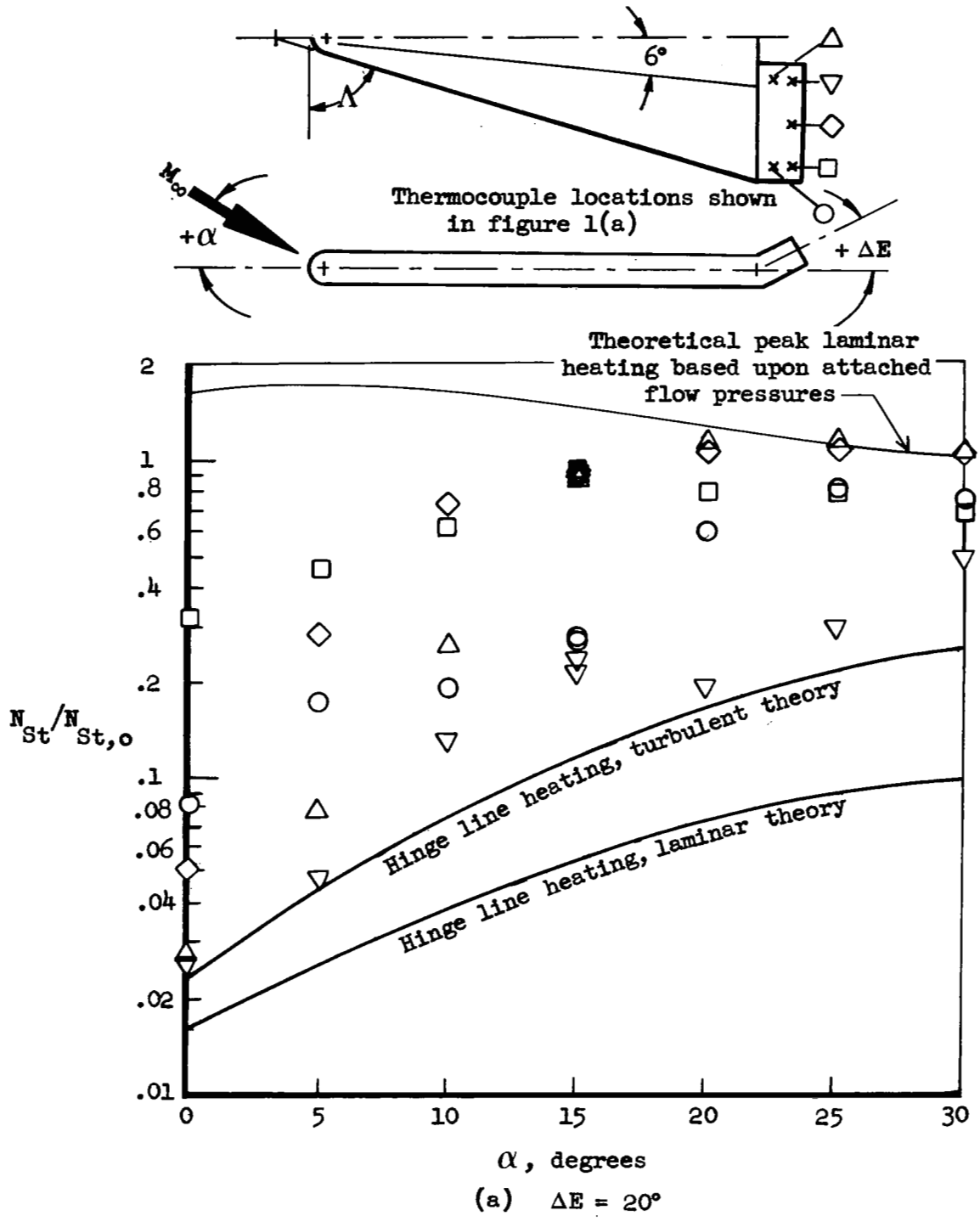

(a) $\Delta E = 20°$

Figure 22.- Heating rate distribution on a deflected elevon attached to a blunt delta wing.

$M_\infty = 8.08$; $\Lambda = 73°$; $N_{Re,L_r} = 1.202 \times 10^6$;

$P'_o = 1.63$ psia; $H_o = 7.5 \times 10^6$ ft-lb/slug.

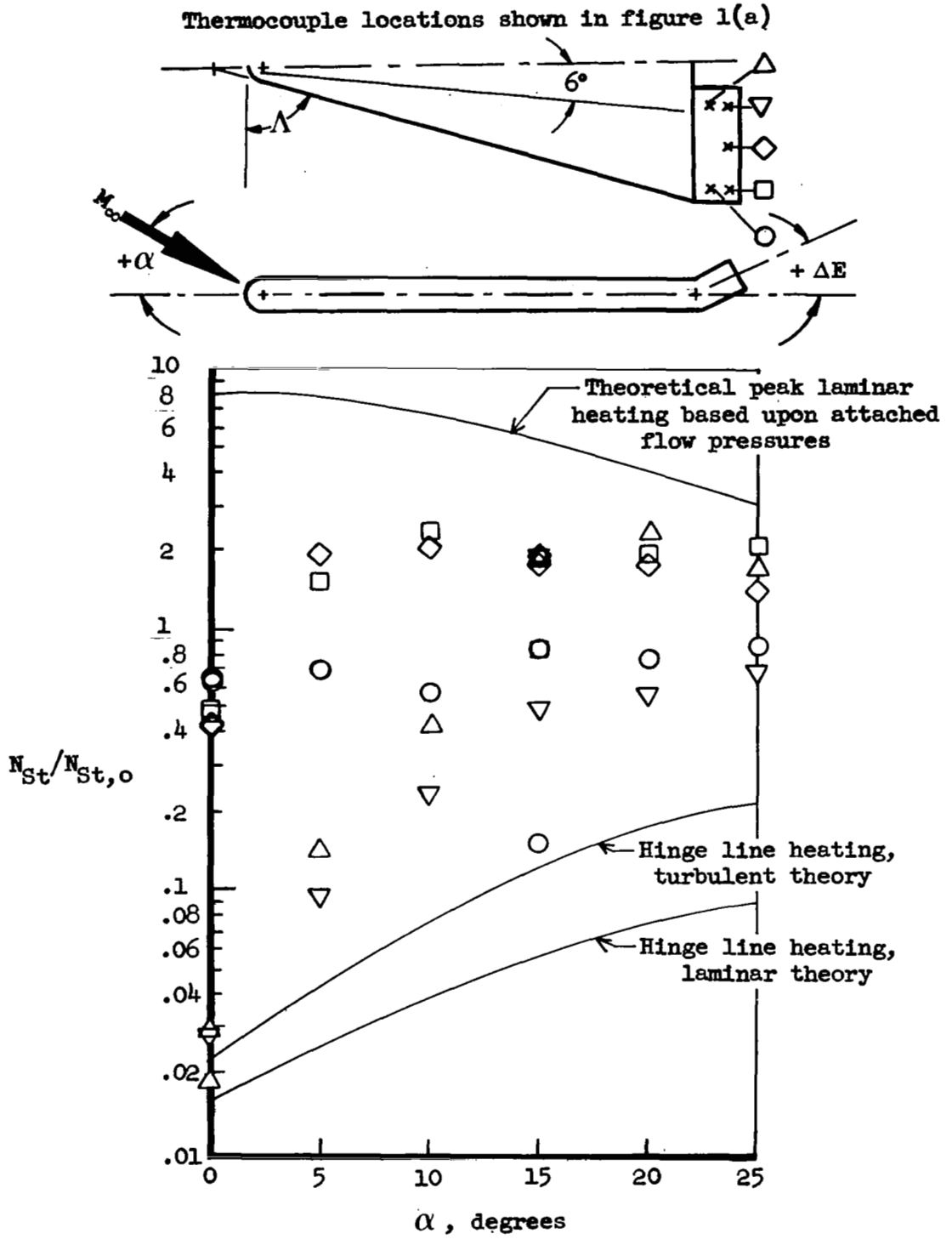

(b) ΔE = 45°

Figure 22.- Concluded.

	Model	M_∞	ΔF, deg	P'_o, psia	H_o, ft-lb/slug	N_{Re,L_r}	T_w/T_o
◁	Wing	8.08	45	1.63	7.5×10^6	1.2×10^6	.4
▽	Wing	8.08	20	1.63	7.5	1.2	.4
■	Plate (transitional data)	6.38	45	88.7	13.7	13.8	.24
□	Plate	15.15	45	.424	27.1	.112	.12
◇	Plate	15.15	30	.424	27.1	.112	.12
◁	Extended span	15.15	45	.424	27.1	.112	.12

——————— Laminar theory at $C_w \equiv 1$, Hakkinen et. al. (ref. 24)
—— —— —— Turbulent theory, Erdos and Pallone (ref. 15)*
—— - —— - — Laminar theory at $C_w \equiv 1$, Chapman (ref. 10)
— — — — — — Turbulent theory, Sterrett et. al. (ref. 23)*

*Assumes origin of turbulent flow at leading edge

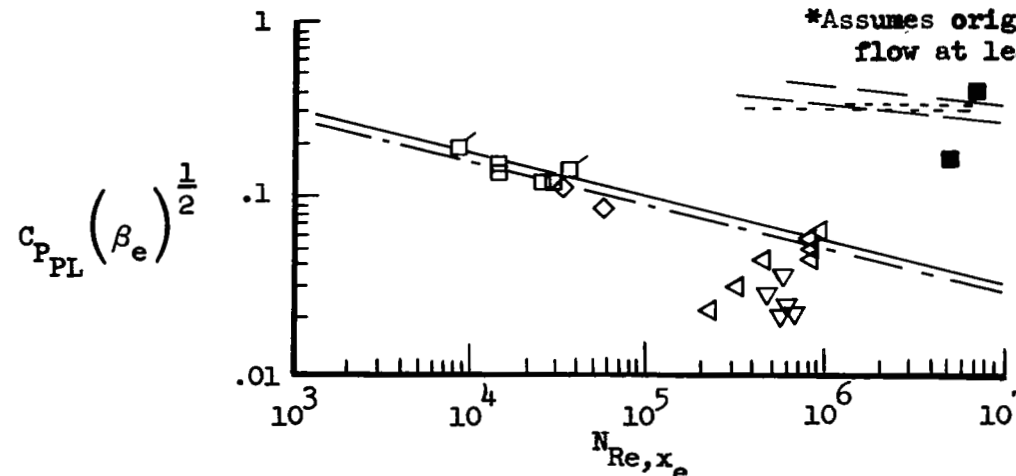

(a) Comparison with sharp flat plate theory

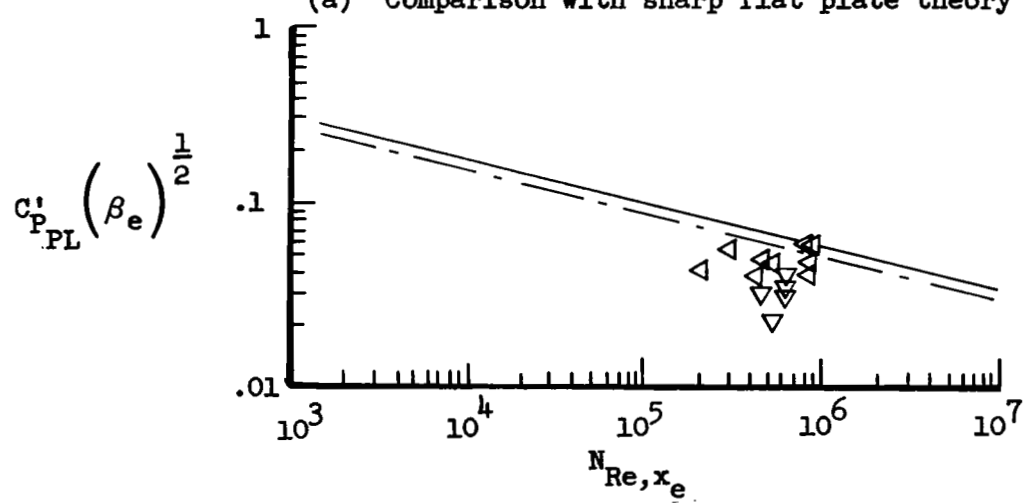

(b) Blunt delta wing plateau pressure coefficients adjusted to remove bluntness induced pressure effect

Figure 23.- Plateau pressure correlation with Reynolds number.

Model	M_∞	ΔF, deg	P'_o, psia	H_o, ft-lb/slug	N_{Re,L_r}	T_w/T_o
◁ Delta wing	8.08	45	1.63	7.5×10^6	1.2×10^6	.4
▽ Delta wing	8.08	20	1.63	7.5×10^6	1.2×10^6	.4
□ Flat Plate	15.15	45	.424	27.1×10^6	$.112 \times 10^6$	.12
◇ Flat Plate	15.15	30	.424	27.1×10^6	$.112 \times 10^6$	.12
□ Flat Plate (extended span)	15.15	45	.424	27.1×10^6	$.112 \times 10^6$	.12

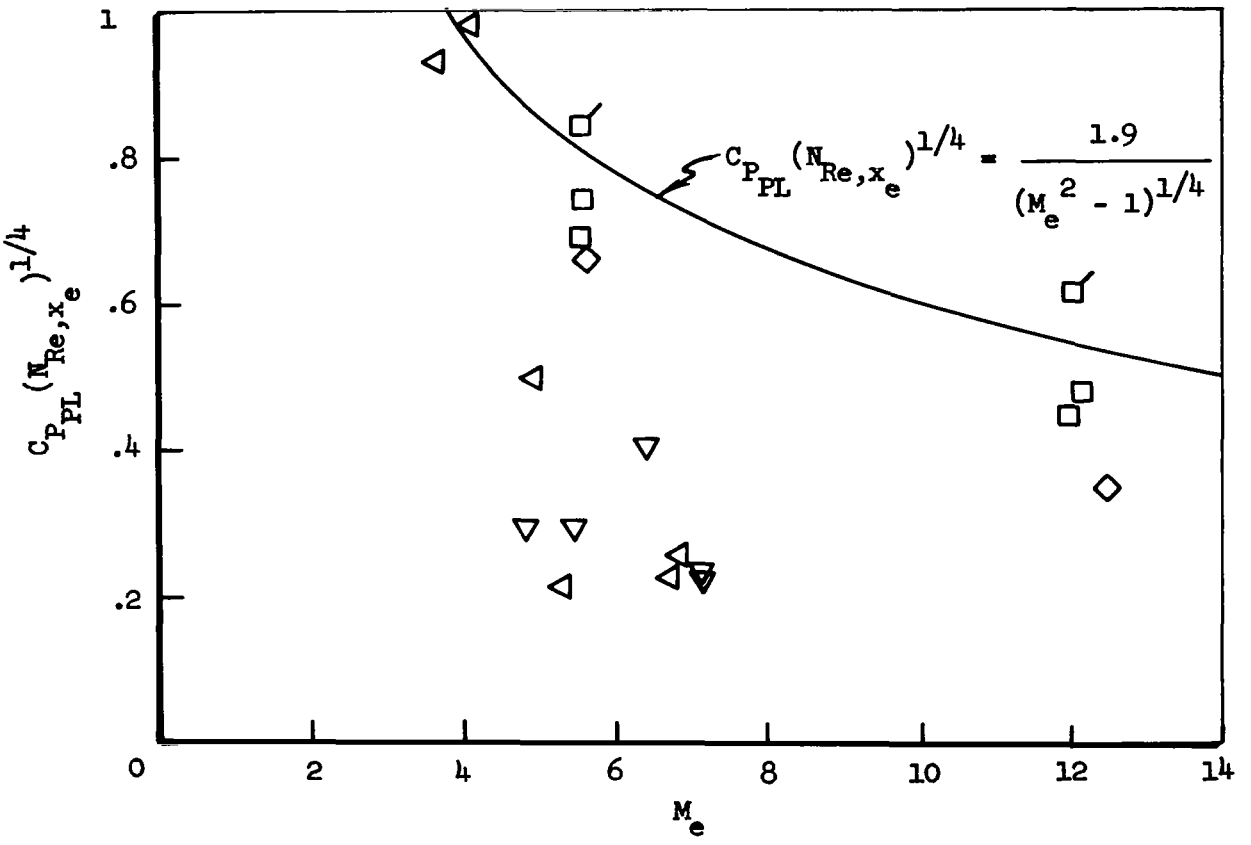

Figure 24.- Plateau pressure correlation with Mach number.

	Model	Reference	M_e	ΔF, deg	N_{Re,L_r}	L_r, ft
◇	-	(24)Hakkinen	2	-	1.8×10^6	1
○	Plate	(26)Pate	3	var.	.375	.92
△	Plate	(26)Pate	3	var.	1.045	.92
◺	Plate	(25)Putnam	9.5-10	var.	1.26	.83
▽	Wing	X-20	5-7	20	1.202	1.22
◁	Wing	X-20	3.5-7	45	1.202	1.22
◇	Plate	X-20	5.5-12	45	.112	1
□	Plate	X-20	5.5-6	15-45	.112	1
◇	Plate	X-20	12-12.5	30-45	.112	1
◆	Plate	X-20	6-7	45	14.04	1
◆	Plate	X-20	4-5	45	14.04	1

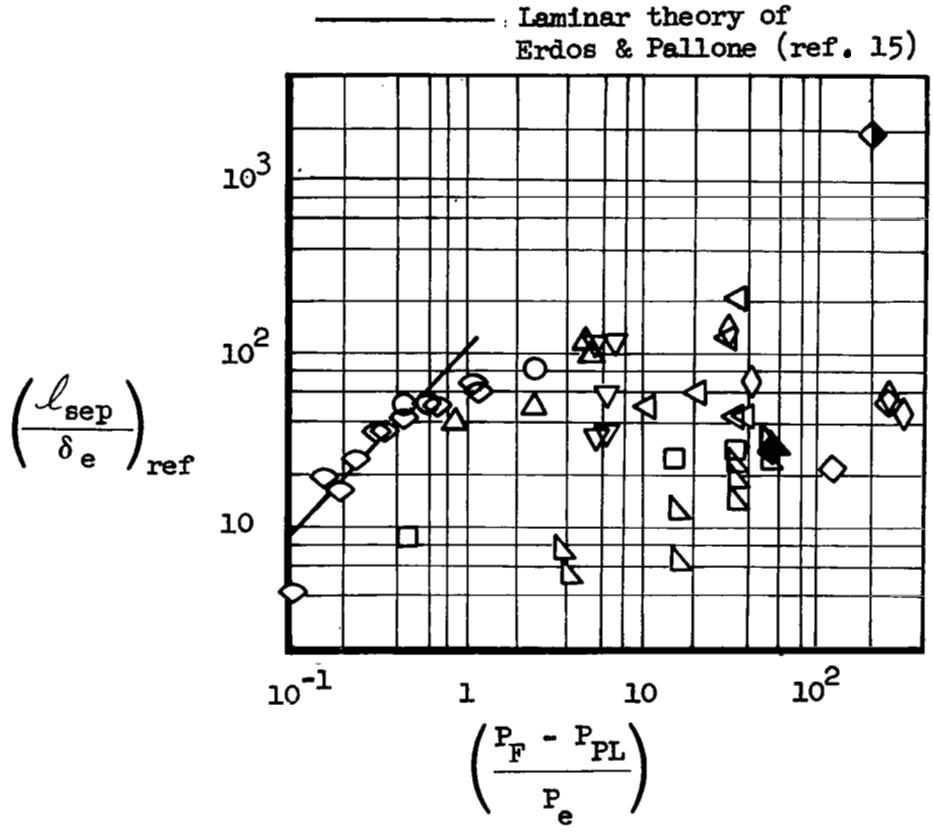

(a) Correlation with parameter of Erdos and Pallone

Figure 25.- Length of laminar and transitional separated region

	Model	Reference	M_e	ΔF, deg	N_{Re,L_r}	L_r, ft
◇	-	(24)Hakkinen	2	-	1.8×10^6	1
○	Plate	(26)Pate	3	var.	.375	.92
△	Plate	(26)Pate	3	var.	1.045	.92
▷	Plate	(25)Putnam	9.5-10	var.	1.26	.83
▽	Wing	X-20	5-7	20	1.202	1.22
◁	Wing	X-20	3.5-7	45	1.202	1.22
◇	Plate	X-20	5.5-12	45	.112	1
□	Plate	X-20	5.5-6	15-45	.112	1
◇	Plate	X-20	12-12.5	30-45	.112	1
◆	Plate	X-20	6-7	45	14.04	1
◆	Plate	X-20	4-5	45	14.04	1

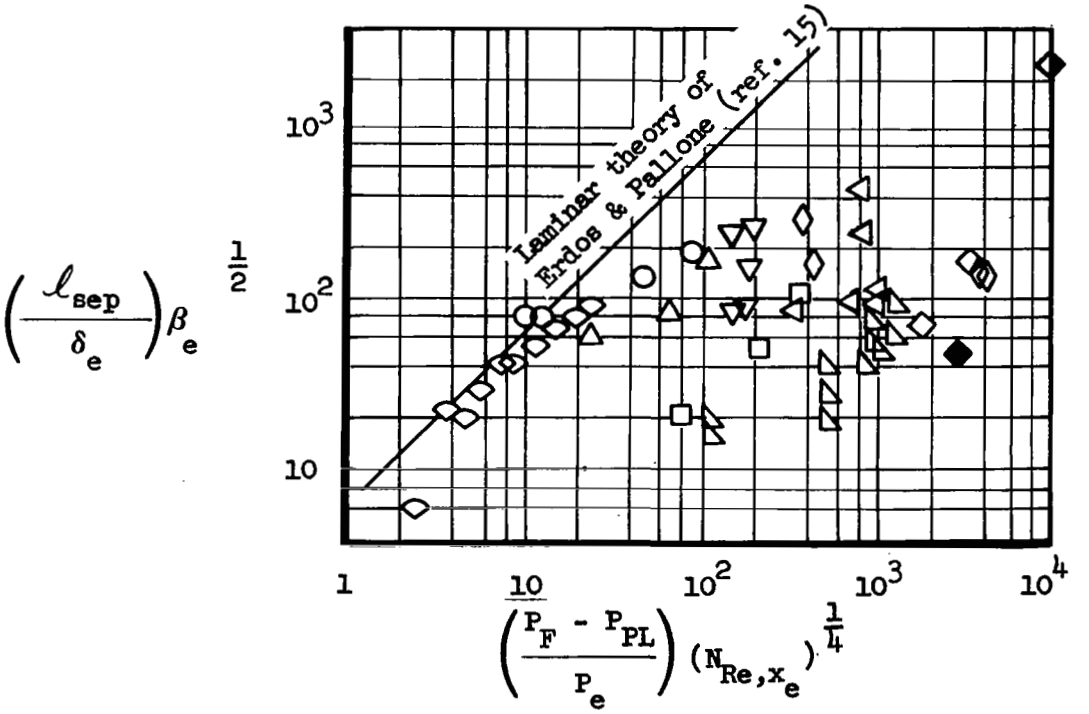

(b) Correlation with modified parameter of Erdos and Pallone

Figure 25.- Continued.

	Model	Reference	M_e	T_w / T_e	ΔF, deg	N_{Re,L_r}	L_r, ft
△	Plate	(25)Putnam	9.5-10	7.7	var.	1.26×10^6	.83
▽	Wing	X-20	5-7	2-5	20	1.202	1.22
◁	Wing	X-20	3.5-7	1.8-4.1	45	1.202	1.22
◇	Plate	X-20	5.5-12	1-3	45	.112	1
□	Plate	X-20	5.5-6	0.7-0.8	15-45	.112	1
◇	Plate	X-20	12-12.5	3-3.5	30-45	.112	1
◆	Plate	X-20	6-7	2.2	45	14.04	1

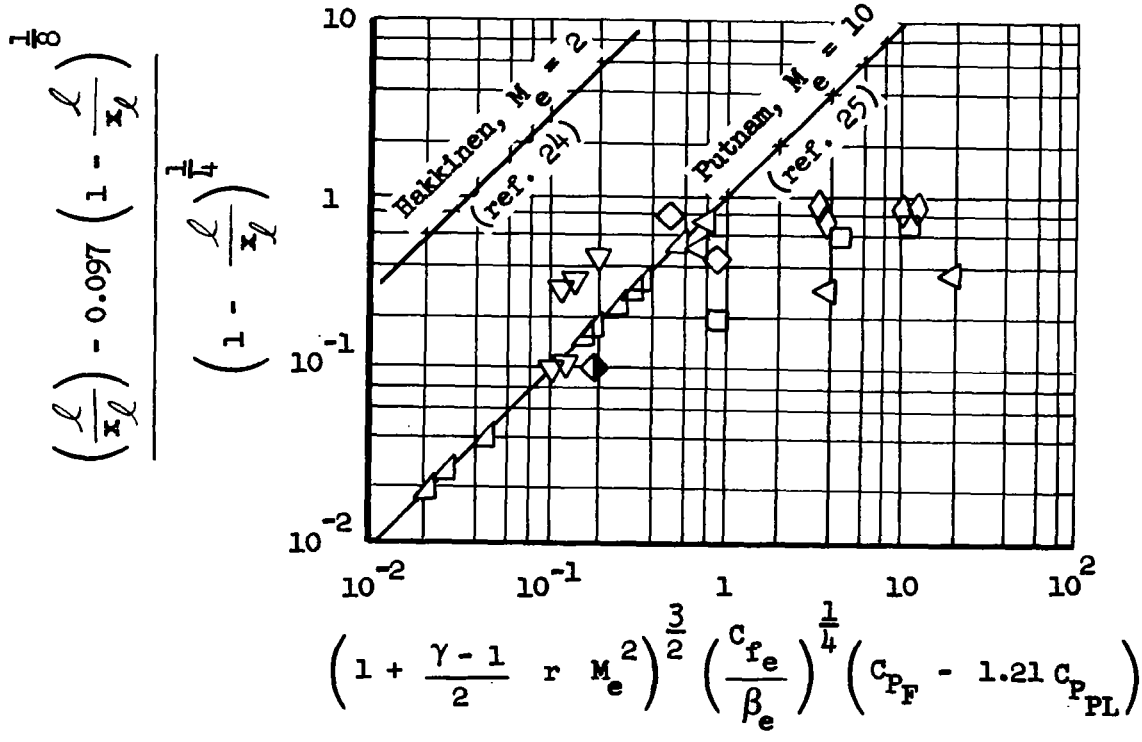

(c) Correlation with theory of Hakkinen, $T_w = T_{aw}$

Figure 25.- Continued.

	Model	Reference	M_e	ΔF, deg	N_{Re,L_r}	L_r, ft
◇	—	(24)Hakkinen	2	—	1.8×10^6	1
○	Plate	(26)Pate	3	var.	.375	.92
△	Plate	(26)Pate	3	var.	1.045	.92
▷	Plate	(25)Putnam	9.5-10	var.	1.26	.83
▽	Wing	X-20	5-7	20	1.202	1.22
◁	Wing	X-20	3.5-7	45	1.202	1.22
◇	Plate	X-20	5.5-12	45	.112	1
□	Plate	X-20	5.5-6	15-45	.112	1
◇	Plate	X-20	12-12.5	30-45	.112	1
◆	Plate	X-20	6-7	45	14.04	1
●	Plate	X-20	4-5	45	14.04	1

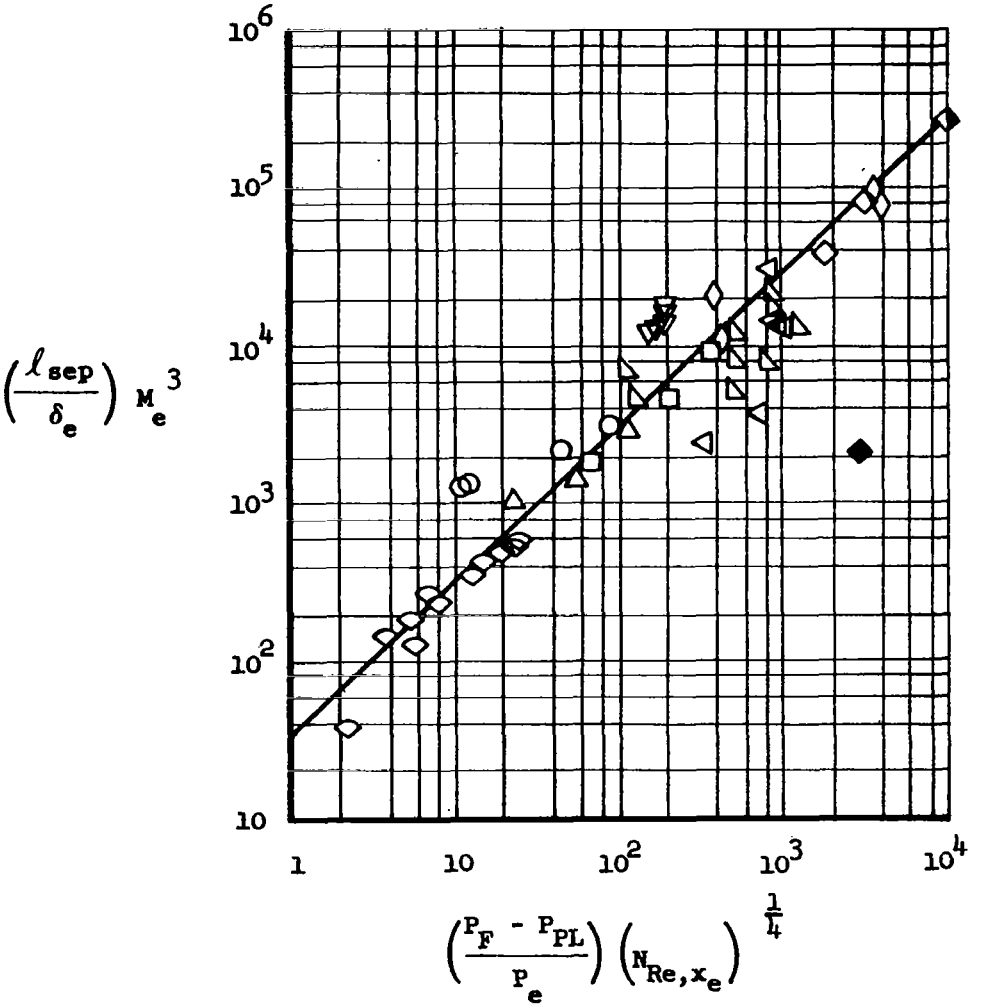

(d) Empirical correlation

Figure 25.- Concluded.

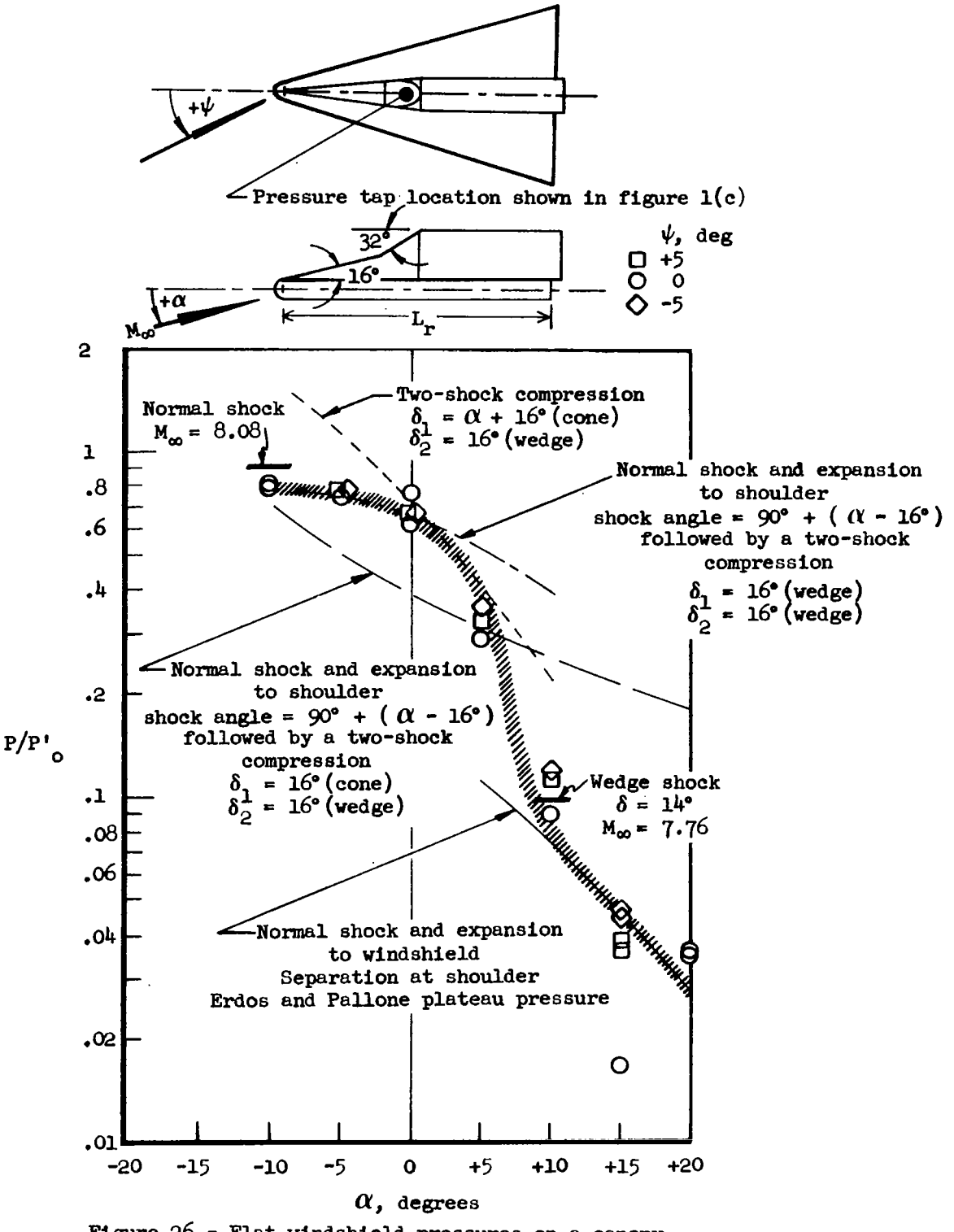

Figure 26.- Flat windshield pressures on a canopy.
$M_\infty = 8.08$; $N_{Re,L_r} = 1.202 \times 10^6$;
$P'_o = 1.63$ psia; $H_o = 7.5 \times 10^6$ ft-lb/slug.

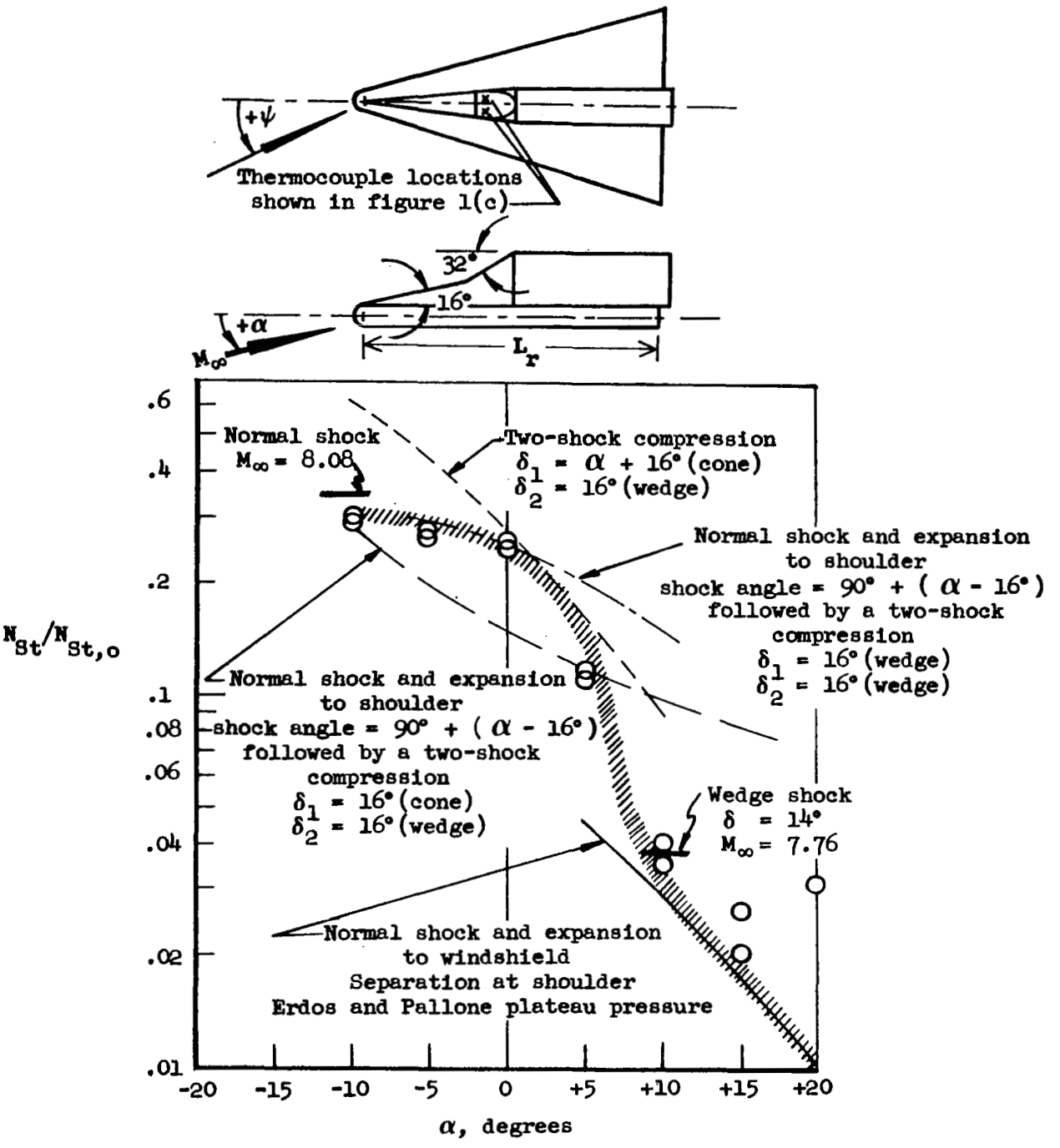

(a) $\psi = 0°$

Figure 27.- Flat windshield heating rates on a canopy.
$M_\infty = 8.08$; $N_{Re,L_r} = 1.202 \times 10^6$;
$P'_o = 1.63$ psia; $H_o = 7.5 \times 10^6$ ft-lb/slug.

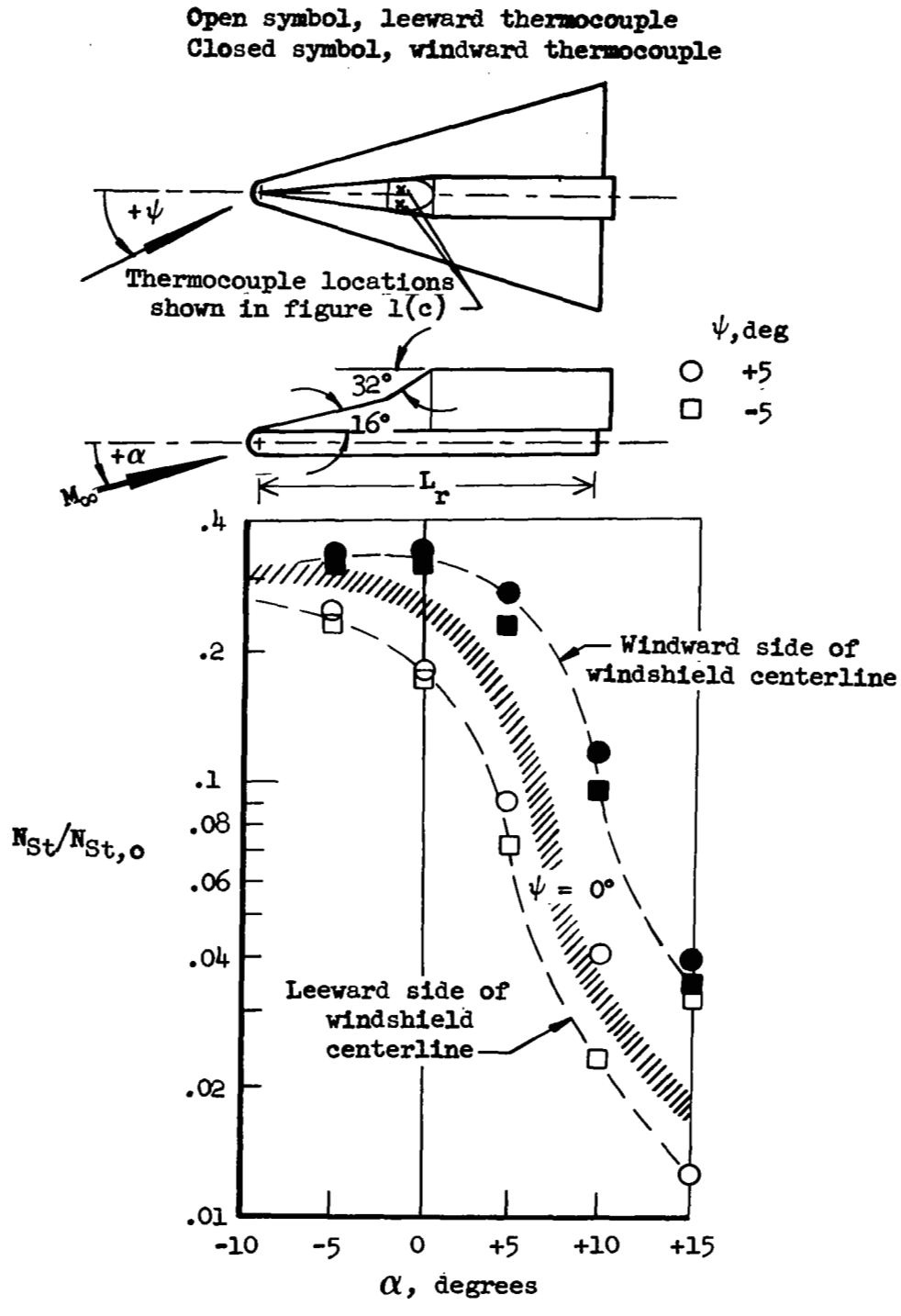

(b) ψ = +5° and -5°

Figure 27.- Concluded.

Thermocouple locations shown in figure 1(c).

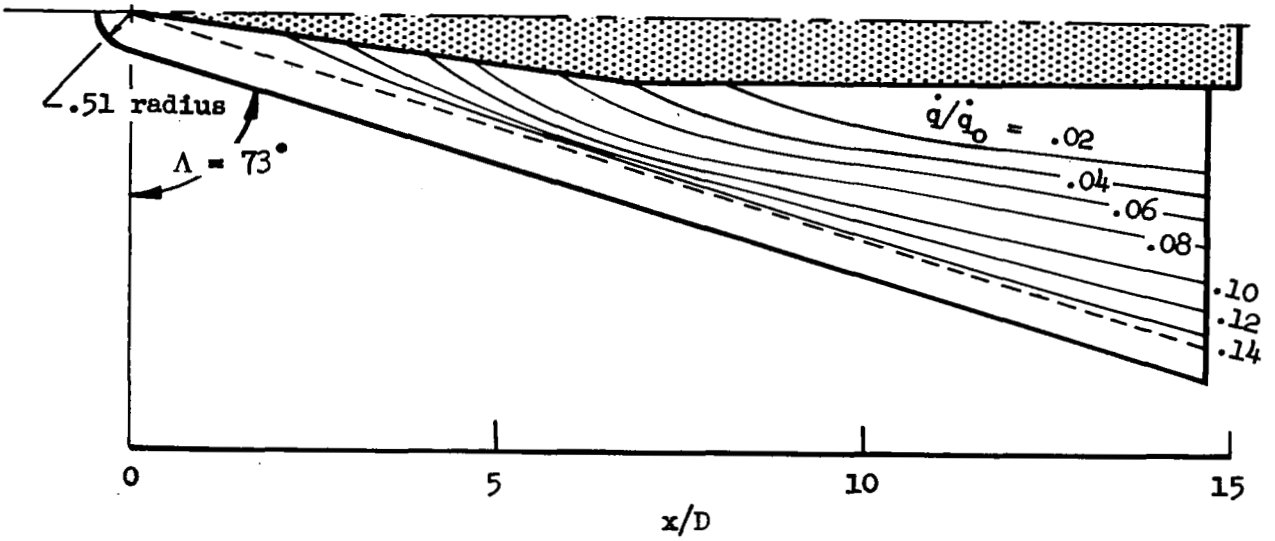

(a) $\alpha = 5°$

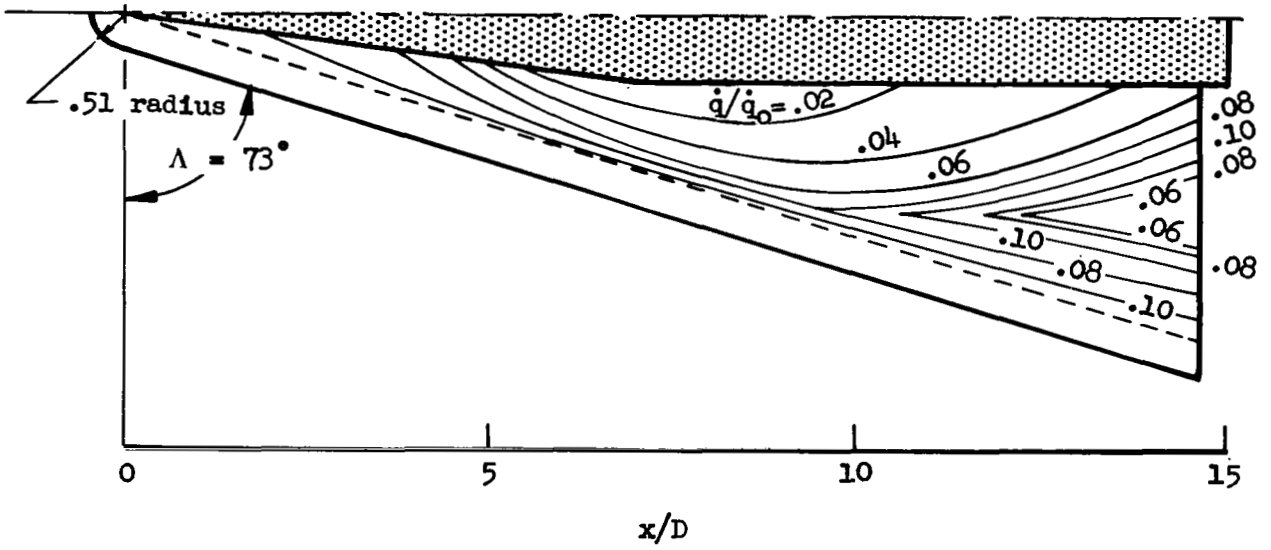

(b) $\alpha = 10°$

Figure 28.- Heating rate distributions on a blunt delta wing in proximity to a body. $M_\infty = 8.08$; $N_{Re,L_r} = 1.202 \times 10^6$; $P'_o = 1.63$ psia; $H_o = 7.5 \times 10^6$ ft-lb/slug; $\dot{q}_o = 11.56$ Btu/ft^2-sec

Thermocouple locations shown in figure 1(c).

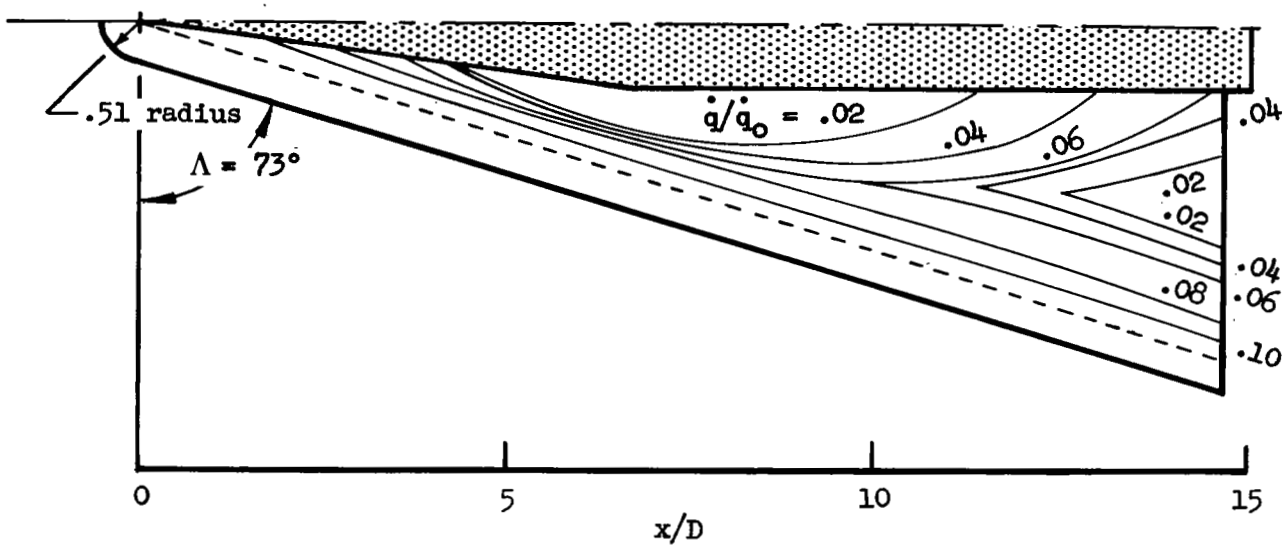

(c) α = 15°

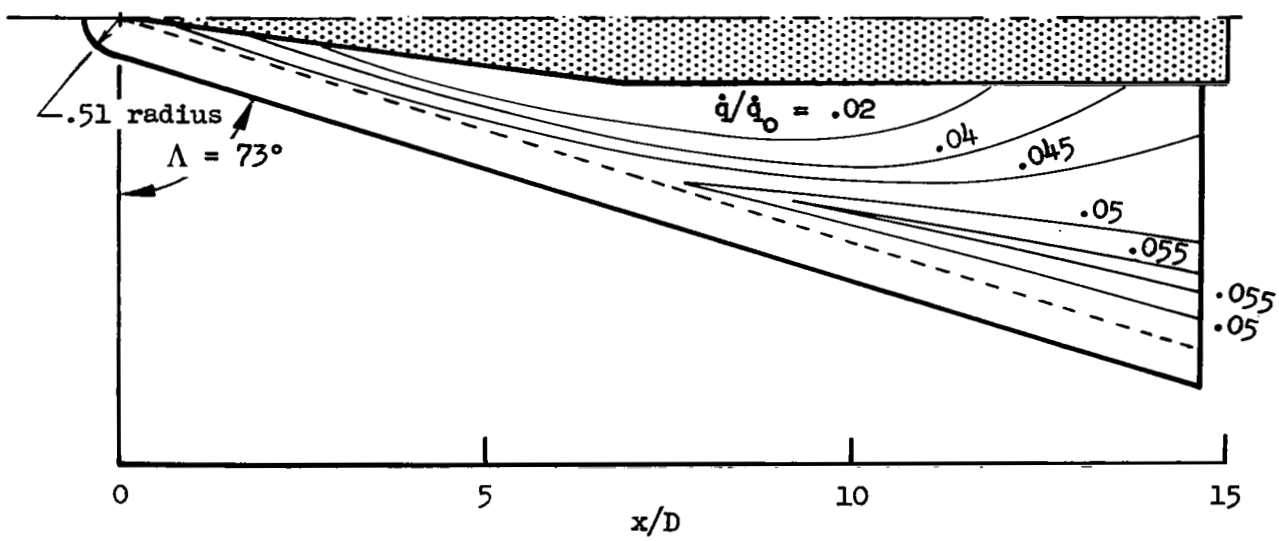

(d) α = 20°

Figure 28.- Concluded.

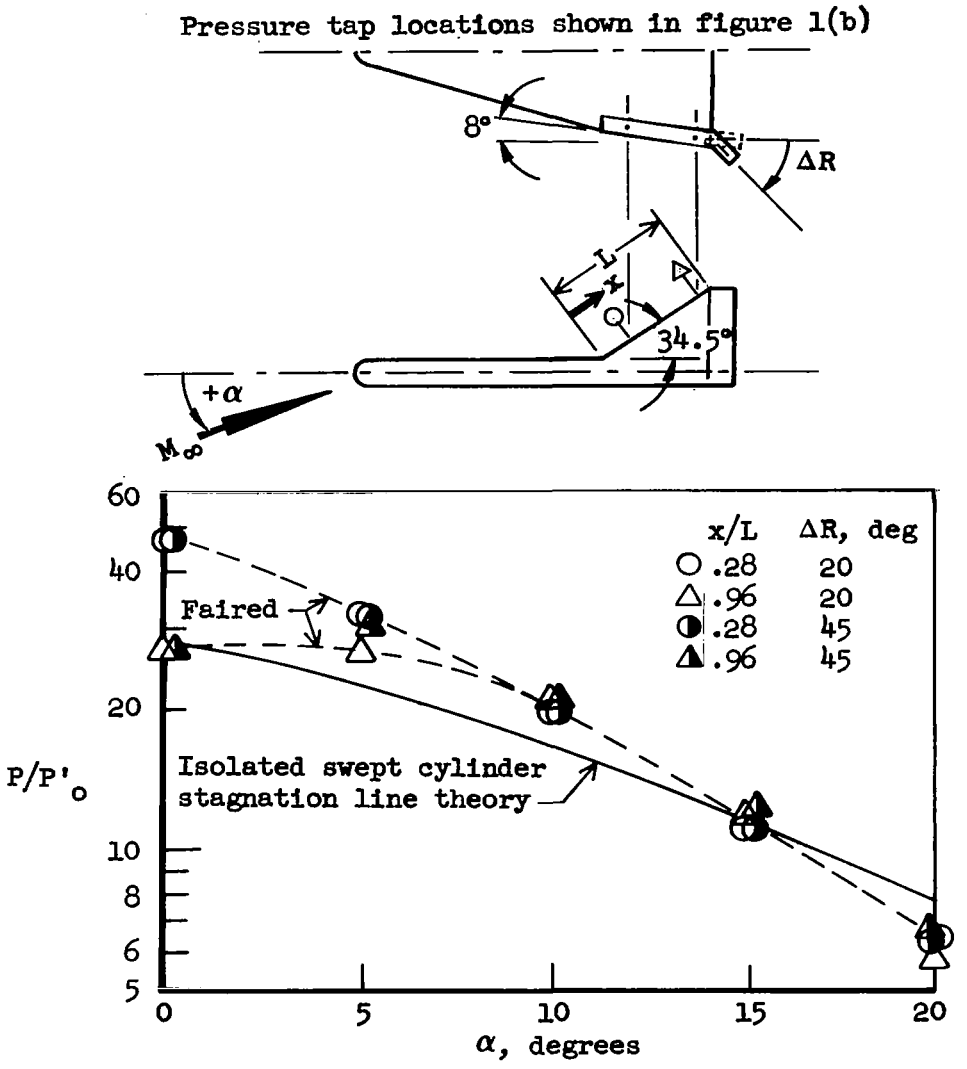

Figure 29.- Pressure on the leading edge of a swept fin mounted on the tip of a blunt delta wing.

$M_\infty = 8.08$; $N_{Re,L_r} = 1.202 \times 10^6$;

$P'_o = 1.63$ psia; $H_o = 7.5 \times 10^6$ ft-lb/slug.

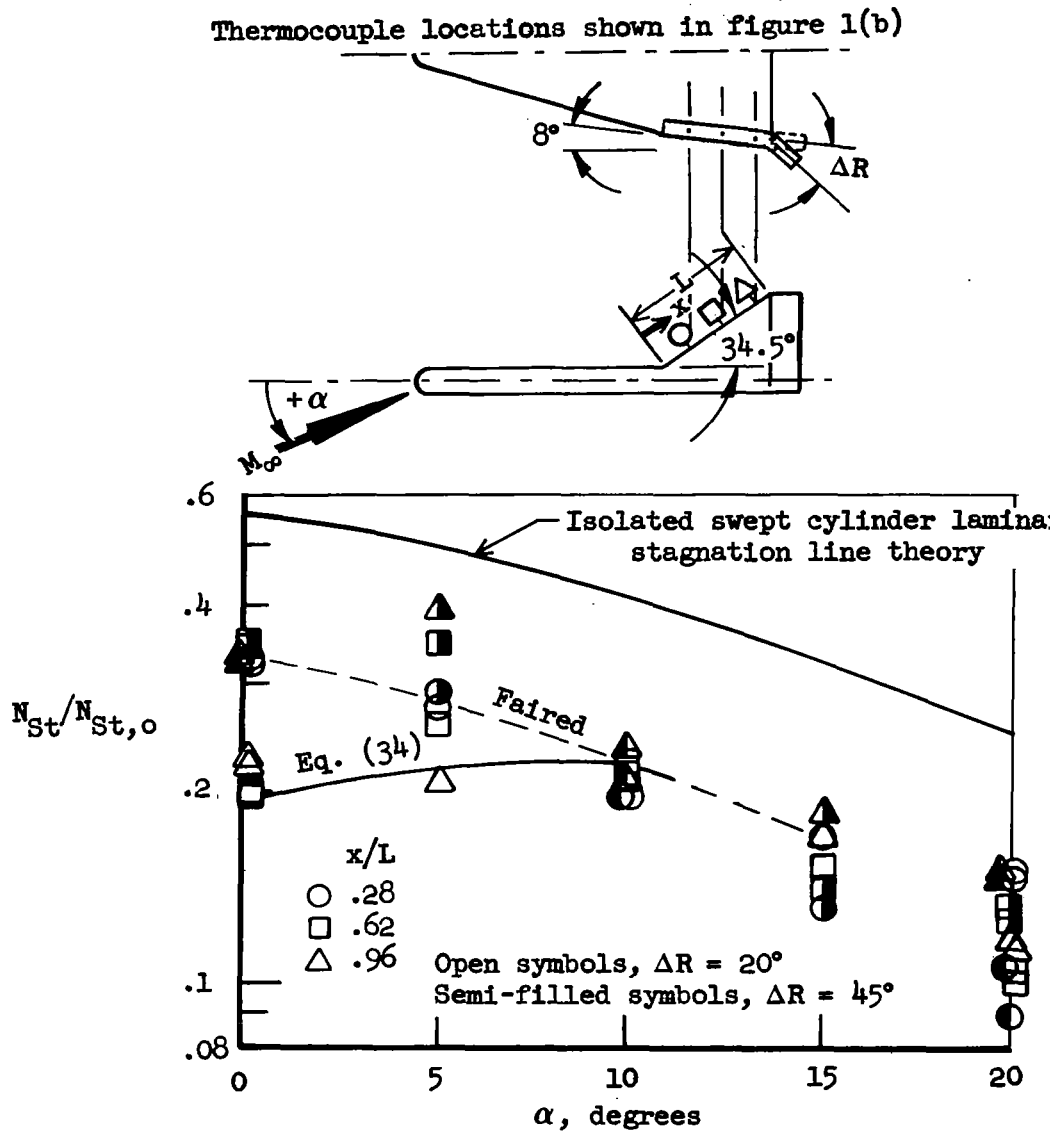

Figure 30.- Heating rates on the leading edge of a fin mounted on the tip of a blunt delta wing.

$M_\infty = 8.08$; $N_{Re,L_r} = 1.202 \times 10^6$;

$P'_o = 1.63$ psia; $H_o = 7.5 \times 10^6$ ft-lb/slug;

$N_{St,o} = .0277$.

REFERENCES

1. Nagel, A. L.; Fitzsimmons, D. H.; and Doyle, L. B.: Analysis of Hypersonic Pressure and Heat Transfer Tests on Delta Wings with Laminar and Turbulent Boundary Layers. NASA CR-535, 1966.
2. Jaeck, C. L.: Analysis of Pressure and Heat Transfer Tests on Surface Roughness Elements with Laminar and Turbulent Boundary Layers. NASA CR-537, 1966.
3. Ellison, R. K.: Turbulent Reference, Roughness, Leakage and Deflected Surface Heat Transfer and Pressure Tests for the Boeing Company Conducted in the CAL 48-inch Hypersonic Shock Tunnel. Cornell Aeronautical Laboratory Report No. AA-1161-Y-1, 1962.
4. Ames Research Staff: Equations, Tables, and Charts for Compressible Flow. NACA Report 1135, 1953.
5. Martin, J. F.; Duryea, G. R.; and Stevenson, L. M.: Instrumentation for Force and Pressure Measurements in a Hypersonic Shock Tunnel. Cornell Aeronautical Laboratory Report No. 133, January 1962.
6. Vidal, R. J.: Transient Surface Temperature Measurements. Cornell Aeronautical Laboratory Report No. 114, March 1962.
7. Staff of Cornell Aeronautical Laboratory: CAL 48-inch Hypersonic Shock Tunnel - Description and Capabilities. Cornell Aeronautical Laboratory, Inc., May 1962.
8. Reece, J. W.: Shock Tube Theory for Real Air with Application to Wind Tunnel Testing and to Flight Simulation. Cornell Aeronautical Laboratory Report No. WTH-003, October 1958.
9. Staff of Arnold Engineering Development Center: Test Facilities Handbook, Volume 4. Arnold Engineering Development Center, Arnold Air Force Station, Tennessee, July 1963.
10. Chapman, Dean R.; Kuehn, Donald M.; and Larson, Howard K.: Investigation of Separated Flows in Supersonic and Subsonic Streams with Emphasis on the Effects of Transition. NASA Report 1356, March 1957.
11. Curle, N.: The Effects of Heat Transfer on Laminar-Boundary-Layer Separation in Supersonic Flow. The Aeronautical Quarterly, November 1961.
12. Gadd, G. E.: Interactions Between Wholly Laminar or Wholly Turbulent Boundary Layers and Shock Waves Strong Enough to Cause Separation. Journal of the Aeronautical Sciences, vol. 20, 1953.
13. Gadd, G. E.: A Theoretical Investigation of Laminar Separation in Supersonic Flow. Journal of Aeronautical Sciences, vol. 24, 1957.
14. Gadd, G. E.: An Experimental Investigation of Heat Transfer Effects on Boundary-Layer Separation in Supersonic Flow. Journal of Fluid Mechanics, vol. 2, 1957.
15. Erdos, John; and Pallone, Adrian: Shock Boundary Layer Interaction and Flow Separation. Proceedings of the 1962 Heat Transfer and Fluid Mechanics Institute held at the University of Washington, June 13, 14, and 15, 1962.
16. Chapman, D. L.: A Theoretical Analysis of Heat Transfer in Regions of Separated Flow. NACA TN 3792, October 1956.
17. Larson, H. K.: Heat Transfer in Separated Flows. IAS Report No. 59-37, January 1959.

18. Holloway, P. F.; Sterrett, J. R.; and Creekmore, H. S.: An Investigation of Heat Transfer within Regions of Separated Flow at a Mach Number of 6.0 NASA TN D-3074, November 1965.
19. Chung, P. M.; and Viegas, J. R.: Heat Transfer at the Reattachment Zone of a Laminar Boundary Layer. NASA TN D-1072, September 1961.
20. Lees, L: Laminar Heat Transfer Over Blunt Nosed Bodies at Hypersonic Speeds. Jet Propulsion, Vol. 26, 1956, pp. 259-269 and 274.
21. Dewey, C. Forbes, Jr.: Use of Local Similarity Concepts in Hypersonic Viscous Interaction Problems. AIAA Journal, January 1963.
22. Graham, W. J.; and Vas, I. E.: An Experimental Investigation of the Separation of a Hypersonic Boundary Layer of a Flat Plate, Part I: Pressure Distribution and Optical Studies at M = 11.7. Aeronautical Research Laboratory Report ARL 63-74, May 1963.
23. Sterrett, J. R.; and Holloway, P. F.: On the Effect of Transition on Parameters within a Separation Region at Hypersonic Speeds - with Emphasis on Heat Transfer. Symposium on Fully Separated Flows, American Society of Mechanical Engineers, Fluid Engineering Division Conference, Philadelphia, Pennsylvania, May 18-20, 1964.
24. Hakkinen, R. J.; Greber, I.; Trilling, L.; and Abarbanel, S. S.: The Interaction of an Oblique Shock Wave with a Laminar Boundary Layer. NASA Memo 2-18-59W, 1959.
25. Putnam, L. E.: Investigation of Effects on Ramp Span and Deflection Angle on Laminar Boundary Layer Separation at Mach 10.03. NASA TN D-2883, May 1965.
26. Pate, S. R.: Investigation of Flow Separation on a Two-Dimensional Flat Plate Having a Variable-Span Trailing-Edge-Flap at M_∞ = 3 and 5. Technical Documentary Report No. AEDC-TDR-64, ARO, Inc., March 1964.
27. Gulbran, C. E.; Redeker, E.; Miller, D. S.; and Strack, S. L.: Heating in Regions of Interfering Flow Fields. Part I. Two and Three-Dimensional Laminar Interactions at Mach 8. AFFDL-TR-65-49, July 1965.
28. Eckert, Ernst R. G.: Survey on Heat Transfer at High Speeds. WADC Tech. Rep. No. 54-70, Wright Air Development Center, Wright Patterson Air Force Base, Ohio, 1954.